

**REMOVING LOVE WAVES
FROM
SHALLOW SEISMIC SH-WAVE DATA**

PROEFSCHRIFT

ter verkrijging van de graad van doctor
aan de Technische Universiteit Delft,
op gezag van de Rector Magnificus Prof. dr. ir. J.T. Fokkema,
in het openbaar te verdedigen ten overstaan van een commissie,
door het College voor Promoties aangewezen,
op maandag 19 januari 2004 te 15:30 uur

door

Lourens Frank VAN ZANEN

doctorandus in de natuurkunde
geboren te Wormerveer

Dit proefschrift is goedgekeurd door de promotoren:

Prof. dr. ir. J.T. Fokkema

Prof. dr. ir. C.P.A. Wapenaar

Toegevoegd promotor: Dr. ir. G.G. Drijkoningen

Samenstelling promotiecommissie:

Rector Magnificus,	voorzitter
Prof. dr. ir. J.T. Fokkema,	Technische Universiteit Delft, promotor
Prof. dr. ir. C.P.A. Wapenaar,	Technische Universiteit Delft, promotor
Dr. ir. G.G. Drijkoningen,	Technische Universiteit Delft, toegevoegd promotor
Prof. dr. S.A.P.L. Cloetingh,	Vrije Universiteit Amsterdam
Prof. dr. ir. P.M. van den Berg,	Technische Universiteit Delft
Dr. ir. G.C. Herman,	Technische Universiteit Delft, Shell
Dr. J. Brouwer,	TNO-NITG Utrecht
Prof. dr. ir. A. Gisolf,	Technische Universiteit Delft, reservelid

ISBN 90-9017719-1

Copyright © 2004 by L.F. van Zanen, Section of Applied Geophysics, Department of Applied Earth Sciences, Faculty of Civil Engineering and Geosciences, Delft University of Technology.

All rights reserved, No parts of this publication may be reproduced, stored in a retrieval system or transmitted, in any form or by any means, electronic, mechanical, photocopying, recording, or otherwise, without the prior written permission of the author.

To my wife, Carola

Contents

1	Introduction	1
1.1	General description of seismic exploration	2
1.2	Problem statement	3
1.2.1	Defining the problem	3
1.2.2	Existing methods for removing surface effects	4
1.2.3	Our approach	5
1.3	Outline of this thesis	6
2	Basic elastodynamic theory	9
2.1	Mathematical considerations	10
2.2	Elastodynamic equations	10
2.2.1	Equation of motion	10
2.2.2	Equation of deformation rate	11
2.2.3	Boundary conditions	13
2.3	Equations in the Laplace domain	14
2.4	Elastic waves in an unbounded homogeneous medium	15
2.5	The Betti-Rayleigh reciprocity theorem	17
2.6	Application of reciprocity: physical reciprocity	19
3	Removal of Love waves from land seismic SH-wave reflection data	21
3.1	Reciprocity theorem for SH-waves	22
3.2	Description of the reciprocity states	22

3.2.1	The actual state - with a stress free surface	22
3.2.2	The desired state - without a surface	23
3.2.3	The domain of integration	24
3.3	Application of the reciprocity theorem	25
3.3.1	The stress in terms of velocity	27
3.3.2	Integral equation of the second kind for the no-surface wavefield	29
3.4	Horizontally layered media	31
3.5	Numerical implementation for laterally varying media	33
3.6	Numerical tests and results	35
3.6.1	A horizontally layered medium	36
3.6.2	A medium with an interface with a jump	38
3.6.3	A medium with a complex interface	40
3.6.4	A medium with scatterers	42
4	Sensitivity of the Love-wave removal method	45
4.1	Effect of an erroneous estimation of input parameters	46
4.1.1	Effect of an erroneous estimation of the velocity . . .	46
4.1.2	Effect of an erroneous estimation of the mass density .	47
4.2	Effect of distorted input data	48
4.2.1	Effect of random noise	48
4.2.2	Effect of anelastic attenuation	50
4.3	Effect of an erroneous estimation of the source wavelet	50
5	Towards removal of surface effects from coupled P- and SV- wave systems	55
5.1	Reciprocity for coupled P- and SV-wave systems	56
5.2	Description of the reciprocity states	56
5.2.1	The actual state - with a stress-free surface	56
5.2.2	The desired state - without a surface	57
5.3	Application of the reciprocity theorem	58
5.4	Removing Rayleigh waves from a homogeneous halfspace . . .	62
5.5	Numerical test and results	64
5.6	Removing surface effects from horizontally layered media . .	66
6	Conclusions	71
A	Integral transforms and their properties	77
A.1	The Laplace transform	77

A.1.1	Continuous Laplace transform	77
A.1.2	Numerical implementation	79
A.1.3	Discretization in the time domain	79
A.2	The spatial Fourier transform	80
A.2.1	Fourier transform with respect to the receiver coordinate	81
A.2.2	Fourier transform with respect to the source coordinate	82
A.2.3	Discretization in the space domain	82
B	Elastodynamic radiation from line sources	85
B.1	The incident SH-wave field	85
B.2	The incident P- and SV-wave field	87
B.2.1	The x_1 component of the particle velocity, due to a source in the x_1 direction	89
B.2.2	The x_3 -component of the particle velocity, due to a source in the x_3 direction	90
B.2.3	The x_1 -component of the particle velocity, due to a source in the x_3 direction, and vice versa	91
C	Application on field data	93
C.1	Geometry of the dataset	95
C.2	Source and receiver considerations	96
C.3	Preprocessing steps	98
C.4	Results of the removal procedure on the Sofia data	100
C.4.1	Deviations in the source wavelets	103
C.4.2	Deviations in shot-sensitivity	103
C.4.3	Use of 1-D scheme to 1-D shot	105
C.5	Conclusions and recommendations	112
C.5.1	Concerning near-field and 3-D effects	112
C.5.2	Concerning heterogeneities and anisotropy	113
D	An attempt at wavelet estimation based on energy minimiza- tion	115
D.1	Basis definitions	116
D.2	Problem statement	116
D.3	Iterative solution	117
D.3.1	Minimizing the energy	118
D.3.2	The (conjugate) gradient direction	120
D.3.3	Initial Guess	120
D.4	Results and discussion	121

Bibliography	124
Abstract	129
Samenvatting	133
Curriculum Vitae	137
Acknowledgments	139

Introduction

This thesis presents a new method that can be used in seismic data processing. The method aims to eliminate surface effects from seismic land data, without disturbing the desired reflection information. Elastic reciprocity is used for this purpose. This thesis discusses the implementation and practical aspects of the method.

This introductory chapter serves three purposes. First, it gives a short description of some of the basic terms used in seismic exploration. Second, it discusses the problems we address in this thesis, and gives a summary of the currently available techniques used to address these problems. Third, and final, it gives an outline of this thesis.

1.1 General description of seismic exploration

The main goal of seismic exploration is to make an image of the subsurface, and to find its medium parameters. Preferably, this information is obtained without making disruptions in the subsurface. The use of seismic (or sound) waves is one example of such a non-destructive method. Traditional seismic exploration aims at finding hydro-carbons such as oil and gas. Often, these resources are located in reservoirs several kilometers deep in the earth. In recent years, however, there were developments where the focus of seismic exploration became the shallow subsurface, typically no more than 100 meters deep. The main applications for this target area lie in subsurface engineering (Steeple and Miller [1990]; Swinnen et al. [1998]), environmental issues and archaeological investigations.

But how do we make an image of the subsurface by using seismic waves? The following description is meant for those who are not familiar with seismology, and will describe the basic terms.

We focus our attention on land seismic experiments only (as opposed to marine seismics). In these experiments, the seismic waves we mentioned are generated by a source at or just below the surface. This source can be dynamite or, when we want the source to be more controlled, a vibrator source. A special type of vibrator source, when we want to generate shear waves (see Chapter 2), is the horizontal vibrator (Ghose et al. [1996]). The generated wave propagates into the subsurface. When it comes at a place where the material properties of the subsurface change (i.e. when the wave encounters a layer interface or an object), part of the wave will be reflected, and part of the wave will travel deeper into the subsurface, where it will (probably) encounter other changes. When the reflected part of the wave reaches the surface, the resulting vibrations are detected by receivers, which we call *geophones*. Figure 1.1 shows a graphical representation of the description above. Such a configuration is also called a *shot* (i.e. one source, and several recording receivers), and the resulting recorded data is subsequently called a *shot record*, or equivalently, a *common source gather*. Generally, many shot records are needed to obtain an adequate image of the subsurface.

The arrival time of a reflected wave tells us something about the velocity with which it traveled through the subsurface, and therefore also about the depth of the reflecting layer. Its amplitude is related to the spatial changes of the medium properties. Therefore, the seismic data can be used to make an image of the Earth's subsurface. More information about processing seismic data is found in for example Yilmaz [1987].

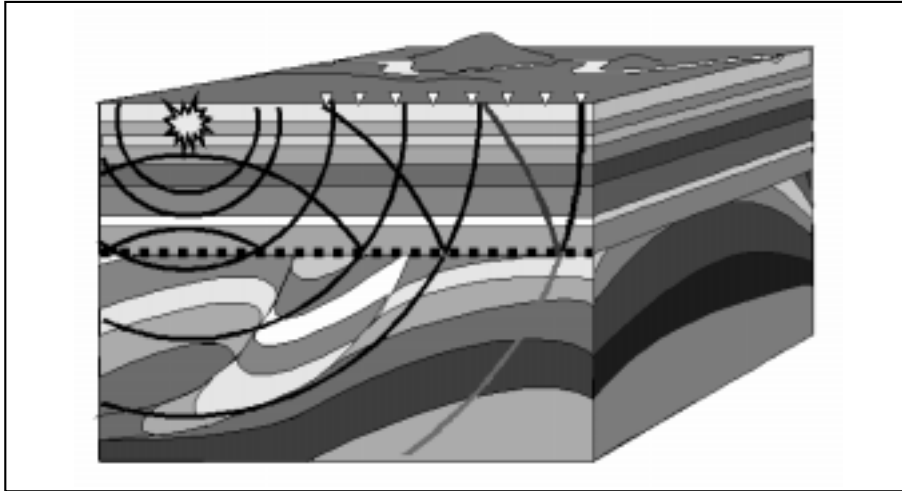


Figure 1.1: Geometry for one shot record of a land seismic experiment. The arcs indicate possible wave fronts of the generated waves, the triangles represent the geophones.

1.2 Problem statement

■ 1.2.1 Defining the problem

The difference between seismic experiments on land and marine seismic experiments lies in the physical characteristics of the top layer. On land, the top layer consists of an elastic medium, whereas in the marine case, it consists of water, which is an acoustic medium. This difference results in different types of surface related wave phenomena.

There are two types of waves that can propagate through an elastic medium: compressional waves (P-waves) and shear waves (S-waves)¹. The velocity of shear waves is always lower than that of P-waves (we review the proof for this in Chapter 2).

Shear waves are also divided into two types: waves polarized in a vertical plane (SV-waves) and horizontally polarized waves (SH-waves). In many cases, SH-waves are decoupled from the other two wave types, or, in other words, they propagate independently. Since they have a lower velocity than

¹In an acoustic medium, there is only one wave type, which is equivalent to a P-wave.

P-waves, it is possible to have a higher resolution and more detail in the data with the same frequency content. Also, in air- or gas-filled media, P-waves are often severely scattered, while S-waves are hardly affected. These are the reasons why a seismic SH-wave reflection experiment is an adequate and cost effective method to image the shallow subsurface (Deidda and Balia [2001]).

Unfortunately, reflected waves are not the only type of waves that are recorded. Seismic data are almost always polluted with surface related wave phenomena. Surface waves are considered unwanted noise, because they carry little or no subsurface information data. In the case of SH-waves, these surface waves are called *Love waves* (so called because they were first described by Love [1926]), and they often pose a large problem in the data processing (Miller et al. [2001]). For an extended discussion on Love waves, see for example Aki and Richards [1980].

Due to several reasons, it is difficult to remove surface waves, like Love waves, from seismic data. One problem is that, since they propagate solely along the surface, they attenuate slowly, and therefore they make up most of the energy in a shot record, obscuring the reflection data from shallow layers. Another problem, is that surface waves like Love waves and Rayleigh waves have a group velocity that is almost equal to the shear wave velocity. This is especially true for soft soils. This makes it hard to remove surface waves from seismic data with conventional methods based on velocity discrimination, such as (f, k) -domain filtering. A third problem is that many surface waves are dispersive. This means that their phase velocity is frequency dependent. It is yet another difficulty when we try to apply velocity based filtering.

■ 1.2.2 Existing methods for removing surface effects

One of the earliest methods to suppress surface waves from seismic data is the application of *geophone arrays* (Holtzman [1963]; Morse and Hildebrandt [1989]). In this method, groups of geophones are placed in such a way that, after summing their responses, they attenuate certain wavenumbers, hence this resembles a moving-average filter. However, as this method is applied in the field, before processing, it requires some a priori information of the subsurface. We have to know which wavenumbers will contain the surface waves (which generally have shorter apparent wavelengths), and which wavenumbers will contain the desired reflection data (which generally have longer apparent wavelengths), and design the geophone array with this information.

A processing method for removing dispersive events was developed for example by Ernst and Herman [1998] or Blonk [1995]. They developed methods

in which they estimate a model of the near subsurface, calculate the response, and subtract that response from the data, thus leaving the deeper reflections intact. However, these methods, as stated, require that a great amount of time is spent in developing a model for the immediate subsurface, whereas generally, the main focus of a seismic experiment is the structure of the deeper layers.

Nguyen et al. [1999] propose a method where they use a combination of filter techniques to remove dispersive surface waves. But a part of their method uses the polarization characteristics of Rayleigh waves, and therefore needs multi-component seismic data, whereas the main focus of this thesis lies with single-component SH-wave data. Their method can therefore not be used for removing Love waves from SH-wave data.

Saatçılar and Canitez [1994] developed a technique with the help of a lattice filter. In addition to removing the surface waves, it also works as a spiking/predictive deconvolution. But since this is a trace-by-trace filter technique, it could damage the relative amplitudes of events in a record. This is something we would like to avoid, in case the data is used in further amplitude versus offset (AVO) studies.

■ 1.2.3 Our approach

The ideal filter should be able to completely remove all effects caused by the presence of the surface, but should simultaneously not disturb the effects caused by the actual subsurface structure. Furthermore, it should not be dependent on a priori information of the subsurface structure, since this subsurface structure is the goal of the seismic experiment.

Our approach is similar to that of van Borselen et al. [1996]. They used Rayleigh's acoustic field reciprocity to remove surface related water layer multiples from marine seismic data. The relevant difference between Love waves and water layer multiples is that multiples are propagating waves, whereas Love waves occur primarily in the evanescent regime. Van Borselen et al. arrive at an iterative procedure, a so-called Neumann series expansion, where the n^{th} iteration removes the n^{th} order multiple. A similar iterative procedure was developed by Verschuur et al. [1992]. The difference is that they first made a forward modeling scheme based on physical arguments, and then inverted this scheme to arrive at an expression for the multiple-free wavefield in terms of the wavefield containing surface multiples.

We use the Betti-Rayleigh elastic field reciprocity theorem and elastodynamic wave theory. Reciprocity is a mathematical concept by which two

different states are related to each other. In our case, the two states are wavefields in an elastic medium. One state is defined as the actual state, where a (stress-free) surface is present, the other state is the desired state, that differs only from the actual state (i.e. the physical reality) by the absence of this surface. The result is an integral equation of the second kind, from which we can find the wavefield without surface effects (especially the Love waves) from the wavefield which includes those effects.

1.3 Outline of this thesis

Chapter 2 starts with the derivation of the elastodynamic equations. It introduces the basic quantities that are used throughout this thesis. With these elastodynamic equations, we show that the wavefield decouples into three different wave types (P-waves, SV-waves and SH-waves) in a homogeneous and unbounded elastic medium. Also, this chapter derives the Betti-Rayleigh reciprocity theorem, a mathematical tool to relate two states in an elastic medium to each other. This is the starting point for the derivation of the Love-wave suppression method.

Chapter 3 applies the Betti-Rayleigh reciprocity theorem on the decoupled case of SH-waves to arrive at an expression which relates the wavefields of an actual state and a desired state to each other. The actual state has a stress-free surface, as is the case in the field, while the desired state differs only in the sense that it lacks a surface. The resulting expression is an integral equation of the second kind, which, after discretization, can be written as a matrix equation. This matrix equation is solved with for example a direct matrix inversion. Instead of just in the space domain, the matrix equation can also be solved in the horizontal slowness domain. If we then assume a horizontally layered medium, the kernel of the matrix equation becomes diagonal, and an efficient algebraic expression is obtained. The chapter is concluded with some examples of the method working on synthetic data.

In Chapter 4, a sensitivity study is performed on the method. We test the method for deviations in the input parameters and for distorted input data. A third test will be the sensitivity to the source wavelet, which is an input vector of the method.

Chapter 5 follows the same strategy as Chapter 3, but applies the reciprocity theorem on coupled P- and SV-wave systems. With this approach, the aim is to remove Rayleigh waves from seismic data. Since P- and SV-wave systems are coupled, the resulting removal equations are coupled too.

For reasons of simplicity, we limit our analysis to horizontally layered configurations only, and we give one example where we remove the Rayleigh wave from a homogeneous halfspace.

Finally, Chapter 6 concludes this thesis with a summary of the most important conclusions and observations.

Basic elastodynamic theory

In this chapter, we derive the linearized elastodynamic equations that describe the elastic wavefield in term of its relevant quantities: the stress and the particle velocity, due to volume source densities of force, and volume source densities of deformation rate. It is shown that three different wave types exist in an elastic medium: compressional waves (P-waves), shear waves polarized in a vertical plane (SV-waves) and horizontally polarized shear waves (SH-waves). Furthermore, it is shown that in a homogeneous and isotropic medium, the SH-waves are decoupled from the other wave types.

Using the elastodynamic equations, we derive the Betti-Rayleigh reciprocity theorem. This theorem provides a means to relate the elastodynamic wavefields of two states in an elastic medium to each other. This reciprocity theorem is the starting point of our analysis in Chapter 3.

2.1 Mathematical considerations

A location in the 3-dimensional Euclidian space is denoted by a vector $\mathbf{x} = \{x_1, x_2, x_3\}$, where a right-handed Cartesian coordinate system is used, set up by three orthonormal base vectors $\{\mathbf{i}_1, \mathbf{i}_2, \mathbf{i}_3\}$, such that $\mathbf{x} = x_1\mathbf{i}_1 + x_2\mathbf{i}_2 + x_3\mathbf{i}_3$. The \mathbf{i}_3 vector points vertically downward.

Where applicable, the Einstein summation convention for repeated indices is employed, i.e. $a_i b_i$ stands for $\sum_{i=1}^3 a_i b_i = a_1 b_1 + a_2 b_2 + a_3 b_3$.

The symbol ∂_i will be used as a short-hand notation for the partial derivative with respect to the x_i coordinate, and a differentiation with respect to time is denoted as ∂_t , where t is the time coordinate.

The Kronecker delta tensor is defined as: $\delta_{i,j} = 1$ when $i = j$ and 0 otherwise. The anti-symmetrical tensor of Levi-Civita is defined as: $\varepsilon_{i,j,k} = 1$ on an even permutation of 1, 2 and 3, $\varepsilon_{i,j,k} = -1$ on an odd permutation, and $\varepsilon_{i,j,k} = 0$ otherwise.

2.2 Elastodynamic equations

For the course of this thesis, it is assumed that the changes in an elastic medium due to wave propagation are small enough for the medium to behave linearly. Here, we derive the basic equations that describe linearized elastic wave propagation. Only a simple derivation is given, to introduce the basic terms. For a more extensive discussion, we refer to de Hoop [1995] or Aki and Richards [1980].

■ 2.2.1 Equation of motion

Suppose we have an arbitrary elastic element, with volume V , bounded by a closed surface S . External forces can be applied to it. They can cause the element to move or to be deformed. The traction t_i at a point on the surface is defined as:

$$t_i = \frac{dF_{i,S}}{dA}, \quad (dA) \rightarrow 0, \quad (2.1)$$

where $dF_{i,S}$ is the force in the x_i direction on the surface, and dA is an (infinitesimal small) piece of the surface. From there, we introduce the *stress tensor* $\tau_{i,j}$ as:

$$t_i = \tau_{i,j} n_j. \quad (2.2)$$

Here, n_j is the component in the x_j direction of the unit normal vector on the surface. So $\tau_{i,j}$ is the traction in the x_i direction across a surface whose

plane is perpendicular to the x_j axis. From the linearized law of conservation of angular momentum follows that the rate of change of angular momentum is equal to the resultant moment of forces. De Hoop and Aki and Richards show that this means that the stress tensor is symmetric: $\tau_{i,j} = \tau_{j,i}$.

From here, we go to Newtons *equation of motion*. This equation states that the total of forces on the body (the surface forces t_i and the volume source density of body forces f_i) causes a change in impulse:

$$\oint_S t_i d^2\mathbf{x} + \int_V f_i d^3\mathbf{x} = \partial_t \int_V \rho v_i d^3\mathbf{x}. \quad (2.3)$$

In this equation, ρ is the volume density of mass of the material, and v_i is the velocity of a particle within the material. The leftmost term of the left side of this equation can, with the help of eq. (2.2) and Gauss' divergence theorem, be written as:

$$\oint_S t_i d^2\mathbf{x} = \oint_S \tau_{i,j} n_j d^2\mathbf{x} = \int_V \partial_j \tau_{i,j} d^3\mathbf{x}. \quad (2.4)$$

Now, we can put all the terms of eq. (2.3) under the integral:

$$\int_V [\partial_j \tau_{i,j} + f_i - \rho \partial_t v_i] d^3\mathbf{x} = 0. \quad (2.5)$$

Since this holds for any volume V , the integrand has to be zero, and we obtain:

$$\partial_j \tau_{i,j} - \rho \partial_t v_i = -f_i. \quad (2.6)$$

This is the basic local form of the equation of motion.

■ 2.2.2 Equation of deformation rate

Here we consider two particles in an elastic element, called P and Q , with coordinates \mathbf{x}^P and \mathbf{x}^Q , respectively. As forces are acting on the body, each particle will have a displacement, $\mathbf{s}(\mathbf{x}, t)$, so that the particles will get a new coordinate, $\mathbf{x}'^P = \mathbf{x}^P + \mathbf{s}(\mathbf{x}^P, t)$ and $\mathbf{x}'^Q = \mathbf{x}^Q + \mathbf{s}(\mathbf{x}^Q, t)$. This displacement leads to a change in distance $d(P, Q) = \sqrt{(x_j^Q - x_j^P)(x_j^Q - x_j^P)}$ between the two particles, which is approximately:

$$\{d(P', Q')\}^2 \approx \{d(P, Q)\}^2 + 2e_{p,q} (x_p^Q - x_p^P) (x_q^Q - x_q^P), \quad (2.7)$$

in which:

$$e_{p,q} = \frac{1}{2} (\partial_p s_q + \partial_q s_p + \partial_p s_k \partial_q s_k), \quad (2.8)$$

and where $d(P, Q)$ denotes the distance between P and Q . Usually however, $|\partial_p s_k| \ll 1$, so we can neglect higher order terms. Therefore, we can write eq. (2.8) as:

$$e_{p,q} = \frac{1}{2} (\partial_p s_q + \partial_q s_p) \quad (2.9)$$

This tensor $e_{p,q}$ specifies the changes in distance between neighboring points, due to forces acting on the body. It is called the *strain tensor*. This tensor is by definition also symmetric: $e_{p,q} = e_{q,p}$.

The stress and the strain are related to each other. If the elastic material has the following properties:

- the material behaves linearly,
- the material is locally reacting,
- the material reacts instantaneously,

it is called a *perfectly elastic* material. We can write:

$$\tau_{i,j} = C_{i,j,p,q} e_{p,q}, \quad (2.10)$$

where $C_{i,j,p,q}$ represents the 81 components of the *stiffness tensor*. From the symmetry of the stress tensor follows: $C_{i,j,p,q} = C_{j,i,p,q}$, from the symmetry of the strain tensor follows: $C_{i,j,p,q} = C_{i,j,q,p}$, and Dahlen and Tromp [1998] show that if the occurring deformations are *adiabatic*, then $C_{i,j,p,q} = C_{p,q,i,j}$. Thus the number of independent coefficients of the stiffness tensor are reduced to 21. If the material is *isotropic*, the number of independent coefficients reduces to two, and we can write:

$$C_{i,j,p,q} = \lambda \delta_{i,j} \delta_{p,q} + \mu (\delta_{i,p} \delta_{j,q} + \delta_{i,q} \delta_{j,p}), \quad (2.11)$$

The coefficients λ and μ are known as the *Lamé coefficients*.

When eq. (2.10) is differentiated with respect to time, we arrive at the linearized equation of deformation rate:

$$\partial_t \tau_{i,j} = C_{i,j,p,q} (\partial_p v_q - h_{p,q}), \quad (2.12)$$

where we made use of the property that the strain tensor is symmetric. We also introduced an *external* part of the deformation rate, $h_{p,q}$, that is representative for the action of external sources that impress a deformation rate to the solid. This $h_{p,q}$ is called the *volume source density of deformation rate*.

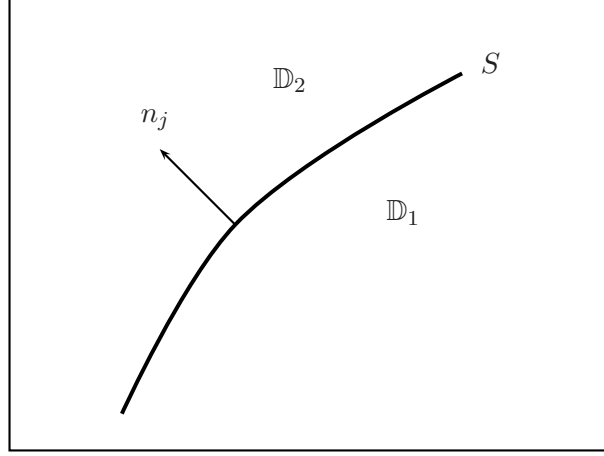


Figure 2.1: Boundary S between two adjacent media.

■ 2.2.3 Boundary conditions

At some points in the elastic medium, its material properties may show discontinuities. There, the elastic wavefield quantities are not continuously differentiable, and eq. (2.6) and eq. (2.12) are no longer valid. At these points, boundary conditions are needed to supplement these equations. It is assumed that these discontinuities consist of a jump by a finite amount in the material parameters, across a boundary surface S .

Let S be a surface between two adjacent media, \mathbb{D}_1 and \mathbb{D}_2 , that have different material properties. The vector n_j is the normal to S , pointing away from \mathbb{D}_1 (see Figure 2.1). Then the following conditions hold:

$$\text{The particle velocity } v_i \text{ is continuous across } S, \quad (2.13)$$

$$\text{The traction } \tau_{i,j}n_j \text{ is continuous across } S. \quad (2.14)$$

A special but very important boundary condition is given when the medium \mathbb{D}_2 consists of a vacuum. Then, the boundary S is a free surface, and the following boundary condition holds:

$$\text{The traction vanishes at } S, \text{ i.e. } \tau_{i,j}n_j = 0 \quad \text{at } S. \quad (2.15)$$

2.3 Equations in the Laplace domain

We introduce the symmetrical unit tensor of rank four as:

$$\Delta_{i,j,p,q}^+ = \frac{1}{2} (\delta_{i,p}\delta_{j,q} + \delta_{j,p}\delta_{i,q}). \quad (2.16)$$

With this, eq. (2.6) and eq. (2.12) are rewritten in a slightly different form:

$$\Delta_{i,j,p,q}^+ \partial_j \tau_{p,q}(\mathbf{x}, t) - \rho(\mathbf{x}) \partial_t v_i(\mathbf{x}, t) = -f_i(\mathbf{x}, t), \quad (2.17)$$

$$\Delta_{i,j,p,q}^+ \partial_p v_q(\mathbf{x}, t) - S_{i,j,p,q}(\mathbf{x}) \partial_t \tau_{p,q}(\mathbf{x}, t) = h_{i,j}(\mathbf{x}, t), \quad (2.18)$$

in which

$$\begin{aligned} \tau_{i,j}(\mathbf{x}, t) &= \text{elastic stress tensor [Pa]}, \\ v_i(\mathbf{x}, t) &= \text{particle velocity [m/s]}, \\ \rho(\mathbf{x}) &= \text{volume density of mass [kg/m}^3\text{]}, \\ S_{i,j,p,q}(\mathbf{x}) &= \text{compliance tensor [Pa}^{-1}\text{]}, \\ f_i(\mathbf{x}, t) &= \text{volume source density of force [N/m}^3\text{]}, \\ h_{i,j}(\mathbf{x}, t) &= \text{volume source density of deformation rate [s}^{-1}\text{]}. \end{aligned}$$

The compliance tensor is the inverse of the stiffness tensor, and has the same symmetry relations. Specifically, the relation between them is:

$$S_{i,j,m,n} C_{m,n,p,q} = \Delta_{i,j,p,q}^+. \quad (2.19)$$

We assume that before a certain time, called $t = 0$, the elastic medium is in a state of equilibrium. The medium is then excited by the sources. Due to causality, changes in the elastic wavefield properties can only occur after this excitation. Under these circumstances, it is mathematically advantageous to perform a Laplace transformation with respect to time on eq. (2.17) and eq. (2.18), since this will eliminate the time coordinate. Taking into account that $\partial_t \rightarrow s$, when performing a Laplace transformation (defined in Appendix A.1), we find:

$$\Delta_{i,j,p,q}^+ \partial_j \hat{\tau}_{p,q}(\mathbf{x}, s) - s\rho(\mathbf{x}) \hat{v}_i(\mathbf{x}, s) = -\hat{f}_i(\mathbf{x}, s), \quad (2.20)$$

$$\Delta_{i,j,p,q}^+ \partial_p \hat{v}_q(\mathbf{x}, s) - sS_{i,j,p,q}(\mathbf{x}) \hat{\tau}_{p,q}(\mathbf{x}, s) = \hat{h}_{i,j}(\mathbf{x}, s). \quad (2.21)$$

This formulation is the most convenient one for deriving the Betti-Rayleigh reciprocity theorem.

2.4 Elastic waves in an unbounded homogeneous medium

This section derives a differential equation for the particle velocity in an unbounded homogeneous elastic medium, induced by both volume sources of force and volume sources of deformation rate. The stress components $\hat{\tau}_{i,j}$ are eliminated by substituting eq. (2.21) into eq. (2.20) and using eq. (2.19). This way, we obtain the two-way wave equation for the particle velocity components \hat{v}_i :

$$\partial_j C_{i,j,p,q} \partial_p \hat{v}_q - s^2 \rho \hat{v}_i = \partial_j C_{i,j,p,q} \hat{h}_{p,q} - s \hat{f}_i. \quad (2.22)$$

When a homogeneous, isotropic medium is assumed, eq. (2.11) can be substituted. When we also divide by ρ , we obtain:

$$\frac{\lambda + 2\mu}{\rho} \partial_i \partial_p \hat{v}_p - \frac{\mu}{\rho} \partial_i \partial_p \hat{v}_p + \frac{\mu}{\rho} \partial_p \partial_p \hat{v}_i - s^2 \hat{v}_i = -\hat{Q}_i, \quad (2.23)$$

where $\hat{Q}_i = \frac{s}{\rho} \hat{f}_i - \frac{C_{i,j,p,q}}{\rho} \partial_j \hat{h}_{p,q}$ describes the source terms. This last equation can also be written as:

$$\frac{\lambda + 2\mu}{\rho} \partial_i \partial_p \hat{v}_p - \frac{\mu}{\rho} \varepsilon_{i,j,k} \partial_j (\varepsilon_{k,p,q} \partial_p \hat{v}_q) - s^2 \hat{v}_i = -\hat{Q}_i. \quad (2.24)$$

This is a wave equation, and it tells us, that the wavefield consists of a curl-free part (since the curl of a gradient is zero) that travels with a velocity of $\sqrt{(\lambda + 2\mu)/\rho}$, and a divergence-free part (since the divergence of a curl is zero) that travels with a velocity of $\sqrt{\mu/\rho}$. The curl-free part relates to the P-waves, and the divergence-free part to the S-waves. We then define the P-wave velocity c_p and the S-wave velocity c_s as:

$$c_p = \sqrt{\frac{\lambda + 2\mu}{\rho}}, \quad (2.25)$$

$$c_s = \sqrt{\frac{\mu}{\rho}}, \quad (2.26)$$

and observe that in any elastic medium, the S-wave velocity is always lower than the P-wave velocity.

It is customary to introduce a P-wave potential Φ and an S-wave potential Ψ_k according to:

$$\hat{v}_i = \partial_i \Phi + \varepsilon_{i,j,k} \partial_j \Psi_k. \quad (2.27)$$

Φ and Ψ_k are called *Lamé potentials* (Berkhout [1987]). These potentials are four functions, that together describe the three components of the particle velocity. Hence, without loss of generality, we can define Ψ_i to be divergence free: $\partial_i \Psi_i = 0$. When we take into account the rule for double curls (which, in tensor notation, reads $\varepsilon_{i,j,k} \partial_j (\varepsilon_{k,m,n} \partial_m \Psi_n) = \partial_i \partial_j \Psi_j - \partial_j \partial_j \Psi_i$), eq. (2.24) becomes:

$$c_p^2 \partial_i \left(\partial_p \partial_p \Phi - \frac{s^2}{c_p^2} \Phi \right) + c_s^2 \varepsilon_{i,j,k} \partial_j \left(\partial_p \partial_p \Psi_k - \frac{s^2}{c_s^2} \Psi_k \right) = -\hat{Q}_i. \quad (2.28)$$

This equation demonstrates even more clearly the separation between P-waves and S-waves, and shows that both wave types are governed by a Helmholtz wave equation.

It is customary to distinguish between S-waves polarized in a vertical plane (called SV-waves) and horizontally polarized S-waves (called SH-waves). Assume a wave propagating in the (x_1, x_3) -plane, then for a compressional wave (whose particle motion is perpendicular to the wave front) we can write:

$$\begin{aligned} \hat{v}_1 &= \partial_1 \Phi, \\ \hat{v}_2 &= 0, \\ \hat{v}_3 &= \partial_3 \Phi, \end{aligned} \quad (2.29)$$

and for SV-waves:

$$\begin{aligned} \hat{v}_1 &= -\partial_3 \Psi_2, \\ \hat{v}_2 &= 0, \\ \hat{v}_3 &= \partial_1 \Psi_2, \end{aligned} \quad (2.30)$$

and finally, for SH-waves:

$$\begin{aligned} \hat{v}_1 &= 0, \\ \hat{v}_2 &= \partial_3 \Psi_1 - \partial_1 \Psi_3, \\ \hat{v}_3 &= 0. \end{aligned} \quad (2.31)$$

We have now distinguished three different wave types, which in an unbounded, homogeneous, isotropic and source-free medium propagate fully independently. When a medium is layered (but independent of the x_2 -direction), P-waves and SV-waves will interact at the boundaries of these

layers. SH-waves, however, have a different polarization, and do not interact with the P- and SV-waves at such boundaries.

Of course, in general inhomogeneous media, SV- and SH-waves cannot be distinguished, and all three wave types are coupled. For the scope of this thesis, however, we assume that SH-waves are decoupled from P- and SV-waves. Most generally, this is the case when a medium is invariant in the crossline (x_2) direction, when we use point-sources and when we look at the waves propagating in the (x_1, x_3) -plane. But it is also true when we use line-sources in such a medium.

2.5 The Betti-Rayleigh reciprocity theorem

Reciprocity, in general terms, is a mathematical tool to relate two non-identical states in the same spatial domain \mathbb{V} to each other. Here, these states are wavefields in elastic media. The two states are labeled with superscripts A and B . Thus, for state A we have:

$$\Delta_{i,j,p,q}^+ \partial_j \hat{\tau}_{p,q}^A(\mathbf{x}, s) - s\rho^A(\mathbf{x}) \hat{v}_i^A(\mathbf{x}, s) = -\hat{f}_i^A(\mathbf{x}, s), \quad (2.32)$$

$$\Delta_{i,j,p,q}^+ \partial_p \hat{v}_q^A(\mathbf{x}, s) - sS_{i,j,p,q}^A(\mathbf{x}) \hat{\tau}_{p,q}^A(\mathbf{x}, s) = \hat{h}_{i,j}^A(\mathbf{x}, s), \quad (2.33)$$

and for state B we have:

$$\Delta_{i,j,p,q}^+ \partial_j \hat{\tau}_{p,q}^B(\mathbf{x}, s) - s\rho^B(\mathbf{x}) \hat{v}_i^B(\mathbf{x}, s) = -\hat{f}_i^B(\mathbf{x}, s), \quad (2.34)$$

$$\Delta_{i,j,p,q}^+ \partial_p \hat{v}_q^B(\mathbf{x}, s) - sS_{i,j,p,q}^B(\mathbf{x}) \hat{\tau}_{p,q}^B(\mathbf{x}, s) = \hat{h}_{i,j}^B(\mathbf{x}, s). \quad (2.35)$$

In case of discontinuities in the material parameters, boundary conditions, such as discussed in Section 2.2.3, are needed. As one can see, one elastic state is actually a combination of three states: the field state ($\hat{\tau}_{i,j}$ and \hat{v}_i), the material state (ρ and $S_{i,j,p,q}$) and the source state (\hat{f}_i and $\hat{h}_{i,j}$). Instead of giving eqs. (2.32)–(2.35) each time, the states can be summarized in a reciprocity table, such as Table 2.1.

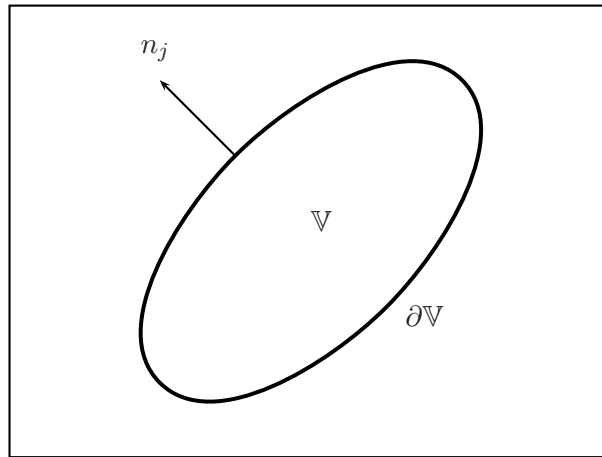
For simplicity, we drop the (\mathbf{x}, s) -dependence in the notation. We define the scalar interaction quantity between the two states as:

$$\begin{aligned} \Delta_{i,j,p,q}^+ \partial_i (\hat{\tau}_{p,q}^A \hat{v}_j^B - \hat{\tau}_{p,q}^B \hat{v}_j^A) = \\ \hat{v}_j^B \Delta_{i,j,p,q}^+ \partial_i \hat{\tau}_{p,q}^A + \hat{\tau}_{p,q}^A \Delta_{i,j,p,q}^+ \partial_i \hat{v}_j^B - \hat{v}_j^A \Delta_{i,j,p,q}^+ \partial_i \hat{\tau}_{p,q}^B - \hat{\tau}_{p,q}^B \Delta_{i,j,p,q}^+ \partial_i \hat{v}_j^A. \end{aligned} \quad (2.36)$$

Table 2.1: States in the elastodynamic reciprocity theorem.

	State A	State B
Field state	$\{\hat{\tau}_{i,j}^A, \hat{v}_i^A\}(\mathbf{x}, s)$	$\{\hat{\tau}_{i,j}^B, \hat{v}_i^B\}(\mathbf{x}, s)$
Material state	$\{\rho^A, S_{i,j,p,q}^A\}(\mathbf{x})$	$\{\rho^B, S_{i,j,p,q}^B\}(\mathbf{x})$
Source state	$\{\hat{h}_{p,q}^A, \hat{f}_i^A\}(\mathbf{x}, s)$	$\{\hat{h}_{p,q}^B, \hat{f}_i^B\}(\mathbf{x}, s)$
Domain \mathbb{V}		

Substituting eqs. (2.32)—(2.35) into this last equation and using the symme-

**Figure 2.2:** Configuration of domain \mathbb{V} for the application of the reciprocity theorem.

try properties of the stress tensor to eliminate the $\Delta_{i,j,p,q}^+$ tensor, we obtain:

$$\begin{aligned} \partial_j (\hat{\tau}_{i,j}^A \hat{v}_i^B - \hat{\tau}_{i,j}^B \hat{v}_i^A) = \\ s (S_{i,j,p,q}^B - S_{p,q,i,j}^A) \hat{\tau}_{i,j}^A \hat{\tau}_{p,q}^B - s (\rho^B - \rho^A) \hat{v}_i^A \hat{v}_i^B \\ + \hat{f}_i^B \hat{v}_i^A + \hat{h}_{i,j}^B \hat{\tau}_{i,j}^A - \hat{f}_i^A \hat{v}_i^B - \hat{h}_{i,j}^A \hat{\tau}_{i,j}^B. \end{aligned} \quad (2.37)$$

This is the *local* form of the elastic reciprocity theorem.

The *global* form of the reciprocity theorem is obtained by integrating eq. (2.37) over the volume \mathbb{V} , which is bounded by the surface $\partial\mathbb{V}$ and where the normal n_j is pointing outward (see Figure 2.2), and by applying Gauss' integral theorem. This leads to:

$$\begin{aligned} \oint_{\mathbf{x} \in \partial\mathbb{V}} (\hat{\tau}_{i,j}^A \hat{v}_i^B - \hat{\tau}_{i,j}^B \hat{v}_i^A) n_j d^2\mathbf{x} = \\ \int_{\mathbf{x} \in \mathbb{V}} [s (S_{i,j,p,q}^B - S_{p,q,i,j}^A) \hat{\tau}_{i,j}^A \hat{\tau}_{p,q}^B - s (\rho^B - \rho^A) \hat{v}_i^A \hat{v}_i^B] d^3\mathbf{x} + \\ \int_{\mathbf{x} \in \mathbb{V}} [\hat{f}_i^B \hat{v}_i^A + \hat{h}_{i,j}^B \hat{\tau}_{i,j}^A - \hat{f}_i^A \hat{v}_i^B - \hat{h}_{i,j}^A \hat{\tau}_{i,j}^B] d^3\mathbf{x}. \end{aligned} \quad (2.38)$$

This equation is the elastic field reciprocity in its global form for the domain \mathbb{V} , and is also known as the *Betti-Rayleigh reciprocity theorem*.

2.6 Application of reciprocity: physical reciprocity

In marine, acoustic seismics, missing traces can be replaced by traces from other shots, where source and receiver positions are swapped. This swapping of source and receiver positions is called *physical reciprocity*, and can be done because both sources and receivers are omni-directional. With elastic seismics, this is obviously not the case. However, a similar form of physical reciprocity is possible, and will be derived here.

We start by defining the sources for the two states. In state A , there is a point source of force, pointing specifically in the x_m direction, while in state B , there is a point source of force, pointing specifically in the x_n direction. These sources are denoted for example by: $\hat{f}_i(\mathbf{x}, s) = \hat{f}^n(s) \delta_{i,n} \delta(\mathbf{x} - \mathbf{x}^S)$. The Kronecker delta implies, that should a summation over i occur, then there is only a contribution when i equals n , and the superscript n is just a reminder that this source points in the x_n direction.

The resulting wavefield quantities due to these sources will be described with an extra subscript, i.e. $\hat{\tau}_{i,j;n}$ and $\hat{v}_{i;n}$, which means that the wavefields

Table 2.2: States for determining physical reciprocity.

	State A	State B
Field state	$\left\{ \hat{\tau}_{i,j;n}^A, \hat{v}_{i;n}^A \right\} (\mathbf{x} \mathbf{x}^A, s)$	$\left\{ \hat{\tau}_{i,j;m}^B, \hat{v}_{i;m}^B \right\} (\mathbf{x} \mathbf{x}^B, s)$
Material state	$\{ \rho, S_{i,j,p,q} \} (\mathbf{x})$	$\{ \rho, S_{i,j,p,q} \} (\mathbf{x})$
Source state	$\left\{ 0, \hat{f}^{A,n}(s) \delta_{i,n} \right\} \delta(\mathbf{x} - \mathbf{x}^A)$	$\left\{ 0, \hat{f}^{B,m}(s) \delta_{i,m} \right\} \delta(\mathbf{x} - \mathbf{x}^B)$
Domain \mathbb{R}^3		

are caused by a source pointing specifically in the x_n direction. The position dependence of the wavefield quantities are denoted for example as: $\hat{v}_{i;n}(\mathbf{x}^R | \mathbf{x}^S, s)$, which means as much as the x_i component of the particle velocity measured at position \mathbf{x}^R , caused by a source at position \mathbf{x}^S (which is pointing in the x_n direction).

The domain of integration is the complete three dimensional space \mathbb{R}^3 . The material parameters are the same for both states. The states are summarized in Table 2.2, and substituted in eq. (2.38). When we assume adiabatic processes, the symmetry property $S_{i,j,p,q} = S_{p,q,i,j}$ holds (Dahlen and Tromp [1998]). Therefore the integral with the differences in material parameters vanishes. The integral over the surface (the left hand side of eq. (2.38)) at infinity yields zero, due to causality (Fokkema and van den Berg [1993]).

We obtain:

$$\hat{f}^{B,m}(s) \hat{v}_{m;n}^A(\mathbf{x}^B | \mathbf{x}^A, s) = \hat{f}^{A,n}(s) \hat{v}_{n;m}^B(\mathbf{x}^A | \mathbf{x}^B, s), \quad (2.39)$$

When we take equal source signatures $\hat{f}^{A,n}(s) = \hat{f}^{B,m}(s)$, we get:

$$\hat{v}_{m;n}^A(\mathbf{x}^B | \mathbf{x}^A, s) = \hat{v}_{n;m}^B(\mathbf{x}^A | \mathbf{x}^B, s). \quad (2.40)$$

This equation implies that the x_m component of the particle velocity at point \mathbf{x}^B , caused by a source in the x_n direction at point \mathbf{x}^A is the same as the x_n component of the particle velocity at point \mathbf{x}^A , caused by a source in the x_m direction at point \mathbf{x}^B . Or, in other words, source and receiver positions can be swapped, but then the indices have to be swapped, too.

Removal of Love waves from land seismic SH-wave reflection data

In this chapter, we take the Betti-Rayleigh reciprocity theorem and derive an expression that removes the effects of the stress-free surface from land seismic data. We do that for the decoupled case of SH-waves only. The two states that are defined for the use in the reciprocity integral are an actual state and a desired state. The actual state has a stress free surface, which, in the case of SH-waves, is a perfectly reflecting boundary. It is the cause of all sorts of surface effects, such as Love waves. The desired state distinguishes itself from the actual state only in the sense that it lacks a surface. Hence, no surface effects are possible in this configuration.

The final expression is an integral equation of the second kind, and it solves the wavefield without surface effects from the actual wavefield that does contain such effects. After discretization, the integral equation becomes a matrix equation that can be solved by for example a direct matrix inversion. When a horizontally layered medium is assumed, the kernel of the matrix equation becomes diagonal after a double Fourier transformation to the horizontal slowness domain. An efficient suppression procedure is then derived.

3.1 Reciprocity theorem for SH-waves

Since this chapter only considers the decoupled case of SH-waves, it is not necessary to take all terms of the Betti-Rayleigh reciprocity theorem, eq. (2.38), into account. Also, since a source of force density in the crossline (x_2) direction generates only SH-waves in the (x_1, x_3) -plane, we take only this kind of source, and the notation introduced in Section 2.6 (see Table 2.2 and eq. (2.40)) is omitted in this chapter. Furthermore, since both states we describe have the same material properties for the domain of integration, there is no difference in the material parameters. Lastly, for reasons of simplicity, we take x_2 -invariant media and use line sources from now on. Summarizing this, and applying it to the Betti-Rayleigh integral, leads to:

$$\oint_{\mathbf{x} \in \partial\mathbb{V}} (\hat{\tau}_{2,j}^A \hat{v}_2^B - \hat{\tau}_{2,j}^B \hat{v}_2^A) n_j d\mathbf{x} = \int_{\mathbf{x} \in \mathbb{V}} [\hat{f}_2^B \hat{v}_2^A - \hat{f}_2^A \hat{v}_2^B] d^2\mathbf{x}. \quad (3.1)$$

In this equation, \mathbb{V} is a two-dimensional plane, instead of a volume like in eq. (2.38), and similarly, $\partial\mathbb{V}$ is its one-dimensional closed path. This equation is the starting point of our analysis in the remainder of this chapter.

3.2 Description of the reciprocity states

We describe the two states for the reciprocity theorem here. They are: a state with a stress free surface, and a state without it. Therefore, from now on, quantities related to state A will have the superscript *surf*, and quantities related to state B will have the superscript *nosurf*.

■ 3.2.1 The actual state - with a stress free surface

In the actual configuration, we assume that there is a homogeneous and isotropic layer with an arbitrarily shaped lower boundary on top of other earth layers, which may be arbitrarily inhomogeneous and anisotropic. This top layer is bounded at $x_3 = 0$ by a stress-free surface, i.e. we imposed the boundary condition of eq. (2.15). When this top layer has a shear-wave velocity lower than the layers underneath it, then that is the configuration where Love waves can occur. However, the shear wave velocity does not have to be lower to achieve suppression of the surface effects, it just means that the surface effects will be different. We denote the domain of the top layer by \mathbb{D} , and the domain of the remainder of the configuration by \mathbb{D}' . Figure 3.1 shows a graphical representation of this configuration.

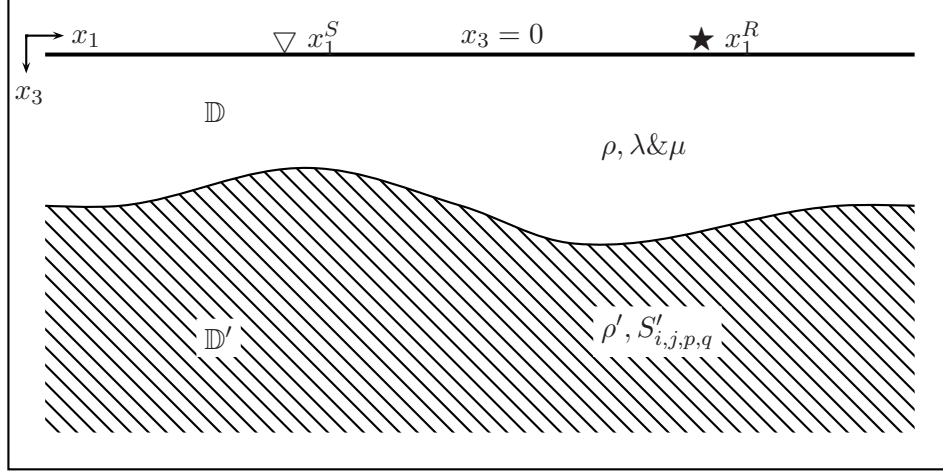


Figure 3.1: The actual state for the reciprocity theorem.

The sources and receivers are placed on the stress-free surface $x_3 = 0$. The receiver is placed on a position denoted with x_1^S (with S for *Source*, but the reason for this will become clear later). It is a little hard to define a *volume* source density of force, when it is located exactly on the stress-free surface. Instead we choose to define the source as a boundary condition in the stress field. This means that the surface is stress-free, except at a certain point $x_1 = x_1^R$ (with R for *Receiver*; again, the reason for this will become clear later). Hence, the stress on the surface is given by:

$$\hat{\tau}_{2,3}^{\text{surf}}(x_1, x_3 = 0 | x_1^R, x_3^R = 0, s) = -\hat{t}_2^{\text{surf}}(s) \delta(x_1 - x_1^R), \quad (3.2)$$

where, conform eq. (2.1), \hat{t}_2 is defined as the traction on the surface in the x_2 direction. The minus sign on the right hand side comes from the fact that, in the reciprocity theorem, the normal on the surface points out of the domain of integration, which is upward in this case, while the positive x_3 direction is downward.

■ 3.2.2 The desired state - without a surface

The desired configuration differs only from the actual configuration in the sense that it lacks a stress free surface. The material properties of the top

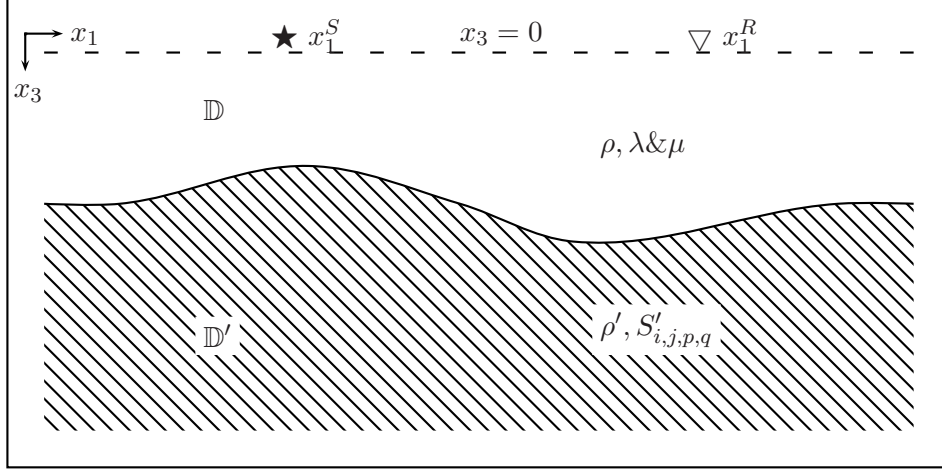


Figure 3.2: The desired state for the reciprocity theorem.

layer are extended to $x_3 \rightarrow -\infty$. This way, the plane $x_3 = 0$ is no longer a real surface, but an arbitrary reference depth level in a homogeneous half-space. This configuration is shown in Figure 3.2. It is obvious that for this configuration, no surface effects exist. The “boundary” condition on the depth level $x_3 = 0$ now consists of continuous velocity and traction across this depth level, conform eq. (2.13) and eq. (2.14).

Also in this situation, the sources and receivers are placed on the plane $x_3 = 0$. The receiver is placed on a position denoted with x_1^R , and the source is placed on a position denoted with x_1^S , i.e. the source- and receiver-positions are switched when compared to the situation of the surface state. Since the source is now surrounded by a homogeneous embedding, we can now define a source of force density in a normal fashion:

$$\hat{f}_2^{\text{nosurf}}(x_1, x_3, s) = \hat{f}_2^{\text{nosurf}}(s) \delta(x_1 - x_1^S) \delta(x_3). \quad (3.3)$$

■ 3.2.3 The domain of integration

The domain of integration is the same for both states. It is the lower half-space, $\{\mathbb{V} = \mathbb{D} \cup \mathbb{D}' \in \mathbb{R}^2 \mid -\infty < x_1 < \infty, 0 \leq x_3 < \infty\}$. The path of integration (for the left hand side of eq. (3.1)) is defined as the surface $x_3 = 0$, which is closed by a semi-circle with a radius Δ that extends to infinity in the

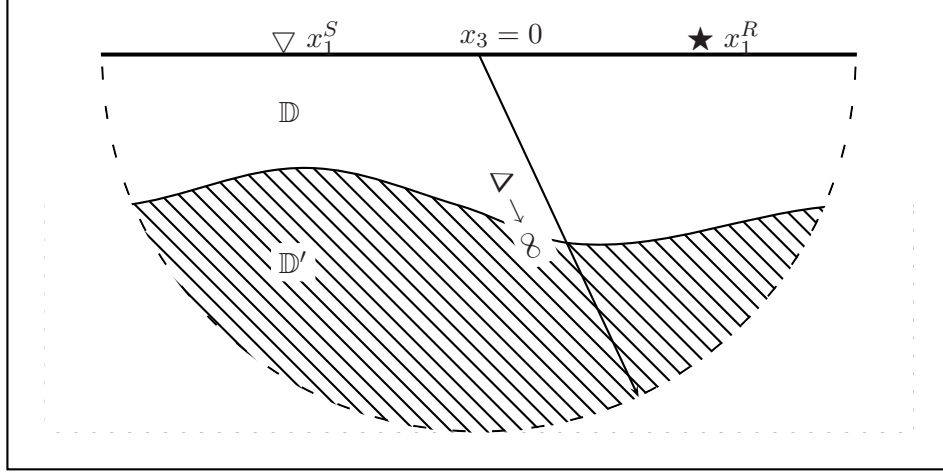


Figure 3.3: The domain of integration for the reciprocity theorem.

lower half-space. Figure 3.3 shows a graphical representation of this domain of integration. The integral over the semi-circle at infinity yields zero, due to causality (Fokkema and van den Berg [1993]), and the only contribution that remains on the left hand side of eq. (3.1) is the integral over the surface $x_3 = 0$.

3.3 Application of the reciprocity theorem

The states discussed in the previous section are summarized in Table 3.1 for quick reference. We can now substitute them into eq. (3.1). Furthermore, we apply physical reciprocity, as explained by eq. (2.40), on \hat{v}_2^{surf} . Then, we obtain the following equation:

$$\int_{x_1 \in \mathbb{R}} \hat{\tau}_{2,3}^{\text{nosurf}}(x_1, 0 | x_1^S, 0, s) \hat{v}_2^{\text{surf}}(x_1^R, 0 | x_1, 0, s) dx_1 = \frac{1}{2} \hat{f}_2^{\text{nosurf}}(s) \hat{v}_2^{\text{surf}}(x_1^R, 0 | x_1^S, 0, s) - \hat{t}_2^{\text{surf}}(s) \hat{v}_2^{\text{nosurf}}(x_1^R, 0 | x_1^S, 0, s). \quad (3.4)$$

There is no minus sign on the left hand side of this equation, because the normal of the domain of integration is pointing outward (upward, in this case), while the positive x_3 direction is downward. Therefore, that compensates for the original minus sign of $-\hat{\tau}_{2,j}^B \hat{v}_2^A$. The same reasoning goes for the minus

Table 3.1: States for the reciprocity theorem, used for the removal of Love waves. \mathbf{x}^S and \mathbf{x}^R are located on the surface $x_3 = 0$.

	State A (surface state)	State B (no-surface state)
Field state	$\{\hat{\tau}_{2,j}^{\text{surf}}, \hat{v}_2^{\text{surf}}\}(\mathbf{x} \mathbf{x}^R, s)$	$\{\hat{\tau}_{2,j}^{\text{nosurf}}, \hat{v}_2^{\text{nosurf}}\}(\mathbf{x} \mathbf{x}^S, s)$
Material state	$\{\rho, \lambda \& \mu\}$ in \mathbb{D} $\{\rho', S'_{i,j,p,q}\}$ in \mathbb{D}'	$\{\rho, \lambda \& \mu\}$ in \mathbb{D} $\{\rho', S'_{i,j,p,q}\}$ in \mathbb{D}'
Source state	$\{0, 0\}$	$\{0, \hat{f}_2^{\text{nosurf}}(s) \times \delta(x_1 - x_1^S) \delta(x_3)\}$
Surface state	Stress-free except at $x_1 = x_1^R$: $\hat{\tau}_{2,3}^{\text{surf}} = -\hat{t}_2^{\text{surf}}(s) \times \delta(x_1 - x_1^R)$	Continuous velocity and traction
Domain $\mathbb{V} = \mathbb{D} \cup \mathbb{D}'$ (see Figure 3.3)		

sign in the second term on the right hand side of the equation. The factor $\frac{1}{2}$ in the first term on the right hand side is the result of integrating over a delta function located exactly on the boundary of the domain of integration (the surface $x_3 = 0$).

We take equal source function in both states:

$$\hat{f}_2^{\text{nosurf}}(s) = \hat{t}_2^{\text{surf}}(s) = \hat{f}_2(s), \quad (3.5)$$

and apply Parseval's theorem to eq. (3.4):

$$\begin{aligned} \frac{1}{2\pi} \int_{s\alpha_1 \in \mathbb{R}} \tilde{\tau}_{2,3}^{\text{nosurf}}(js\alpha_1, 0|x_1^S, 0, s) \bar{v}_2^{\text{surf}}(x_1^R, 0|js\alpha_1, 0, s) ds\alpha_1 = \\ \frac{1}{2} \hat{f}_2(s) \hat{v}_2^{\text{surf}}(x_1^R, 0|x_1^S, 0, s) - \hat{f}_2(s) \hat{v}_2^{\text{nosurf}}(x_1^R, 0|x_1^S, 0, s). \end{aligned} \quad (3.6)$$

Notice that we used two different Fourier transforms in this equation. We used one Fourier transform with respect to the receiver coordinates (denoted by the tilde \sim), and one with respect to the source coordinates (denoted by the bar $\bar{}$). These Fourier transforms are explained in Appendix A.2.

From eq. (3.6), we want to solve for the term $\hat{v}_2^{\text{nosurf}}(x_1^R, 0|x_1^S, 0, s)$. When the term $\hat{v}_2^{\text{surf}}(x_1^R, 0|x_1^S, 0, s)$ is the measured data and the source wavelet $\hat{f}_2(s)$ is known, then the only other unknown term in eq. (3.6) is the stress component $\hat{\tau}_{2,3}^{\text{nosurf}}(js\alpha_1, 0|x_1^S, 0, s)$. Finding a suitable expression for this term is the scope of the next section.

■ 3.3.1 The stress in terms of velocity

The term $\hat{\tau}_{2,3}^{\text{nosurf}}$ is an unknown term in eq. (3.4). It can be rewritten in terms of velocity with the help of the equation of deformation, eq. (2.21). We restate that equation, but without sources of deformation rate, and take only the necessary component:

$$\hat{\tau}_{2,3}^{\text{nosurf}} = \frac{\mu}{s} \partial_3 \hat{v}_2^{\text{nosurf}}. \quad (3.7)$$

The differentiation to the x_3 coordinate cannot be performed in the space-Laplace domain, because, in a land seismic survey, there are only receivers on one level: the surface $x_3 = 0$. But in the horizontal slowness domain, we have more convenient expressions for the wave field. From Appendix B.1 we see that a differentiation to the x_3 coordinate becomes a multiplication with either $+s\gamma_s$ or $-s\gamma_s$ in the horizontal slowness domain. γ_s is defined as:

$$\gamma_s = \sqrt{\frac{1}{c_s^2} + \alpha_1^2}, \quad \text{Re}(\gamma_s) > 0. \quad (3.8)$$

The sign of this multiplication depends on a differentiation of an up-going or down-going wavefield, respectively.

Therefore, to determine whether to use the multiplication with $+s\gamma_s$ or $-s\gamma_s$, we split the wavefield $\hat{v}_2^{\text{nosurf}}$ into components of which we can easily determine whether they are up- or down-going. These components are the incident and the reflected wavefield:

$$\hat{v}_2^{\text{nosurf}} = \hat{v}_2^{\text{inc}} + \hat{v}_2^{\text{ref}}. \quad (3.9)$$

Figure 3.4 shows a graphical representation of these two components of the no-surface wavefield. The vertical derivative of the incident wavefield is zero,

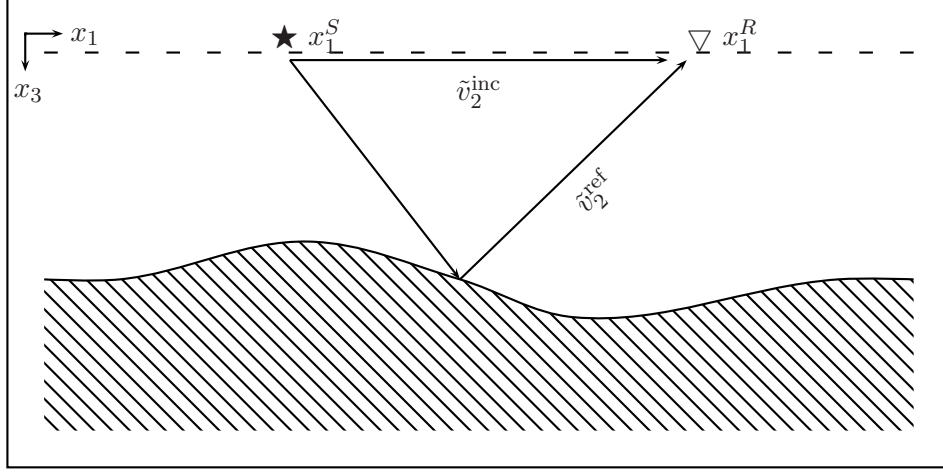


Figure 3.4: The incident and reflected wavefield in absence of a stress-free surface.

because the sources and receivers are at the same level (namely, the surface $x_3 = 0$). Exactly on this level, the wavefield is neither up-going nor down-going (as shown in Figure 3.4). Mathematically, the same outcome can be shown. For this we look at eq. (B.10). When we take the vertical derivative, we see that: $\partial_3 \tilde{v}_2^{\text{inc}} = -\text{sign}(x_3) s \gamma_s \tilde{v}_2^{\text{inc}}$. Therefore, $\partial_3 \tilde{v}_2^{\text{inc}} = 0$, because the sign-function is defined such that $\text{sign}(x_3) = 0$ for $x_3 = 0$. Figure 3.4 also shows that the reflected wavefield is purely up-going in the no-surface situation. We find that $\partial_3 \tilde{v}_2^{\text{ref}} = s \gamma_s \tilde{v}_2^{\text{ref}}$. We find for eq. (3.7):

$$\tilde{\tau}_{2,3}^{\text{nosurf}} = \frac{\mu}{s} \partial_3 \left(\tilde{v}_2^{\text{inc}} + \tilde{v}_2^{\text{ref}} \right) = \mu \gamma_s \left(\tilde{v}_2^{\text{nosurf}} - \tilde{v}_2^{\text{inc}} \right), \quad \text{for } x_3 = 0. \quad (3.10)$$

With this, the goal of writing the stress-field in terms of velocity is complete. The term $\tilde{v}_2^{\text{nosurf}}$ is the unknown term that we are looking for, and the term \tilde{v}_2^{inc} is known. We can write for the latter term (see Appendix B.1):

$$\tilde{v}_2^{\text{inc}}(js\alpha_1, 0|x_1^S, 0, s) = \frac{\hat{f}_2(s)}{2\mu\gamma_s} e^{js\alpha_1 x_1^S}. \quad (3.11)$$

■ 3.3.2 Integral equation of the second kind for the no-surface wavefield

The final expression is achieved when we substitute eq. (3.10) into eq. (3.6):

$$\begin{aligned} \frac{1}{2\pi} \int_{s\alpha_1 \in \mathbb{R}} \frac{\mu\gamma_s}{\hat{f}_2(s)} \left(\tilde{v}_2^{\text{nosurf}} - \tilde{v}_2^{\text{inc}} \right) (js\alpha_1, 0|x_1^S, 0, s) \tilde{v}_2^{\text{surf}}(x_1^R, 0|js\alpha_1, 0, s) ds\alpha_1 = \\ \frac{1}{2} \hat{v}_2^{\text{surf}}(x_1^R, 0|x_1^S, 0, s) - \hat{v}_2^{\text{nosurf}}(x_1^R, 0|x_1^S, 0, s). \end{aligned} \quad (3.12)$$

When we substitute the equation for the incident SH-wavefield, eq. (3.11), into this last equation, we find that this part represents exactly an inverse Fourier transformation from the horizontal slowness domain to the space-Laplace domain, with regard to the source coordinates, i.e.

$$\begin{aligned} -\frac{1}{2\pi} \int_{s\alpha_1 \in \mathbb{R}} \frac{\mu\gamma_s}{\hat{f}_2(s)} \tilde{v}_2^{\text{inc}}(js\alpha_1, 0|x_1^S, 0, s) \tilde{v}_2^{\text{surf}}(x_1^R, 0|js\alpha_1, 0, s) ds\alpha_1 = \\ -\frac{1}{2} \hat{v}_2^{\text{surf}}(x_1^R, 0|x_1^S, 0, s). \end{aligned} \quad (3.13)$$

With this, we reach our final expression:

$$\begin{aligned} \frac{1}{2\pi} \int_{s\alpha_1 \in \mathbb{R}} \frac{\mu\gamma_s}{\hat{f}_2(s)} \tilde{v}_2^{\text{surf}}(x_1^R, 0|js\alpha_1, 0, s) \tilde{v}_2^{\text{nosurf}}(js\alpha_1, 0|x_1^S, 0, s) ds\alpha_1 = \\ \hat{v}_2^{\text{surf}}(x_1^R, 0|x_1^S, 0, s) - \hat{v}_2^{\text{nosurf}}(x_1^R, 0|x_1^S, 0, s). \end{aligned} \quad (3.14)$$

This is an integral equation of the second kind, meaning that the unknown term ($\hat{v}_2^{\text{nosurf}}$) is both inside and outside the integral. In order to solve for $\hat{v}_2^{\text{nosurf}}$, the following input is needed: the measured data with the surface effects (\hat{v}_2^{surf}), the source wavelet ($\hat{f}_2(s)$), and the material parameters of the top layer (via $\mu\gamma_s$). No model is needed for the structure of the first layer (or further earth layers for that matter).

Intermezzo - A Neumann expansion series

In this section, we derived an integral equation of the second kind, eq. (3.14), where we could solve the no-surface wavefield from the input surface wavefield. In the space-Laplace domain, this equation can be written as:

$$\begin{aligned} \int_{x_1 \in \mathbb{R}} \hat{K}(x_1^R, 0|x_1, 0, s) \hat{v}_2^{\text{nosurf}}(x_1, 0|x_1^S, 0, s) dx_1 = \\ \hat{v}_2^{\text{surf}}(x_1^R, 0|x_1^S, 0, s) - \hat{v}_2^{\text{nosurf}}(x_1^R, 0|x_1^S, 0, s), \end{aligned} \quad (3.15)$$

in which \hat{K} is called the *kernel* of the integral equation, and is defined as:

$$\hat{K}(x_1^R, 0|x_1, 0, s) = \mathcal{F}_S^{-1} \left\{ \frac{\mu\gamma_s}{\hat{f}_2(s)} \mathcal{F}_S \left\{ \hat{v}_2^{\text{surf}}(x_1^R, 0|x_1, 0, s) \right\} \right\}. \quad (3.16)$$

One possible way to solve an integral equation of the second kind, is a Neumann expansion series, as van Borselen [1995] proposes in his thesis. In our case, the Neumann series would be defined as:

$$\hat{v}_2^{\text{nosurf}}(x_1^R, 0|x_1^S, 0, s) = \sum_{n=0}^{\infty} \hat{v}_2^{\text{nosurf},(n)}(x_1^R, 0|x_1^S, 0, s), \quad (3.17)$$

where

$$\hat{v}_2^{\text{nosurf},(0)}(x_1^R, 0|x_1^S, 0, s) = \hat{v}_2^{\text{surf}}(x_1^R, 0|x_1^S, 0, s), \quad (3.18)$$

and

$$\begin{aligned} \hat{v}_2^{\text{nosurf},(n)}(x_1^R, 0|x_1^S, 0, s) = \\ - \int_{x_1 \in \mathbb{R}} \hat{K}(x_1^R, 0|x_1, 0, s) \hat{v}_2^{\text{nosurf},(n-1)}(x_1, 0|x_1^S, 0, s) dx_1. \end{aligned} \quad (3.19)$$

If a Neumann series expansion converges, it will converge to the right solution. Convergence, however, is not guaranteed. A sufficient condition for convergence is when the norm of the kernel is smaller than 1. For a definition of the norm of the kernel, see Appendix D. In numerical tests, the norm turned out to be as big as 10^4 in some occasions. Therefore, we cannot prove convergence with the norm condition.

Van Borselen showed that the expansion series was convergent for his case, by proving that, for data with a finite recording time, the infinite sum could be replaced by a finite one. In his case, each successive term of the Neumann series removes a higher order multiple, i.e. the first term removes the first multiple, the second term removes the second multiple, etc. Therefore, each term of the expansion series is zero before a certain time in the space-time domain. And so, an N -th order term will be zero for the whole window of observation in the data, and the Neumann series expansion can be terminated.

In our case, where we want to remove Love waves from SH-wave data, we can also look at the Love waves as “multiples”. Not propagating multiples like in the marine case, but “multiples” with the largest contribution in the evanescent field. These “multiples” are not separated in time, and the time

before which each “multiple” is zero increases only slightly with each iteration. Therefore, to remove Love waves with a Neumann expansion series, we need an order of 20 multiples or more. With a norm of the kernel in the order of 10^4 , the computations will rapidly reach machine precision. We conclude that a Neumann series expansion is not possible for the removal of Love waves from SH-wave data.

3.4 Horizontally layered media

A convenient simplification is reached, when the medium is assumed to be horizontally layered, like in Figure 3.5. This is called a 1-D configuration. In this configuration, the data is dependent on the relative distance between the source and the receivers (at least in a land configuration, where both are situated on the surface), but not on their absolute position. We can write:

$$\hat{v}_2^{\text{surf}}(x_1^R, 0 | x_1^S, 0, s) = \hat{v}_2^{\text{surf}}(x_1^R - x_1^S, 0, s). \quad (3.20)$$

We perform a Fourier transform to the horizontal slowness domain with respect to the receiver coordinates, and obtain:

$$\begin{aligned} \tilde{v}_2^{\text{surf}}(js\alpha_1^R, 0 | x_1^S, 0, s) &= \int_{x_1^R \in \mathbb{R}} \hat{v}_2^{\text{surf}}(x_1^R - x_1^S, 0, s) e^{js\alpha_1^R x_1^R} dx_1^R = \\ &\tilde{v}_2^{\text{surf}}(js\alpha_1^R, 0, s) e^{js\alpha_1^R x_1^S}. \end{aligned} \quad (3.21)$$

After applying another Fourier transform to the horizontal slowness domain, this time with respect to the source coordinates, we obtain:

$$\tilde{\tilde{v}}_2^{\text{surf}}(js\alpha_1^R, 0 | js\alpha_1^S, 0, s) = \tilde{v}_2^{\text{surf}}(js\alpha_1^R, 0, s) \cdot 2\pi\delta(s\alpha_1^R - s\alpha_1^S). \quad (3.22)$$

The same arguments are used to arrive at a similar expression for $\hat{v}_2^{\text{nosurf}}$. When we apply a double Fourier transform (one with respect to the receiver coordinates, the other with respect to the source coordinates) on eq. (3.14) and substitute eq. (3.22), we find for horizontally layered (1-D) media:

$$\begin{aligned} 2\pi \int_{s\alpha_1 \in \mathbb{R}} \frac{\mu\gamma_s}{\hat{f}_2(s)} \tilde{v}_2^{\text{surf}}(js\alpha_1^R, 0, s) \delta(s\alpha_1^R - s\alpha_1) \cdot \\ \tilde{v}_2^{\text{nosurf}}(js\alpha_1, 0, s) \delta(s\alpha_1 - s\alpha_1^S) ds\alpha_1 = \\ 2\pi \tilde{v}_2^{\text{surf}}(js\alpha_1^R, 0, s) \delta(s\alpha_1^R - s\alpha_1^S) - 2\pi \tilde{v}_2^{\text{nosurf}}(js\alpha_1^R, 0, s) \delta(s\alpha_1^R - s\alpha_1^S). \end{aligned} \quad (3.23)$$

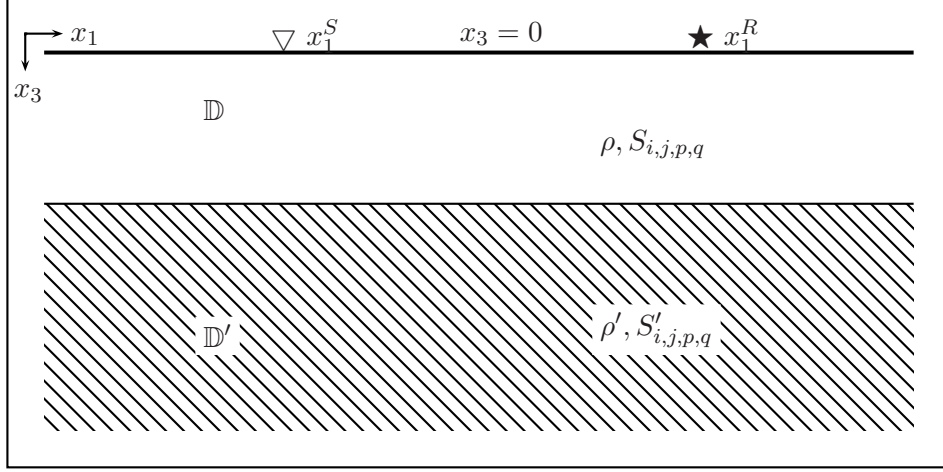


Figure 3.5: Configuration of a horizontally layered medium.

We observe that the factors 2π cancel each other, and that the integral on the left hand side only has a contribution at $s\alpha_1 = s\alpha_1^R$ due to the Dirac delta functions. The remaining delta functions also cancel each other. The equation reduces to an analytical expression:

$$\frac{\mu\gamma_s}{\hat{f}_2(s)} \tilde{v}_2^{\text{surf}}(js\alpha_1^R, 0, s) \tilde{v}_2^{\text{nosurf}}(js\alpha_1^R, 0, s) = \tilde{v}_2^{\text{surf}}(js\alpha_1^R, 0, s) - \tilde{v}_2^{\text{nosurf}}(js\alpha_1^R, 0, s). \quad (3.24)$$

In this equation, the factor γ_s is now a function of α_1^R , whereas previously, it was a function of α_1 . When we use eq. (3.11), the equation becomes:

$$\tilde{v}_2^{\text{nosurf}} = \frac{\tilde{v}_2^{\text{surf}}}{1 + \frac{\tilde{v}_2^{\text{surf}}}{2\tilde{v}_2^{\text{inc}}}}. \quad (3.25)$$

This equation represents an efficient 1-D suppression scheme to remove Love waves from data in a horizontally layered media. The integral equation is reduced to an explicit analytical expression, and only one shot-gather is needed to solve eq. (3.25).

Intermezzo - Mildly laterally varying media

The previous analysis shows that data from a horizontally layered medium, after a double Fourier transform to the horizontal slowness domains of the source- and receiver-coordinates, only has contributions when $s\alpha_1^R = s\alpha_1^S$. This implies that after discretization (see the next section), the data-matrix will be a diagonal one. It is likely that when the data comes from a mildly laterally varying medium, the matrix becomes primarily centered around the diagonal (after the double Fourier transformation, of course). This could possibly speed up computations, by using routines that incorporate special techniques for band matrices. However, the increase in efficiency is diminished by the application of the double Fourier transform. The subject has not been fully explored by the author.

For mildly laterally varying media, Verschuur [1991] proposes in his thesis to apply his multiple removal scheme on common-midpoint (CMP) sorted data. A CMP-sorting means that the data are sorted in such a way that, in each gather, the point halfway each source and receiver pair is constant. It is assumed that each reflection point in the subsurface is more or less vertically below this midpoint. When this is true, the data are considered to correspond to data from a 1-D configuration. However, due to the low velocity of shear waves (especially in soft soils), a common-shot gather can very easily be spatially aliased in SH-wave experiments. When the data are CMP-sorted, this becomes even worse, since a CMP-gather has at most half the number of traces of a common-shot gather. Therefore, applying eq. (3.25) on CMP-sorted data is unfortunately often not an option.

3.5 Numerical implementation for laterally varying media

When the data are discrete, eq. (3.14) can be written as a matrix equation. The discrete counterparts of $\hat{v}_2^{\text{surf}}(x_1^R|x_1^S, s)$ and $\hat{v}_2^{\text{nosurf}}(x_1^R|x_1^S, s)$ (where we omitted the $x_3^R = x_3^S = 0$ dependence) are denoted with bold, uppercase $\hat{\mathbf{V}}_2^{\text{surf}}$ and $\hat{\mathbf{V}}_2^{\text{nosurf}}$, respectively. For a fixed Laplace parameter s , these are two-dimensional matrices, where the organization is, from fast to slow dimension: x_1^R and x_1^S . This way, one column in the matrix $\hat{\mathbf{V}}_2^{\text{surf}}$ represents a common-source gather (data where the source position is constant), while one row represents a common-receiver gather (data where the receiver position is constant). When these matrices are square, it greatly simplifies the performance of matrix operations such as multiplication or inversion. This

matrix notation was introduced by Berkhout [1982].

As a next step, we examine the operation $\mu\gamma_s$ in eq. (3.14). It is the result of writing the no-surface stress-field, $\hat{\tau}_{2,3}^{\text{nosurf}}$, in terms of velocity, $\hat{v}_2^{\text{nosurf}}$. But now that the equation is written in the horizontal slowness domain with the help of Parseval's theorem, we notice that this operation can alternatively be applied to the surface wavefield, \hat{v}_2^{surf} , but with the Fourier transform applied to the shot positions, instead of the receiver positions. We then transform the equation back to the space-Laplace domain by applying Parseval's theorem again. Then, we arrive at the formulation of eq. (3.15) in the intermezzo about the Neumann series expansion. In discrete notation, this equation becomes:

$$\frac{\mu}{\hat{f}_2(s)} \mathcal{F}_S^{-1} \left\{ \mathcal{F}_S \left\{ \hat{\mathbf{V}}_2^{\text{surf}} \right\} \cdot \mathbf{\Gamma}_s \right\} \cdot \hat{\mathbf{V}}_2^{\text{nosurf}} \Delta x_1 = \hat{\mathbf{V}}_2^{\text{surf}} - \hat{\mathbf{V}}_2^{\text{nosurf}}. \quad (3.26)$$

Here, $\mathbf{\Gamma}_s$ is the discrete counterpart of γ_s . Since it is a function of α_1^S only, it has the shape of a diagonal matrix. We rewrite the equation as:

$$\hat{\mathbf{V}}_2^{\text{nosurf}} = \left[\frac{\mu \Delta x_1}{\hat{f}_2(s)} \mathcal{F}_S^{-1} \left\{ \mathcal{F}_S \left\{ \hat{\mathbf{V}}_2^{\text{surf}} \right\} \cdot \mathbf{\Gamma}_s \right\} + \mathbf{I} \right]^{-1} \cdot \hat{\mathbf{V}}_2^{\text{surf}}. \quad (3.27)$$

In this equation, \mathbf{I} is the unity matrix. This equation can be solved with a matrix inversion, for example. Notice that in the integral equation, eq. (3.15),

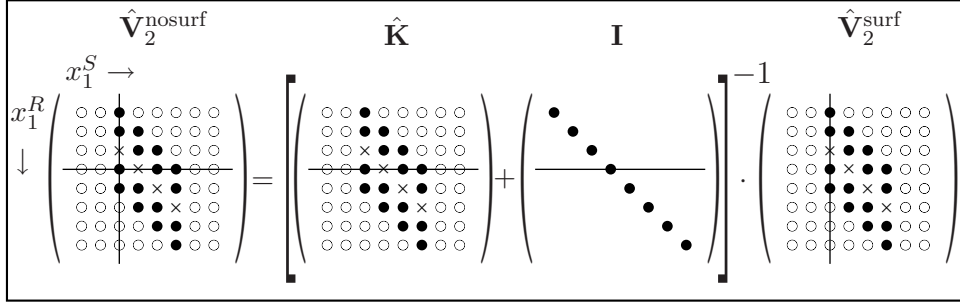


Figure 3.6: Procedure for solving a set of linear equations in the space-Laplace domain to obtain one Love-wave-free trace (denoted by the crossing of the lines on the left-hand side). A circle represents a padded zero, a disc a receiver and a cross a source position. The lines on the right hand side indicate the source and receiver positions involved in the numerical procedure.

the integration variable is the source coordinate in the kernel and the receiver coordinate in the surface wavefield. This implies that the source and receiver sampling must be equal in order to solve the matrix equation, eq. (3.27). Figure 3.6 shows the layout of the matrices when the data is *split spread* (when there are as many receivers with negative offset in a gather as there are with positive offset), for a fixed Laplace parameter s . In this picture, $\hat{\mathbf{K}}$ denotes the discrete counterpart of the kernel described in eq. (3.16).

3.6 Numerical tests and results

This section tests the Love wave removal method described in the previous sections on several synthetic datasets. The datasets are obtained with the use of finite difference modeling, as developed by Falk [1998]. Although the structural model differs in each dataset, the material parameters are the same

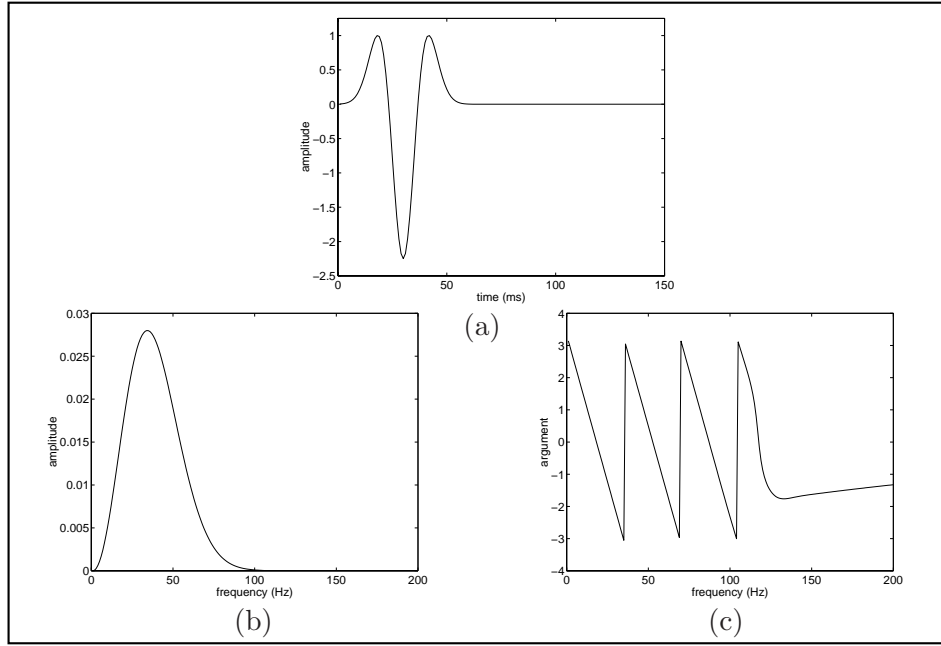


Figure 3.7: Source wavelet $f_2(t)$, (a) in the time domain, (b) its amplitude spectrum, (c) its phase spectrum.

for all. First, there is a thin, Love wave generating layer with a shear wave velocity of $c_s = 200$ m/s, then a thicker layer, which generates a normal reflection, with a shear wave velocity of $c_s = 300$ m/s, and finally the lower half-space, with a shear wave velocity of $c_s = 350$ m/s. The mass density is the same for all layers: $\rho = 2000$ kg/m³. Shot and receiver spacing is 0.8 m. The sampling interval in time is 0.001 s. For the source function, we use a Ricker-wavelet (2nd derivative of the Gaussian bell-curve), with a peak frequency of 33.3333 Hz, and which is shifted in time to make it (almost) causal. This wavelet is shown in Figure 3.7. The data are tapered with a spatial cosine taper to reduce edge effects that are caused by spatial windowing, and only the non-tapered parts of the data are shown. For the implementation of eq. (3.27) and eq. (3.25), we used a complex Laplace parameter $s = \varepsilon + j\omega$, where ω is the angular frequency, and an independent value of $\varepsilon = 4$ is used.

■ 3.6.1 A horizontally layered medium

For the first example, we use a horizontally layered medium. The first layer has a thickness of 1.2 m, the second layer has a thickness of 22.0 m. Figure 3.8 shows a graphical representation of this medium. Because the medium is horizontally layered, we modeled only one shot record. Figure 3.9a shows a shot record from this configuration. The problem is immediately visible. Love waves are the most dominant events in this figure. They are clearly



Figure 3.8: Configuration of a horizontally layered medium.

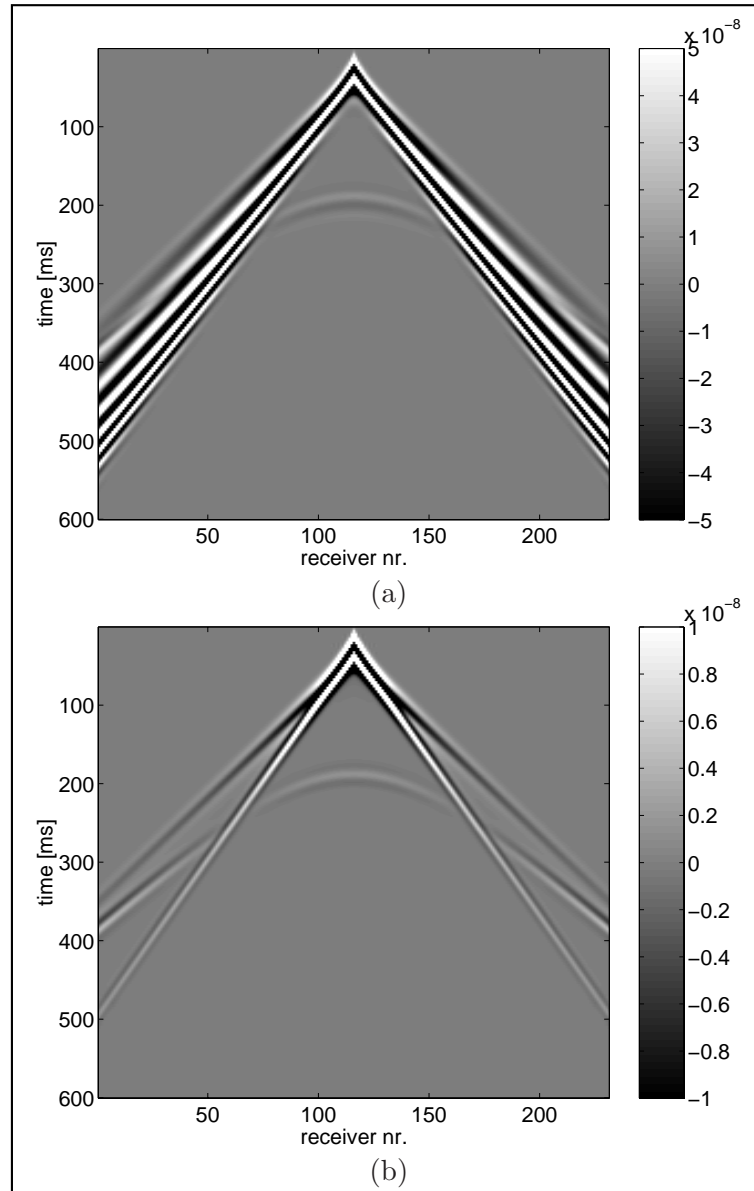


Figure 3.9: (a) Shot record including Love waves, in a horizontally layered medium, (b) after application of Love wave removal method (eq. (3.25)).

dispersive. The reflection from the deeper layer can be seen as a hyperbolic event at small offsets. For larger offsets, the Love waves obscure the reflection.

Figure 3.9b shows the shot record after the application of the removal method. Since the medium is horizontally layered, we used eq. (3.25). All the Love waves have been removed. The events that remain in this record, are the direct (incident) SH-wave, which interferes destructively with the reflection of the boundary of the first layer, and the refraction at this layer. More of the reflection of the deeper layer has become visible, and its amplitude ratio with respect to the other remaining events in this record is higher than in Figure 3.9a.

■ 3.6.2 A medium with an interface with a jump

As a next example, the removal method is tested on data from a medium with an interface with a jump. This medium is one of the most simple configurations that is not horizontally layered. Figure 3.10 shows a graphical representation of this medium. The depth of the small Love-wave generating layer was 0.8 m on the left side of the jump, and 2.8 m on the right side of the jump. The boundary of the deeper layer is located at a depth of 22.0 m. We modeled 251 shots, with 241 receivers each, in a split spread configuration. Figure 3.11a shows the data from shot number 126, the shot in the middle of the dataset. The source of this shot is located exactly above the jump in the

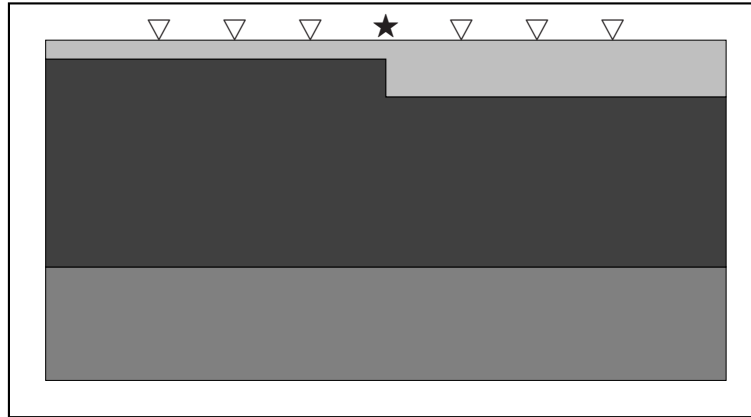


Figure 3.10: Configuration of a medium with an interface with a jump.

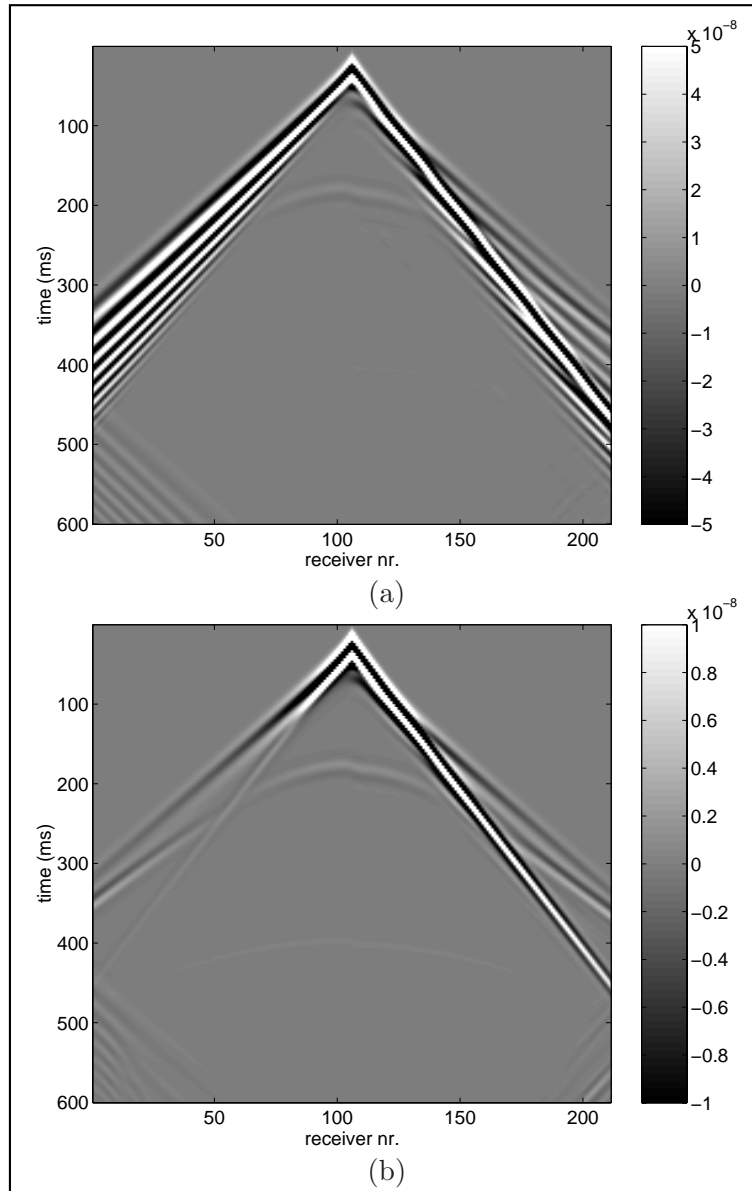


Figure 3.11: (a) Shot record including Love waves, in a medium with an interface with a jump, (b) after application of Love wave removal method (eq. (3.27)).

interface. The Love waves on the left side of the source differ from the Love waves on the right side of the source, which is to be expected. The effect of the jump is also visible in the reflection from the deeper layer.

Figure 3.11b shows the same shot record after the application of the removal method. Since the medium is no longer horizontally layered, eq. (3.27) must be used. Also here, the Love waves have been completely removed. We are left again with the direct (incident) wave, and the reflection and refraction of the small layer. This time, the incident wave and the reflection interfere even more destructively than in the previous example on the left side of the source, in such a way that the resulting wave is hardly visible. But the interference is less destructive on the right side of the source.

■ 3.6.3 A medium with a complex interface

The real test of the Love wave removal method comes with the next example. The medium used for this example has an interface that incorporates several jumps. Figure 3.12 shows a graphical representation of this medium. The thin Love-wave generating interface makes twelve of these jumps, evenly distributed over the model, which is 480 m wide, i.e. there is a jump every 40 m. The depth of this small layer varies from 0.8 m to 2.4 m. The depth of the reflection generating layer is 22.0 m. Again, we modeled 251 shots with 241 receivers each. Figure 3.13a shows the data from a shot in the middle

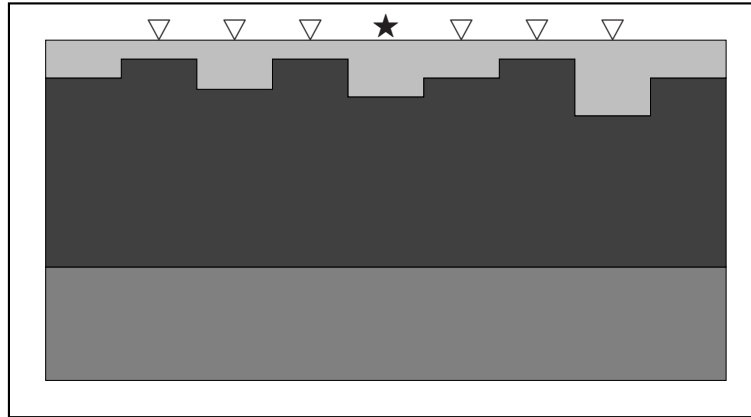


Figure 3.12: Configuration of a medium with a complex interface.

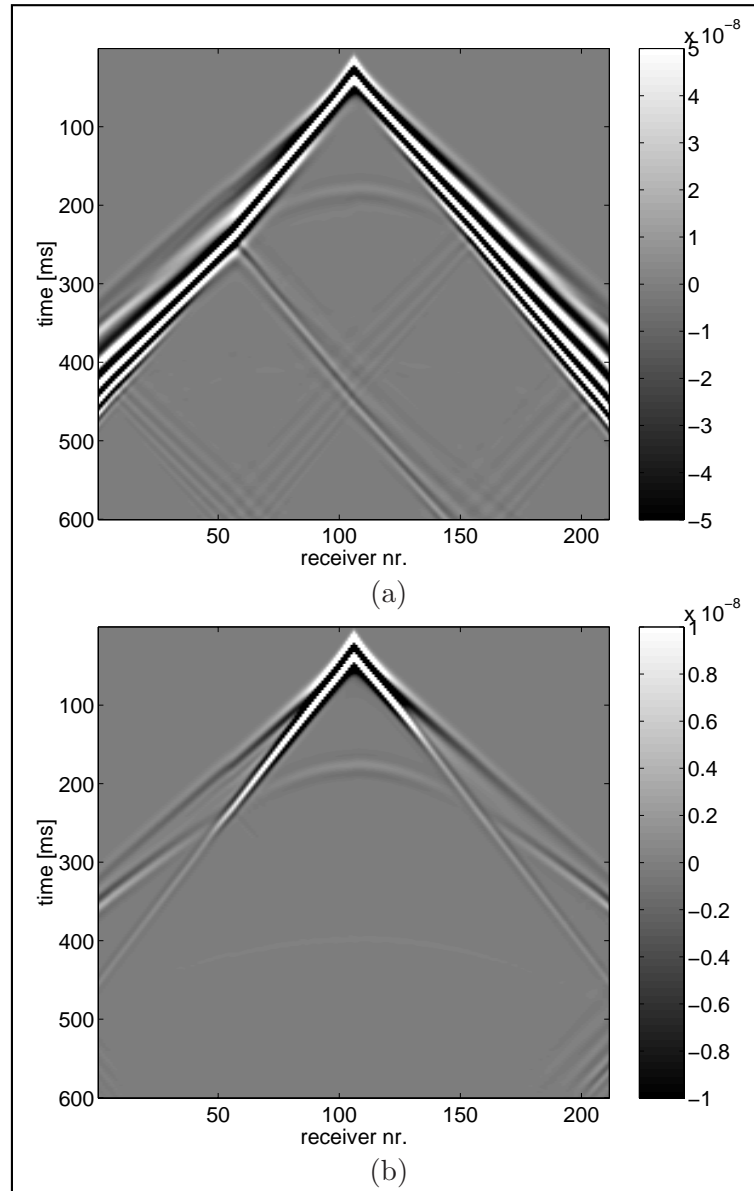


Figure 3.13: (a) Shot record including Love waves, in a medium with a complex interface, (b) after application of Love wave removal method (eq. (3.27)).

of the dataset. Love waves are again the dominant feature in these data. But together with the Love waves, other noise is introduced in the form of scattered Love waves, which are the result of the wave-front “hitting” a jump in the medium.

Figure 3.13b shows the same shot record after the application of the removal method. We have to use eq. (3.27) again. As expected, the Love waves are removed again. But also the scattered Love waves have been removed. In the absence of a (stress-free) surface, the scattered waves are no longer confined within the small layer, but radiate freely to the half-space above the receivers. Therefore their contribution in the data is drastically reduced.

■ 3.6.4 A medium with scatterers

After the result of the previous section, where scattered Love waves were removed by the method, we wondered if the method could also remove the effect of scatterers in the shallow subsurface. So for the final test in this thesis, we made a horizontally layered medium, like in the first example, but buried some scatterers in the thin Love wave generating layer. Figure 3.14 shows a graphical representation of this medium. The depth of the thin layer is 2.0 m. In this layer we place 4 scatterers at a depth of 1.6 m. These scatterers have a shear wave velocity much higher than the surrounding medium, namely

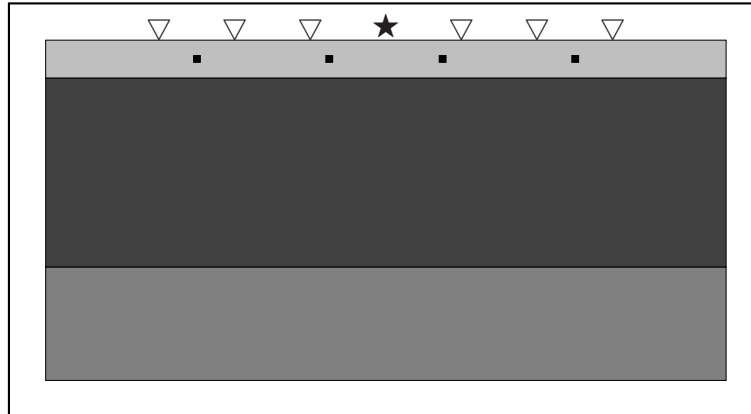


Figure 3.14: Configuration of a medium with scatterers.

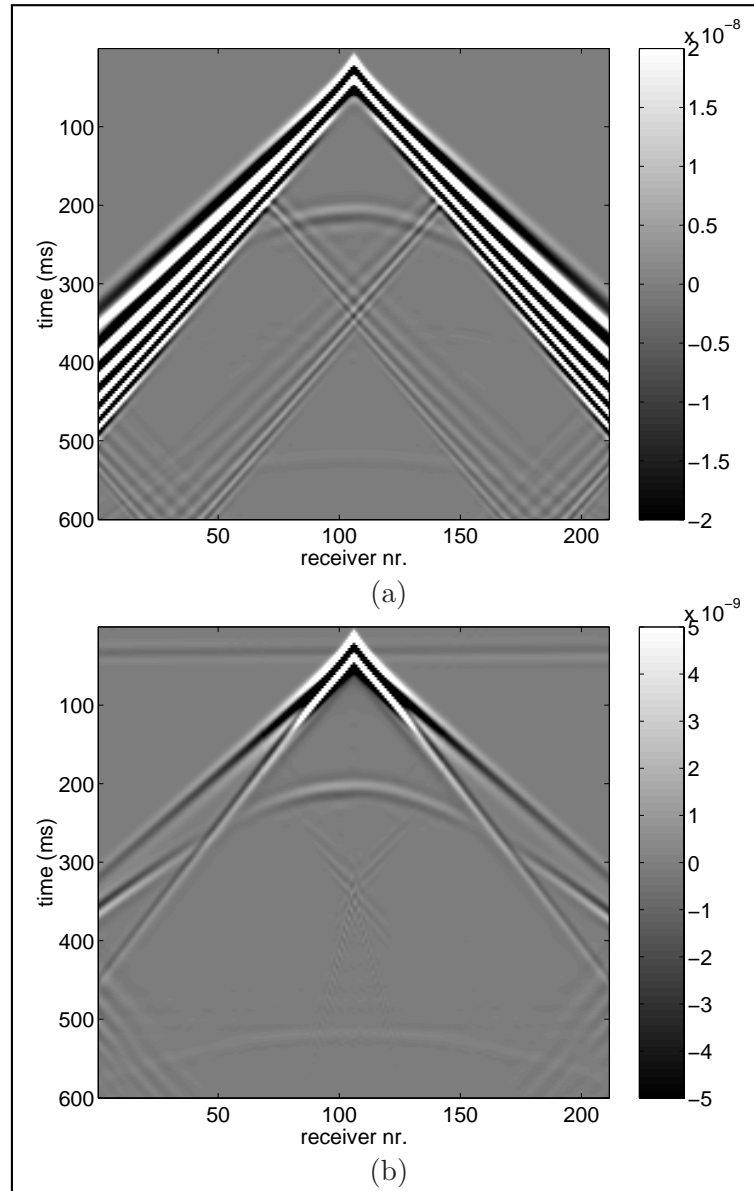


Figure 3.15: (a) Shot record including Love waves, in a medium with scatterers, (b) after application of Love wave removal method (eq. (3.27)).

800 m/s. The scatterers are 80 m apart from each other. Figure 3.15a shows the shot record at the central source position of the dataset. The source is located exactly between two scatterers, and the effect of them is obvious. In addition to the normal Love waves, we also have scattered Love waves.

Figure 3.15b shows the same shot record after the application of the removal method. The presence of scatterers makes this medium no longer horizontally layered, and therefore we must use eq. (3.27) again. As expected, both the Love waves and their scattering are removed. The little noise that remains is most likely the effect of small inaccuracies in the finite-difference method. For example, it cannot deal with sources and receivers located exactly on the surface, but places them one grid-space underneath it instead. This places the sources and receivers even more close to the scatterers than to the boundary of the example in the previous section.

Sensitivity of the Love-wave removal method

In the previous chapter, we developed a method to remove Love waves from seismic SH-wave data. The method performed very well on synthetic data examples. It was even capable of not only removing direct Love waves, but also their scattering. However, with synthetic data, the forward model is known exactly. This is of course not the case with field data. Therefore, in this chapter, we will examine the strengths and weaknesses of the removal method. In other words, we will test under what conditions the method will still perform well, and when it will not. The actual application of the method on a field dataset is discussed in Appendix C.

Two distinctions can be made in this testing. First, the estimation of the input parameters can be wrong. The effects of this are studied in the first section. Second, the input data can be distorted. This can be the result of stochastic noise, or because the subsurface incorporates effects that are not described by the elastodynamic theory. These effects are studied in the second section. Finally, as a third example, we study the sensitivity of the method to the source wavelet. The source wavelet is also an input parameter to the Love-wave removal method, or more precise, it is an input vector. This is the reason that we devote a separate, third section to the effects of a wrong estimation of the source wavelet. We will find that the Love-wave removal method is relatively most sensitive to distortions in the source wavelet.

Throughout this chapter, we use data from a horizontally layered medium. This way, eq. (3.25) can be used, which drastically reduces the amount of calculations. This configuration is described in Section 3.6.1.

4.1 Effect of an erroneous estimation of input parameters

The Love-wave removal equations, eq. (3.25) and eq. (3.27), require two scalar input parameters. They are: the shear wave velocity c_s of the upper layer, and its shear modulus μ . Since the shear modulus can be written as $\mu = \rho c_s^2$, the mass density can also be used as an input parameter. This section explores the effects when these parameters are wrongly estimated, i.e. when they are chosen too high or too low.

■ 4.1.1 Effect of an erroneous estimation of the velocity

Figure 4.1 shows the result of the Love-wave removal method, when the velocity is estimated two times too low, i.e. it is chosen as 100 m/s instead

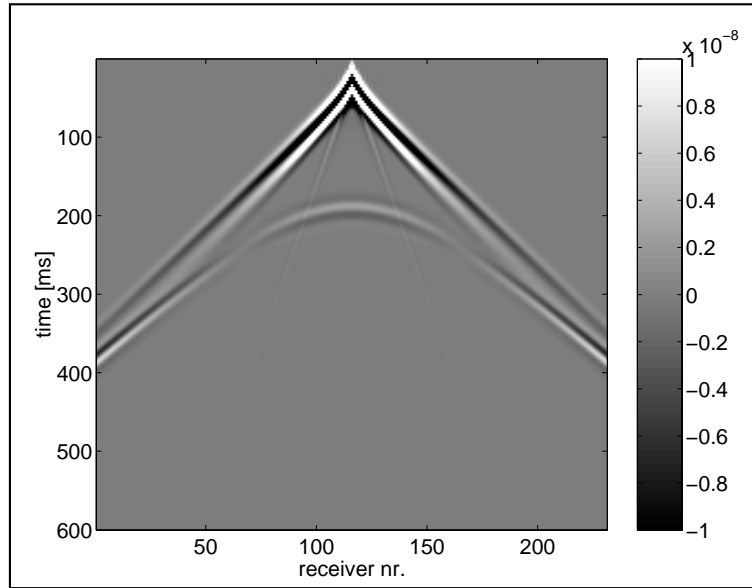


Figure 4.1: Result of removal method, when the velocity is underestimated.

of 200 m/s. The Love waves are still removed to the same extent as the example in Section 3.6.1. The only aberration is that the direct wave (which originally had a velocity of 200 m/s) is replaced by one with a velocity of 100 m/s. However, an effect like this was to be expected. Similar results are obtained when the shear-wave velocity is overestimated by a factor of two, i.e. 400 m/s (instead of 200 m/s).

Fortunately, a very estimation of the shear-wave velocity can usually be obtained easily from the data. Deviations by a factor of two are certainly not an issue. But even then, the Love-wave removal method will still produce very good results.

■ 4.1.2 Effect of an erroneous estimation of the mass density

Figure 4.2 shows the result of the Love-wave removal method, when the mass density of the top layer is severely underestimated. It is chosen as 750 kg/m^3 , instead of 2000 kg/m^3 . The result is still satisfactory. Although the Love waves are not completely removed, they are suppressed for the greater part.

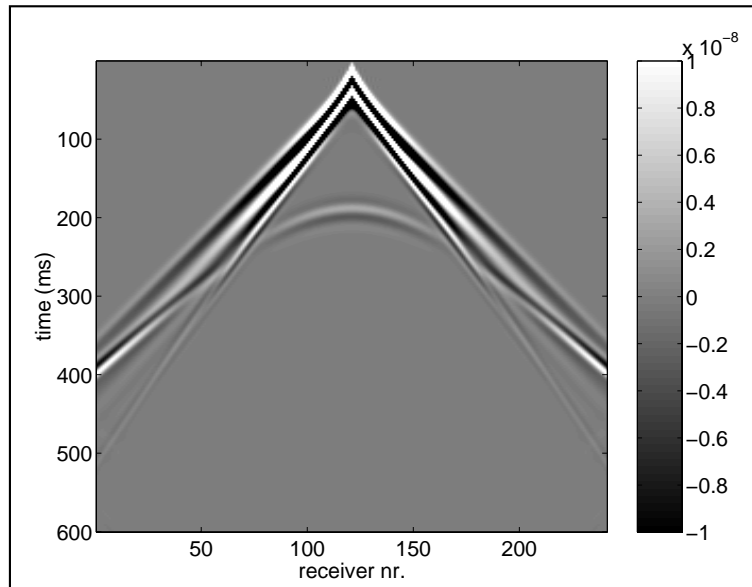


Figure 4.2: Result of removal method, when the mass density is underestimated

When the mass density is chosen too large, the Love-wave removal method will still provide good results. However, the total energy of the resulting data (see Appendix D for a definition of energy in data) decreases as the mass density is chosen larger. The cause of this effect becomes clear when we examine eq. (3.27). When, in this equation, ρ (or equivalently: μ) is chosen infinitely large, the result will go to: $\hat{\mathbf{V}}_2^{\text{nosurf}} \rightarrow \mathbf{0}$.

So also for the mass density (or equivalently, the shear modulus), it is concluded that the Love-wave removal method will provide good results as long as this parameter is chosen correctly within an order of magnitude. Indeed, this parameter can be used as a “fudge factor”. When the mass density is unknown, we start the method with a low value for it, and then perform the method iteratively, until the Love waves are completely removed.

4.2 Effect of distorted input data

In addition to unknown input parameters, the data itself can be distorted in ways that are not described by the theory. Some of these distortions are discussed here. One example is the addition of random, stochastic noise, another example is the effect of anelastic attenuation.

■ 4.2.1 Effect of random noise

The distortion of data unfortunately does not stay limited to shot generated noise. Random, stochastic noise is also present in field data. The only assumption that will be made about this kind of noise, is that it is additive. Figure 4.3a shows the data with random noise added to it. The noise level is as high as the amplitude of the reflection of the deeper layer.

Figure 4.3b shows the result of the removal procedure on this data. The presence of noise in the data did not seem to influence the result. The Love waves are still removed, and the reflection, previously buried underneath the noise, now becomes visible, especially for larger offsets. One remark is that the noise increases for larger times. This is probably because of the exponential taper used for the complex Laplace parameter. Another remark is that the noise appears to be more coherent after the application of the method. That could be explained as the method performing its operations on the noise part of the data.

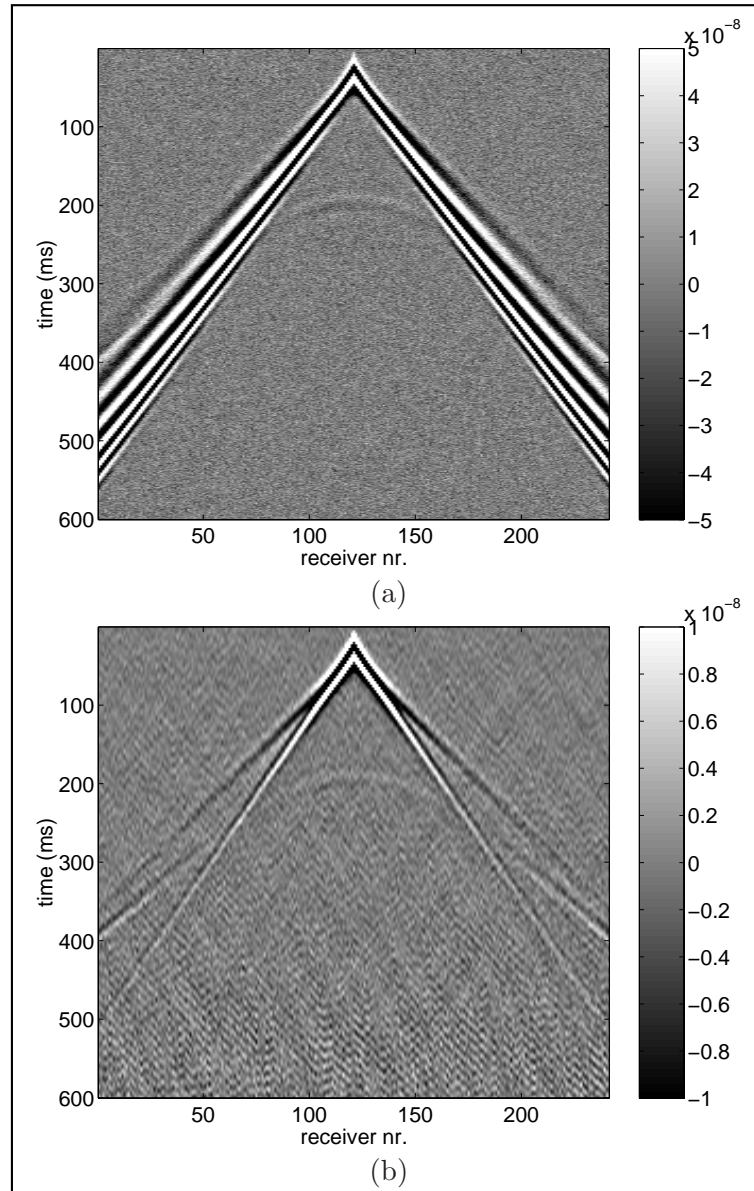


Figure 4.3: (a) Shot record of data with added random noise, (b) after application of the removal method (eq. (3.25)).

■ 4.2.2 Effect of anelastic attenuation

A wave described by the elastodynamic wave theory will continue to propagate through a medium indefinitely. The wave will attenuate spatially, but the total energy of the particle motion in the medium will be preserved. Observations in the field show this idealization to be inaccurate. A wave field will attenuate through a number of processes, which we will describe as being anelastic. Aki and Richards [1980] give a description of the effects of anelastic attenuation, via a *quality factor* Q . A high value of Q means a high “quality” of the medium, that acts mainly elastic, while a low value means a low “quality” of the medium, with much attenuation. In the shallow region, which is the focus of this thesis, where the soil is soft and unconsolidated, the quality factor can be as low as 5.

Figure 4.4a shows the data on which anelastic attenuation is introduced, in the form of an exponential taper applied to the data. A quality factor of 10 is used. Figure 4.4b shows the data after application of the removal method. The method still removes the Love waves. It does introduce a direct wave which is not attenuated into the data. However, in view of Section 4.1.1, an effect like this was to be expected.

The method can be extended by incorporating the effects of anelastic attenuation. Another way to describe the effect of losses in an elastic medium is to take complex values for the material parameters (de Hoop and Stam [1988]). It is likely that the method can be improved by taking such a complex value for the shear modulus μ and shear-wave velocity c_s in eq. (3.14) or eq. (3.27). A further discussion is beyond the scope of this thesis.

4.3 Effect of an erroneous estimation of the source wavelet

As a final example, we test the sensitivity of the method to errors in the source wavelet. As can be seen in eq. (3.27) or eq. (3.25), the method performs a deconvolution step, i.e. the data are divided by the source wavelet. This could be a sensitive procedure. The problem can actually be divided into two parts: The effect of deviations in the amplitude of the source wavelet, and the effect of deviations in the phase of the source wavelet. When we look at eq. (3.27), we see that it contains the term $\mu/\hat{f}_2(s)$. This implies that a deviation in the amplitude of the wavelet is equivalent to a deviation in the shear modulus (or also: mass density). This has been explored in Section 4.1.2, and we concluded that our method was not very sensitive to that. Therefore, this section will focus on the effect of deviations in the phase

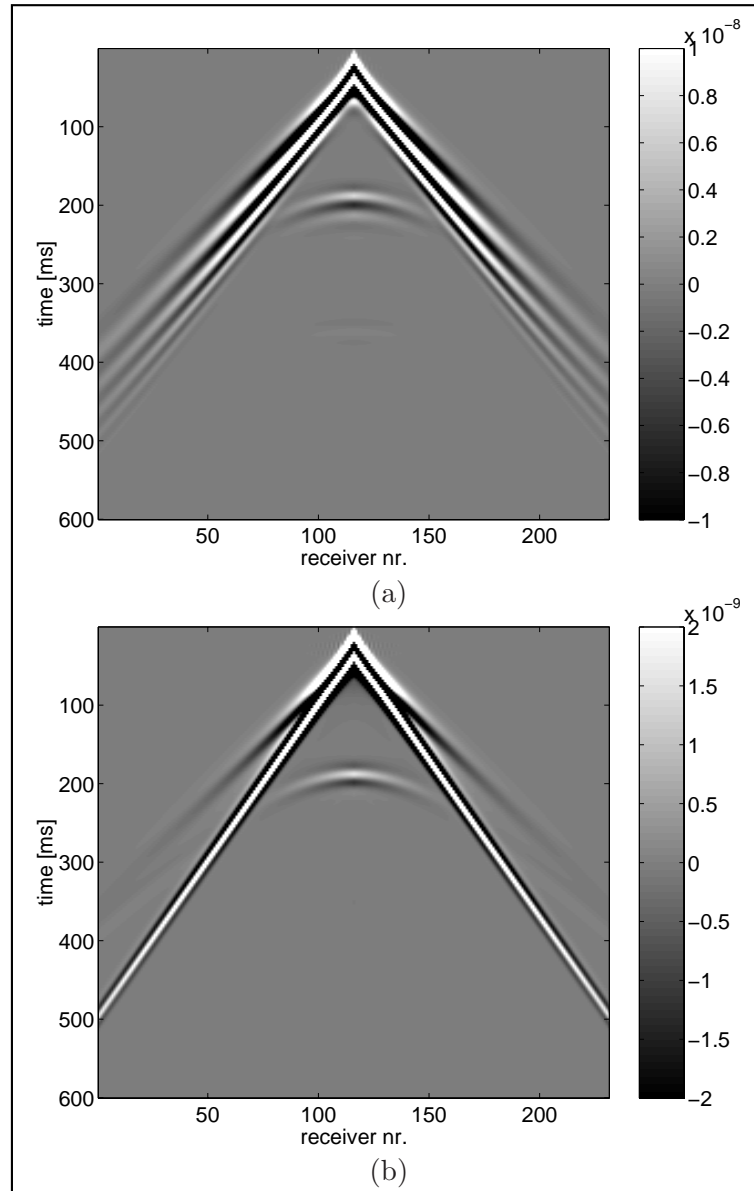


Figure 4.4: (a) Shot record with anelastic attenuation introduced in the data, (b) after application of removal method (eq. (3.25)).

of the wavelet.

As explained in Section 3.6, for the forward modeling, we used a shifted version of the Ricker wavelet, which was then almost causal. Next, we applied a phase shift of 60 degrees to this wavelet, and used this resulting wavelet in the removal procedure. Figure 4.5 shows these two wavelets, and it can be seen that the shape of the wavelet has been changed significantly.

Figure 4.6 shows the result of the removal procedure where the phase-shifted wavelet is used. The Love waves are not completely suppressed anymore, and some noise is added to the data. When the phase shift becomes bigger, more noise is added faster, and the Love waves are also suppressed much worse.

The distortions in the the phase of the wavelet are the only example of errors we found that introduces noise in the data. Therefore, if the source wavelet is unknown, then this implies that it can be estimated from the data with a wavelet estimation procedure based on energy minimization. An attempt to develop such an estimation procedure was tried by the author, but was not successful. This attempt is described in Appendix D.

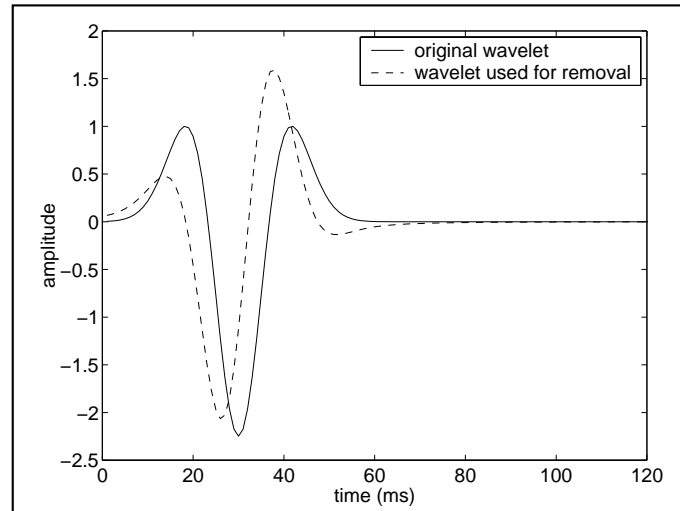


Figure 4.5: The source signature wavelets, the solid line is the one used in the forward modeling, the dashed line is the one used in the removal method.

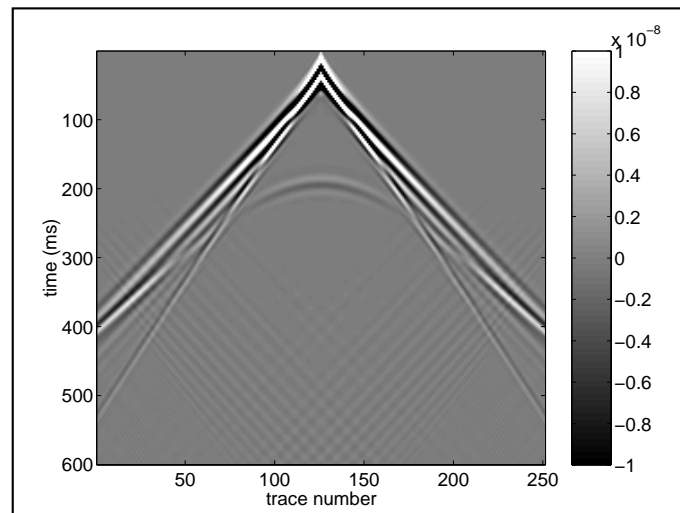


Figure 4.6: Result of removal method, when a shifted wavelet is used.

Towards removal of surface effects from coupled P- and SV-wave systems

Up to this point, this thesis focussed on the the removal of Love waves from seismic SH-wave data. In this chapter, we will explore the possibilities of removing surface effects, in particular Rayleigh waves, from seismic P- and SV-wave data in isotropic media. Since P- and SV-waves are coupled in elastic media, the resulting equations will be coupled as well.

The starting point of our analysis is similar to Chapter 3. We define two different elastodynamic states for use in the Betti-Rayleigh reciprocity integral. One state is the actual state which has a stress-free surface, the other state is the desired state, which lacks this surface. The difference with Chapter 3 lies in the definition of the source-terms. In the P- and SV-wave case, these sources will point in the x_1 and x_3 directions, instead of in the x_2 direction. The resulting wavefield is then measured with receivers measuring the x_1 and x_3 components of the particle velocity.

Due to the length and complexity of the equations, we consider only horizontally layered media, so that we can follow the same procedure as in Section 3.4. This will simplify the expressions. The resulting expression

is a set of four equations with eight unknowns. Obviously, this is unsolvable. However, with one more simplification (we assume that the medium is a homogeneous halfspace), the number of unknowns reduces to four. We illustrate this result with an example in which we will remove the Rayleigh wave from finite difference data. As a final note, we expand the theory in such a way that it should be able to deal with the original and less trivial case of removing surface effects from horizontally layered media. No results have been obtained here yet, however.

Much of this chapter is the result of the M.Sc.-project performed by Lenders [2002].

5.1 Reciprocity for coupled P- and SV-wave systems

This chapter only considers coupled P- and SV-wave systems, without SH-waves. Therefore, some terms in the Betti-Rayleigh reciprocity theorem, eq. (2.38), drop. Specifically, we will not use sources of force in the crossline (x_2) direction and assume x_2 -invariant media. As a consequence, the particle velocity will not have a crossline component in the (x_1, x_3) -plane. We will also not use any sources of deformation rate, and we will define the two states in such a way, that the material parameters in the domain of integration are the same for both states. Lastly, we use line sources again. With these assumptions, the Betti-Rayleigh integral becomes:

$$\oint_{\mathbf{x} \in \partial \mathbb{V}} (\hat{\tau}_{i,j}^A \hat{v}_i^B - \hat{\tau}_{i,j}^B \hat{v}_i^A) n_j d\mathbf{x} = \int_{\mathbf{x} \in \mathbb{V}} [\hat{f}_i^B \hat{v}_i^A - \hat{f}_i^A \hat{v}_i^B] d^2\mathbf{x}, \quad (5.1)$$

where the subscripts i and j take the values 1 and 3 only.

5.2 Description of the reciprocity states

Here, we again describe the two states for the reciprocity theorem. State A , the state with a stress-free surface, will have the superscript *surf*, whereas state B , without such a surface, will have the superscript *nosurf*.

■ 5.2.1 The actual state - with a stress-free surface

In the actual configuration, it is assumed that there is a homogeneous and isotropic layer on top of further arbitrary earth layers. At $x_3 = 0$, the top layer is bounded by a stress-free surface, i.e. the boundary condition of eq. (2.15) is imposed. The material parameters of the top layer are denoted

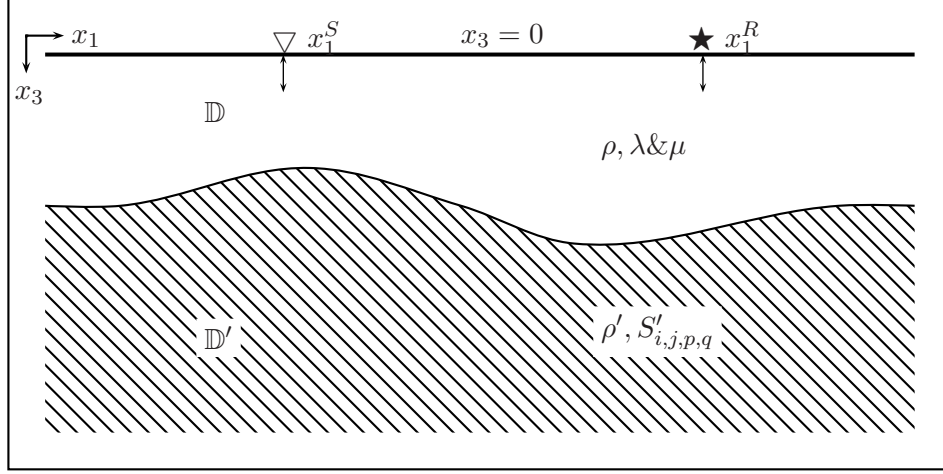


Figure 5.1: The actual state for the reciprocity theorem. As an example, the source and receiver are pointing in the x_3 direction.

with ρ and $\lambda \& \mu$. The material parameters of the further earth layers are denoted with ρ' and $S'_{i,j,p,q}$. Figure 5.1 shows a graphical representation of this configuration.

The source and receiver are placed on the surface $x_3 = 0$. The receiver is placed at x_3^S , and it is a multi-component receiver, capable of measuring both particle velocity components v_1 and v_3 . The source is introduced as a boundary condition in the stress field: The surface $x_3 = 0$ is stress-free, except at $x_1 = x_1^R$, where a traction source is introduced. Therefore, for the surface-state stress field, we can write:

$$\hat{\tau}_{i,3;m}^{\text{surf}}(x_1, x_3 = 0 | x_1^R, x_3^R = 0, s) = -\hat{t}^{\text{surf},m}(s) \delta_{i,m} \delta(x_1 - x_1^R). \quad (5.2)$$

Note that here, we did use the notation introduced in Section 2.6. The source is pointing specifically in the x_m -direction (where m can only take the values 1 or 3).

■ 5.2.2 The desired state - without a surface

The desired configuration doesn't have a stress-free surface at $x_3 = 0$. Instead, the material parameters of the top layer extend to $x_3 \rightarrow -\infty$. This causes the stress and particle velocity field to be continuous on the plane

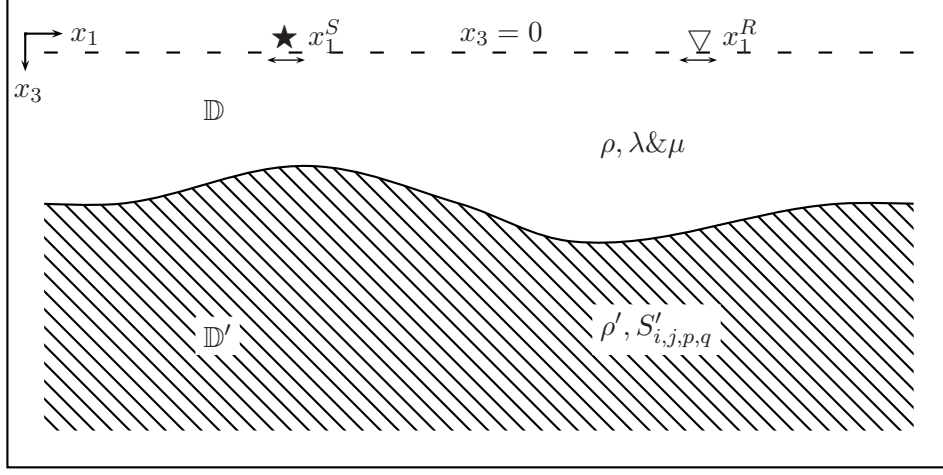


Figure 5.2: The desired state for the reciprocity theorem. As an example, the source and receiver are pointing in the x_1 direction.

$x_3 = 0$. A graphical representation of this configuration is shown in Figure 5.2.

Following the known procedure, we place sources and receivers on the plane $x_3 = 0$. A multi-component receiver is placed on the position x_1^R . It is capable of measuring both the x_1 - and x_3 -component of the particle velocity. We place a source of force density on the position x_1^S . It is defined as:

$$\hat{f}_i^{\text{nosurf}}(x_1, x_3 = 0 | x_1^S, x_3^S = 0, s) = \hat{f}^{\text{nosurf},n}(s) \delta_{i,n} \delta(x_1 - x_1^S) \delta(x_3). \quad (5.3)$$

Note that this source is pointing specifically in the x_n direction, where n can take the value 1 or 3.

5.3 Application of the reciprocity theorem

The domain of integration is the lower halfspace, $\{\mathbb{V} = \mathbb{D} \cup \mathbb{D}' \in \mathbb{R}^2 | -\infty < x_1 < \infty, 0 \leq x_3 < \infty\}$. The states we discussed in the previous section are summarized in Table 5.1. These states are now substituted in eq. (5.1). This

Table 5.1: States for the reciprocity theorem, used for the removal of surface effects from P- and SV-wave systems. \mathbf{x}^S and \mathbf{x}^R are located on the surface $x_3 = 0$.

	State A (surface state)	State B (no-surface state)
Field state	$\{\hat{\tau}_{i,j;m}^{\text{surf}}, \hat{v}_{i;m}^{\text{surf}}\}(\mathbf{x} \mathbf{x}^R, s)$	$\{\hat{\tau}_{i,j;n}^{\text{nosurf}}, \hat{v}_{i;n}^{\text{nosurf}}\}(\mathbf{x} \mathbf{x}^S, s)$
Material state	$\{\rho, \lambda \& \mu\}$ in \mathbb{D} $\{\rho', S'_{i,j,p,q}\}$ in \mathbb{D}'	$\{\rho, \lambda \& \mu\}$ in \mathbb{D} $\{\rho', S'_{i,j,p,q}\}$ in \mathbb{D}'
Source state	$\{0, 0\}$	$\{0, \hat{f}^{\text{nosurf},n}(s)\delta_{i,n} \times \delta(x_1 - x_1^S)\delta(x_3)\}$
Surface state	Stress-free except at $x_1 = x_1^R$: $\hat{\tau}_{i,3;m}^{\text{surf}} = -\hat{t}^{\text{surf},m}(s)\delta_{i,m} \times \delta(x_1 - x_1^R)$	Continuous velocity and traction
Domain $\mathbb{V} = \mathbb{D} \cup \mathbb{D}'$		

yields:

$$\begin{aligned}
\int_{x_1 \in \mathbb{R}} \hat{\tau}_{k,3;n}^{\text{nosurf}}(x_1, 0|x_1^S, 0, s) \hat{v}_{k;m}^{\text{surf}}(x_1, 0|x_1^R, 0, s) dx_1 = \\
+ \frac{1}{2} \hat{f}^{\text{nosurf},n}(s) \hat{v}_{n;m}^{\text{surf}}(x_1^S, 0|x_1^R, 0, s) - \hat{t}^{\text{surf},m}(s) \hat{v}_{m;n}^{\text{nosurf}}(x_1^R, 0|x_1^S, 0, s).
\end{aligned} \tag{5.4}$$

The factor $\frac{1}{2}$ in the first term on the right hand side is the result of the integration over a delta function which was located on the edge of the domain of integration (the surface $x_3 = 0$).

Our aim is to solve the no-surface wavefield $\hat{v}_{m;n}^{\text{nosurf}}$ from the measured wavefield $\hat{v}_{n;m}^{\text{surf}}$. The remaining unknown factor in eq. (5.4) is the desired stress-field, $\hat{\tau}_{k,3;n}^{\text{nosurf}}$. This term has to be rewritten with the help of eq. (2.21)

and eq. (2.19). After applying physical reciprocity (see Section 2.6) on the terms $\hat{v}_{k;m}^{\text{surf}}$, we obtain:

$$\begin{aligned} \int_{x_1 \in \mathbb{R}} \left(\frac{C_{k,3,p,q}}{s} \partial_p \hat{v}_{q;n}^{\text{nosurf}}(x_1, 0|x_1^S, 0, s) \right) \hat{v}_{m;k}^{\text{surf}}(x_1^R, 0|x_1, 0, s) dx_1 = \\ \frac{1}{2} \hat{f}^{\text{nosurf},n}(s) \hat{v}_{m;n}^{\text{surf}}(x_1^R, 0|x_1^S, 0, s) - \hat{t}^{\text{surf},m}(s) \hat{v}_{m;n}^{\text{nosurf}}(x_1^R, 0|x_1^S, 0, s). \end{aligned} \quad (5.5)$$

Since we assumed that the top layer is an isotropic layer, and by using eq. (2.10), we see that the stress terms become:

$$\hat{\tau}_{1,3;n}^{\text{nosurf}} = \frac{\mu}{s} \partial_1 \hat{v}_{3;n}^{\text{nosurf}} + \frac{\mu}{s} \partial_3 \hat{v}_{1;n}^{\text{nosurf}}, \quad (5.6)$$

and

$$\hat{\tau}_{3,3;n}^{\text{nosurf}} = \frac{\lambda}{s} \partial_1 \hat{v}_{1;n}^{\text{nosurf}} + \frac{\lambda + 2\mu}{s} \partial_3 \hat{v}_{3;n}^{\text{nosurf}}. \quad (5.7)$$

With this, eq. (5.5) becomes:

$$\begin{aligned} \int_{x_1 \in \mathbb{R}} \left(\frac{\mu}{s} \partial_1 \hat{v}_{3;n}^{\text{nosurf}}(x_1, 0|x_1^S, 0, s) + \frac{\mu}{s} \partial_3 \hat{v}_{1;n}^{\text{nosurf}}(x_1, 0|x_1^S, 0, s) \right) \cdot \\ \hat{v}_{m;1}^{\text{surf}}(x_1^R, 0|x_1, 0, s) dx_1 + \\ \int_{x_1 \in \mathbb{R}} \left(\frac{\lambda}{s} \partial_1 \hat{v}_{1;n}^{\text{nosurf}}(x_1, 0|x_1^S, 0, s) + \frac{\lambda + 2\mu}{s} \partial_3 \hat{v}_{3;n}^{\text{nosurf}}(x_1, 0|x_1^S, 0, s) \right) \cdot \\ \hat{v}_{m;3}^{\text{surf}}(x_1^R, 0|x_1, 0, s) dx_1 = \\ \frac{1}{2} \hat{f}^{\text{nosurf},n}(s) \hat{v}_{m;n}^{\text{surf}}(x_1^R, 0|x_1^S, 0, s) - \hat{t}^{\text{surf},m}(s) \hat{v}_{m;n}^{\text{nosurf}}(x_1^R, 0|x_1^S, 0, s). \end{aligned} \quad (5.8)$$

This equation becomes more convenient in the horizontal slowness domain, because in that domain we are able to substitute simple multiplications in the place of the partial derivatives. A partial derivative with respect to the x_1 coordinate (∂_1) in the space domain becomes a multiplication with $-js\alpha_1$ in the angular slowness domain. But the partial derivative with respect to the x_3 coordinate (∂_3) is more difficult. For this, we first have to know whether the derivative applies to an up-going or down-going field. And second, we have to know with what velocity the wavefield travels. In Section 3.3.1, we saw that when a reflected shear-wave field was differentiated to the x_3 coordinate, this differentiation became a multiplication with $s\gamma_s$ in the horizontal slowness domain. Analogously, a differentiation with respect

to the x_3 coordinate of a reflected P-wave field becomes a multiplication with $s\gamma_p$ in the horizontal slowness domain. γ_s is defined by eq. (3.8), and γ_p is given as:

$$\gamma_p = \sqrt{\frac{1}{c_p^2} + \alpha_1^2}, \quad \text{Re}(\gamma_p) > 0. \quad (5.9)$$

We see that in order to be able to perform the differentiation with respect to the x_3 coordinate, the no-surface wavefield has to be split into *three* parts: the incident field, the reflected P-wave field and the reflected SV-wave field:

$$\hat{v}_{i;n}^{\text{nosurf}} = \hat{v}_{i;n}^{\text{inc}} + \hat{v}_{i;n}^{\text{ref,P}} + \hat{v}_{i;n}^{\text{ref,SV}}. \quad (5.10)$$

In Appendix B.2 we see that the vertical derivative of the incident P- and SV-wave field is not equal to zero for all combinations of source and receiver directions, in contrast to the SH-wave case.

Using Parseval's theorem to transform the necessary quantities to the horizontal slowness domain, we obtain:

$$\begin{aligned} & \frac{1}{2\pi} \int_{s\alpha_1 \in \mathbb{R}} \left(\frac{\mu}{s} (-js\alpha_1) \tilde{v}_{3;n}^{\text{inc}} + \frac{\mu}{s} (-js\alpha_1) \tilde{v}_{3;n}^{\text{ref,P}} + \frac{\mu}{s} (-js\alpha_1) \tilde{v}_{3;n}^{\text{ref,SV}} \right. \\ & \quad \left. + \frac{\mu}{s} \partial_3 \tilde{v}_{1;n}^{\text{inc}} + \mu\gamma_p \tilde{v}_{1;n}^{\text{ref,P}} + \mu\gamma_s \tilde{v}_{1;n}^{\text{ref,SV}} \right) (js\alpha_1, 0|x_1^S, 0, s) \cdot \\ & \quad \tilde{v}_{m;1}^{\text{surf}}(x_1^R, 0|js\alpha_1, 0, s) \, ds\alpha_1 + \\ & \frac{1}{2\pi} \int_{s\alpha_1 \in \mathbb{R}} \left(\frac{\lambda}{s} (-js\alpha_1) \tilde{v}_{1;n}^{\text{inc}} + \frac{\lambda}{s} (-js\alpha_1) \tilde{v}_{1;n}^{\text{ref,P}} + \frac{\lambda}{s} (-js\alpha_1) \tilde{v}_{1;n}^{\text{ref,SV}} \right. \\ & \quad \left. + \frac{\lambda + 2\mu}{s} \partial_3 \tilde{v}_{3;n}^{\text{inc}} + (\lambda + 2\mu)\gamma_p \tilde{v}_{3;n}^{\text{ref,P}} + (\lambda + 2\mu)\gamma_s \tilde{v}_{3;n}^{\text{ref,SV}} \right) (js\alpha_1, 0|x_1^S, 0, s) \cdot \\ & \quad \tilde{v}_{m;3}^{\text{surf}}(x_1^R, 0|js\alpha_1, 0, s) \, ds\alpha_1 = \\ & \frac{1}{2} \hat{f}^{\text{nosurf},n}(s) \hat{v}_{m;n}^{\text{surf}}(x_1^R, 0|x_1^S, 0, s) - \hat{t}^{\text{surf},m}(s) \hat{v}_{m;n}^{\text{inc}}(x_1^R, 0|x_1^S, 0, s) \\ & \quad - \hat{t}^{\text{surf},m}(s) \hat{v}_{m;n}^{\text{ref,P}}(x_1^R, 0|x_1^S, 0, s) - \hat{t}^{\text{surf},m}(s) \hat{v}_{m;n}^{\text{ref,SV}}(x_1^R, 0|x_1^S, 0, s). \end{aligned} \quad (5.11)$$

At this point, we assume that the medium is horizontally layered. Then, we can follow the same line of reasoning as in Section 3.4. We perform a double Fourier transformation on eq. (5.11), with respect to the source coordinate and with respect to the receiver coordinate. All the wavefield quantities become diagonal kernels (see eq. (3.22)), and this eliminates the integrals. Since all the wavefield quantities now have the same coordinate

dependence (which is $(js\alpha_1, 0, s)$), we will drop that notation. We obtain:

$$\begin{aligned}
& \left(\frac{\mu}{s}(-js\alpha_1)\tilde{v}_{3;n}^{\text{inc}} + \frac{\mu}{s}(-js\alpha_1)\tilde{v}_{3;n}^{\text{ref,P}} + \frac{\mu}{s}(-js\alpha_1)\tilde{v}_{3;n}^{\text{ref,SV}} + \right. \\
& \quad \left. \frac{\mu}{s}\partial_3\tilde{v}_{1;n}^{\text{inc}} + \mu\gamma_p\tilde{v}_{1;n}^{\text{ref,P}} + \mu\gamma_s\tilde{v}_{1;n}^{\text{ref,SV}} \right) \cdot \tilde{v}_{m;1}^{\text{surf}} + \\
& \left(\frac{\lambda}{s}(-js\alpha_1)\tilde{v}_{1;n}^{\text{inc}} + \frac{\lambda}{s}(-js\alpha_1)\tilde{v}_{1;n}^{\text{ref,P}} + \frac{\lambda}{s}(-js\alpha_1)\tilde{v}_{1;n}^{\text{ref,SV}} + \right. \\
& \quad \left. \frac{\lambda + 2\mu}{s}\partial_3\tilde{v}_{3;n}^{\text{inc}} + (\lambda + 2\mu)\gamma_p\tilde{v}_{3;n}^{\text{ref,P}} + (\lambda + 2\mu)\gamma_s\tilde{v}_{3;n}^{\text{ref,SV}} \right) \cdot \tilde{v}_{m;3}^{\text{surf}} = \\
& \frac{1}{2}\hat{f}^{\text{nosurf},n}(s)\tilde{v}_{m;n}^{\text{surf}} - \hat{t}^{\text{surf},m}(s)\tilde{v}_{m;n}^{\text{inc}} - \hat{t}^{\text{surf},m}(s)\tilde{v}_{m;n}^{\text{ref,P}} - \hat{t}^{\text{surf},m}(s)\tilde{v}_{m;n}^{\text{ref,SV}}.
\end{aligned} \tag{5.12}$$

This is a set of four equations (both m and n can take the values 1 and 3) with eight unknowns. For with each combination of m and n , the unknown terms are split into a P-wave field ($\tilde{v}_{m;n}^{\text{ref,P}}$) and an SV-wave field ($\tilde{v}_{m;n}^{\text{ref,SV}}$). The incident field terms ($\tilde{v}_{m;n}^{\text{inc}}$) are derived in Appendix B.2. This problem is unsolvable in its current form. In the next section, we make one more simplification, i.e. we assume that the medium is a homogeneous halfspace. This will reduce the number of unknowns.

In Section 5.6, we will find auxiliary relations for the particle velocity. Together with those, the set of equations, eq. (5.12), should also be solvable for inhomogeneous (but horizontally layered) media. But no results have been obtained yet.

5.4 Removing Rayleigh waves from a homogeneous halfspace

In order to show the validity of the theory above, we make one more simplification. We assume that the medium consists of a homogeneous and isotropic halfspace only, bounded at $x_3 = 0$ by a stress-free surface. The description of seismic waves in this kind of configuration is classically known as *Lamb's problem* (Lamb [1904]).

It is obvious that in this configuration, no reflections will occur. Therefore, when we look at eq. (5.12), all the terms $\tilde{v}_{m;n}^{\text{ref,P}}$ and $\tilde{v}_{m;n}^{\text{ref,SV}}$ vanish, and for the sake of the argument, we assume that $\tilde{v}_{m;n}^{\text{inc}}$ are the unknown terms for which we want to solve. In Appendix B.2, we show that the following terms also vanish: $\tilde{v}_{3;1}^{\text{inc}}$, $\tilde{v}_{1;3}^{\text{inc}}$, $\partial_3\tilde{v}_{1;1}^{\text{inc}}$ and $\partial_3\tilde{v}_{3;3}^{\text{inc}}$. When we take all source wavelets equal, i.e. $\hat{f}^{\text{nosurf},n}(s) = \hat{t}^{\text{surf},m}(s) = \hat{f}(s)$, similar to Section 3.3, and divide by that wavelet, what remains are the following four equations:

$m = 1$ and $n = 1$:

$$\frac{2\lambda}{s\hat{f}(s)}(-js\alpha_1)\tilde{v}_{1;1}^{\text{inc}}\tilde{v}_{1;3}^{\text{surf}} + \frac{2(\lambda+2\mu)}{s\hat{f}(s)}(\partial_3\tilde{v}_{3;1}^{\text{inc}})\tilde{v}_{1;3}^{\text{surf}} + 2\tilde{v}_{1;1}^{\text{inc}} = \tilde{v}_{1;1}^{\text{surf}}, \quad (5.13)$$

$m = 3$ and $n = 1$:

$$\frac{2\lambda}{s\hat{f}(s)}(-js\alpha_1)\tilde{v}_{1;1}^{\text{inc}}\tilde{v}_{3;3}^{\text{surf}} + \frac{2(\lambda+2\mu)}{s\hat{f}(s)}(\partial_3\tilde{v}_{3;1}^{\text{inc}})\tilde{v}_{3;3}^{\text{surf}} = \tilde{v}_{3;1}^{\text{surf}}, \quad (5.14)$$

$m = 1$ and $n = 3$:

$$\frac{2\mu}{s\hat{f}(s)}(-js\alpha_1)\tilde{v}_{3;3}^{\text{inc}}\tilde{v}_{1;1}^{\text{surf}} + \frac{2\mu}{s\hat{f}(s)}(\partial_3\tilde{v}_{1;3}^{\text{inc}})\tilde{v}_{1;1}^{\text{surf}} = \tilde{v}_{1;3}^{\text{surf}}, \quad (5.15)$$

$m = 3$ and $n = 3$:

$$\frac{2\mu}{s\hat{f}(s)}(-js\alpha)\tilde{v}_{3;3}^{\text{inc}}\tilde{v}_{3;1}^{\text{surf}} + \frac{2\mu}{s\hat{f}(s)}(\partial_3\tilde{v}_{3;1}^{\text{inc}})\tilde{v}_{1;3}^{\text{surf}} + 2\tilde{v}_{3;3}^{\text{inc}} = \tilde{v}_{3;3}^{\text{surf}}. \quad (5.16)$$

This set of four equations has four unknowns ($\tilde{v}_{1;1}^{\text{inc}}$, $\tilde{v}_{3;3}^{\text{inc}}$, $\partial_3\tilde{v}_{3;1}^{\text{inc}}$ and $\partial_3\tilde{v}_{1;3}^{\text{inc}}$). We can arrange these equations into a matrix equation, which has the form:

$$\begin{pmatrix} A & B & 0 & 0 \\ C & D & 0 & 0 \\ 0 & 0 & E & F \\ 0 & 0 & G & H \end{pmatrix} \cdot \begin{pmatrix} \tilde{v}_{1;1}^{\text{inc}} \\ \partial_3\tilde{v}_{3;1}^{\text{inc}} \\ \partial_3\tilde{v}_{1;3}^{\text{inc}} \\ \tilde{v}_{3;3}^{\text{inc}} \end{pmatrix} = \begin{pmatrix} \tilde{v}_{1;1}^{\text{surf}} \\ \tilde{v}_{3;1}^{\text{surf}} \\ \tilde{v}_{1;3}^{\text{surf}} \\ \tilde{v}_{3;3}^{\text{surf}} \end{pmatrix}, \quad (5.17)$$

in which:

$$A = \frac{2\lambda(-js\alpha_1)}{s\hat{f}(s)}\tilde{v}_{1;3}^{\text{surf}} + 2, \quad (5.18)$$

$$B = \frac{2(\lambda+2\mu)}{s\hat{f}(s)}\tilde{v}_{1;3}^{\text{surf}}, \quad (5.19)$$

$$C = \frac{2\lambda(-js\alpha_1)}{s\hat{f}(s)}\tilde{v}_{3;3}^{\text{surf}}, \quad (5.20)$$

$$D = \frac{2(\lambda+2\mu)}{s\hat{f}(s)}\tilde{v}_{3;3}^{\text{surf}}, \quad (5.21)$$

$$E = \frac{2\mu}{s\hat{f}(s)} \tilde{v}_{1;1}^{\text{surf}}, \quad (5.22)$$

$$F = \frac{2\mu(-js\alpha_1)}{s\hat{f}(s)} \tilde{v}_{1;1}^{\text{surf}}, \quad (5.23)$$

$$G = \frac{2\mu}{s\hat{f}(s)} \tilde{v}_{3;1}^{\text{surf}}, \quad (5.24)$$

$$H = \frac{2\mu(-js\alpha_1)}{s\hat{f}(s)} \tilde{v}_{3;1}^{\text{surf}} + 2. \quad (5.25)$$

Interesting in this result is the fact that the matrix equation is decoupled with respect to the source direction. In order to solve eq. (5.17), all source and receiver combinations of the data are needed to define the matrix elements $A \dots H$ and the vector on the right hand side, but we can independently solve for data without surface effects, with the source in the x_1 -direction ($\tilde{v}_{1;1}^{\text{inc}}$ and $\partial_3 \tilde{v}_{3;1}^{\text{inc}}$), or with the source in the x_3 -direction ($\tilde{v}_{3;3}^{\text{inc}}$ and $\partial_3 \tilde{v}_{1;3}^{\text{inc}}$).

5.5 Numerical test and results

In this section, we test the method described in the previous section on a synthetic dataset. The dataset is once again obtained by modeling with a finite difference method, as developed by Falk [1998]. The model for the dataset is of course a homogeneous halfspace. The P-wave velocity is 500 m/s, and the S-wave velocity is 250 m/s. The mass density is 2000 kg/m³. The receiver spacing is 1.0 m. The sampling interval in time is 0.001 s. We again use a Ricker-wavelet with a peak frequency of 33.3333 Hz as the source wavelet. This wavelet was already shown in Figure 3.7.

The dataset consists of four shot records. One where the source points in the x_1 -direction and the receivers point in the x_1 -direction (the $v_{1;1}^{\text{surf}}$ -component), one where the source points in the x_1 -direction and the receivers point in the x_3 -direction (the $v_{3;1}^{\text{surf}}$ -component), one where the source points in the x_3 -direction and the receivers point in the x_1 -direction (the $v_{1;3}^{\text{surf}}$ -component), and finally, one where the source points in the x_3 -direction and the receivers point in the x_3 -direction (the $v_{3;3}^{\text{surf}}$ -component). Each record contains 201 receivers, in a split-spread configuration. The data of the $\tilde{v}_{1;1}^{\text{surf}}$ -component and the $\tilde{v}_{3;3}^{\text{surf}}$ -component are shown in Figure 5.3. The data are spatially tapered to reduce edge effects, and only the non-tapered parts are shown. A Rayleigh wave is indeed dominant in these pictures. In Figure 5.3a, there is also a direct P-wave visible. In Figure 5.3b, there is an event with

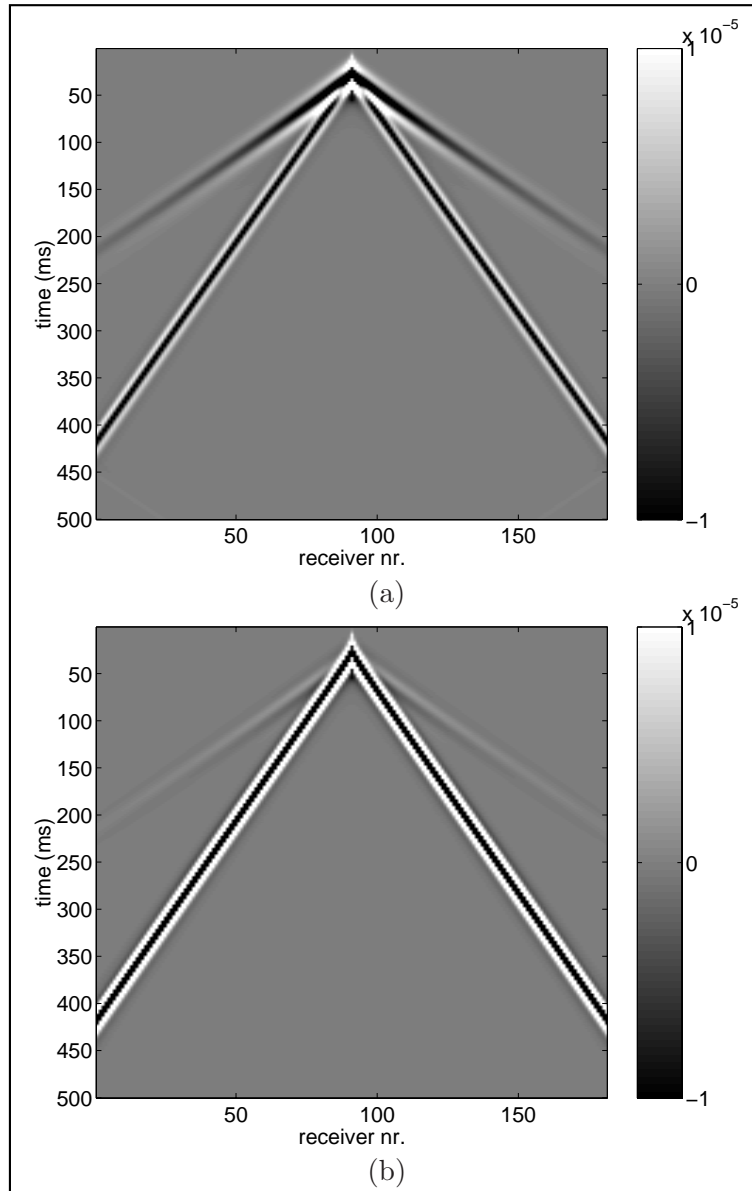


Figure 5.3: Shot records containing a Rayleigh wave, (a) $v_{1;1}^{surf}$ -component, (b) $v_{3;3}^{surf}$ -component.

the same P-wave velocity, but this is near-field P-wave (see Appendix B, eq. (B.30)).

Figure 5.4 shows the data after the application of the removal method, eq. (5.17). In Figure 5.4a, it is immediately obvious that the Rayleigh wave has been removed. What remains in this record are the direct P-wave, and a near-field SV-wave (see Appendix B, eq. (B.25)). In Figure 5.4b, the Rayleigh wave has also been removed. What remains here are the direct SV-wave, which of course has a larger amplitude than its near-field counterpart in Figure 5.4a, and a near-field P-wave (see Appendix B, eq. (B.30)). Notice that the dominant event in Figure 5.4b indeed is the direct SV-wave and not a Rayleigh wave, since the phase of the wave is different, and it has a slightly higher group velocity. Also, the amplitudes in this figure are much lower than in Figure 5.3b.

During the implementation of eq. (5.17), we found that the bottom-right part of the matrix was almost ill-conditioned. This is probably because the Rayleigh wave we are trying to remove has almost the same velocity as the desired remaining direct SV-wave. This ill-conditioning resulted in large artifacts in the data. We countered this by taking a larger value for the real part of the Laplace parameter, ε . Instead of the usual $\varepsilon = 4$, we took $\varepsilon = 8$. With this, the matrix was no longer ill-conditioned, and the artifacts are largely suppressed.

5.6 Removing surface effects from horizontally layered media

We already saw that eq. (5.12) is unsolvable by itself. We need to find auxiliary relations for the particle velocity if we want to solve for true unknown wavefield quantities, $\tilde{v}_{n;m}^{\text{ref,P}}$ and $\tilde{v}_{m;n}^{\text{ref,SV}}$, in the less trivial case of a horizontally layered medium. Luckily, they can be found fairly easy.

Although P- and SV-waves are decoupled and propagate independent, their respective particle velocity components are not independent. When we look at eq. (2.29) and eq. (2.30), we see that we can write for P-waves in the horizontal slowness domain:

$$\begin{aligned}\tilde{v}_{1;n}^{\text{ref,P}} &= (-js\alpha_1)\tilde{\Phi}^{\text{ref}}, \quad \text{and} \\ \tilde{v}_{3;n}^{\text{ref,P}} &= s\gamma_p\tilde{\Phi}^{\text{ref}}.\end{aligned}\tag{5.26}$$

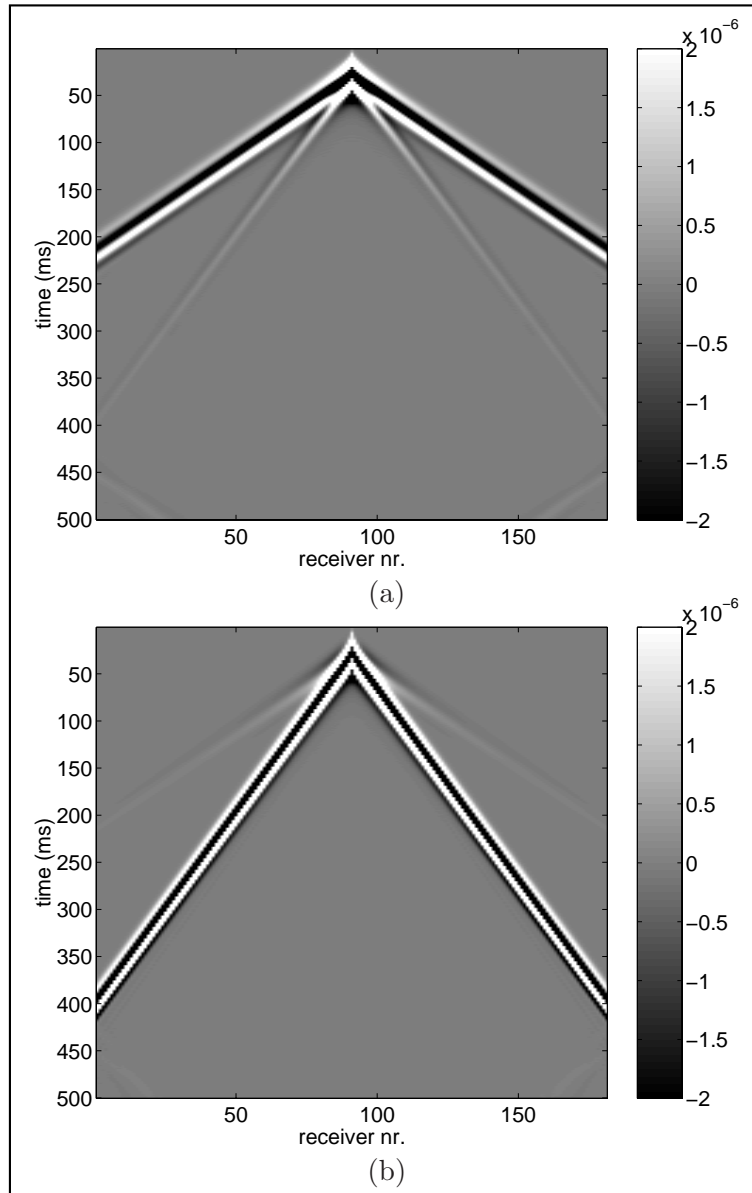


Figure 5.4: Shot records after applying the removal method, eq. (5.17) (a) $v_{1;1}^{\text{nosurf}}$ -component, (b) $v_{3;3}^{\text{nosurf}}$ -component.

And for SV-waves:

$$\begin{aligned}\tilde{v}_{1;n}^{\text{ref,SV}} &= -s\gamma_s \tilde{\Psi}_2^{\text{ref}}, \quad \text{and} \\ \tilde{v}_{3;n}^{\text{ref,SV}} &= (-js\alpha_1) \tilde{\Psi}_2^{\text{ref}}.\end{aligned}\quad (5.27)$$

In these equations, remember that the reflected wavefield is an up-going field. Alternatively, we can write:

$$\tilde{v}_{1;n}^{\text{ref,P}} = \frac{(-js\alpha_1)}{s\gamma_p} \tilde{v}_{3;n}^{\text{ref,P}}, \quad (5.28)$$

$$\tilde{v}_{3;n}^{\text{ref,SV}} = \frac{(-js\alpha_1)}{-s\gamma_s} \tilde{v}_{1;n}^{\text{ref,SV}}. \quad (5.29)$$

These are four equations ($n = 1\&3$), which are independent of eq. (5.12). With them, the problem should be solvable.

We take all source functions equal, like in Section 5.4, and divide eq. (5.12) through this wavelet, to arrive at expressions similar to the final expressions in Chapter 3.

The set of equations formed by eq. (5.12), eq. (5.28) and eq. (5.29) can be formed into a matrix equation. Since we now have eight equations with eight unknowns, the matrix will be a square eight by eight matrix, and will have the form:

$$\begin{pmatrix} \mathcal{A} & \mathcal{B} & \mathcal{C} & \mathcal{D} & 0 & 0 & 0 & 0 \\ 1 & 0 & \mathcal{E} & 0 & 0 & 0 & 0 & 0 \\ \mathcal{F} & \mathcal{G} & \mathcal{H} & \mathcal{I} & 0 & 0 & 0 & 0 \\ 0 & \mathcal{J} & 0 & 1 & 0 & 0 & 0 & 0 \\ 0 & 0 & 0 & 0 & \mathcal{K} & \mathcal{L} & \mathcal{M} & \mathcal{N} \\ 0 & 0 & 0 & 0 & 1 & 0 & \mathcal{O} & 0 \\ 0 & 0 & 0 & 0 & \mathcal{P} & \mathcal{Q} & \mathcal{R} & \mathcal{S} \\ 0 & 0 & 0 & 0 & 0 & \mathcal{T} & 0 & 1 \end{pmatrix} \cdot \begin{pmatrix} \tilde{v}_{1;1}^{\text{ref,P}} \\ \tilde{v}_{1;1}^{\text{ref,SV}} \\ \tilde{v}_{3;1}^{\text{ref,P}} \\ \tilde{v}_{3;1}^{\text{ref,SV}} \\ \tilde{v}_{1;3}^{\text{ref,P}} \\ \tilde{v}_{1;3}^{\text{ref,SV}} \\ \tilde{v}_{3;3}^{\text{ref,P}} \\ \tilde{v}_{3;3}^{\text{ref,SV}} \end{pmatrix} = \begin{pmatrix} \frac{1}{2}\tilde{v}_{1;1}^{\text{surf}} + \mathcal{U} \\ 0 \\ \frac{1}{2}\tilde{v}_{3;1}^{\text{surf}} + \mathcal{V} \\ 0 \\ \frac{1}{2}\tilde{v}_{1;3}^{\text{surf}} + \mathcal{W} \\ 0 \\ \frac{1}{2}\tilde{v}_{3;3}^{\text{surf}} + \mathcal{X} \\ 0 \end{pmatrix}, \quad (5.30)$$

where all the terms are defined as:

$$\mathcal{A} = \frac{\mu\gamma_p}{\hat{f}(s)} \tilde{v}_{1;1}^{\text{surf}} + \frac{\lambda(-js\alpha_1)}{s\hat{f}(s)} \tilde{v}_{1;3}^{\text{surf}} + 1, \quad (5.31)$$

$$\mathcal{B} = \frac{\mu\gamma_s}{\hat{f}(s)} \tilde{v}_{1;1}^{\text{surf}} + \frac{\lambda(-js\alpha_1)}{s\hat{f}(s)} \tilde{v}_{1;3}^{\text{surf}} + 1, \quad (5.32)$$

$$\mathcal{C} = \frac{\mu(-js\alpha_1)}{s\hat{f}(s)} \tilde{v}_{1;1}^{\text{surf}} + \frac{(\lambda + 2\mu)\gamma_p}{\hat{f}(s)} \tilde{v}_{1;3}^{\text{surf}}, \quad (5.33)$$

$$\mathcal{D} = \frac{\mu(-js\alpha_1)}{s\hat{f}(s)}\tilde{v}_{1;1}^{\text{surf}} + \frac{(\lambda+2\mu)\gamma_s}{\hat{f}(s)}\tilde{v}_{1;3}^{\text{surf}}, \quad (5.34)$$

$$\mathcal{E} = -\frac{(-js\alpha_1)}{s\gamma_p}, \quad (5.35)$$

$$\mathcal{F} = \frac{\mu\gamma_p}{\hat{f}(s)}\tilde{v}_{3;1}^{\text{surf}} + \frac{\lambda(-js\alpha_1)}{s\hat{f}(s)}\tilde{v}_{3;3}^{\text{surf}}, \quad (5.36)$$

$$\mathcal{G} = \frac{\mu\gamma_s}{\hat{f}(s)}\tilde{v}_{3;1}^{\text{surf}} + \frac{\lambda(-js\alpha_1)}{s\hat{f}(s)}\tilde{v}_{3;3}^{\text{surf}}, \quad (5.37)$$

$$\mathcal{H} = \frac{\mu(-js\alpha_1)}{s\hat{f}(s)}\tilde{v}_{3;1}^{\text{surf}} + \frac{(\lambda+2\mu)\gamma_p}{\hat{f}(s)}\tilde{v}_{3;3}^{\text{surf}} + 1, \quad (5.38)$$

$$\mathcal{I} = \frac{\mu(-js\alpha_1)}{s\hat{f}(s)}\tilde{v}_{3;1}^{\text{surf}} + \frac{(\lambda+2\mu)\gamma_s}{\hat{f}(s)}\tilde{v}_{3;3}^{\text{surf}} + 1, \quad (5.39)$$

$$\mathcal{J} = \frac{(-js\alpha_1)}{s\gamma_s}, \quad (5.40)$$

$$\mathcal{K} = \frac{\mu\gamma_p}{\hat{f}(s)}\tilde{v}_{1;1}^{\text{surf}} + \frac{\lambda(-js\alpha_1)}{s\hat{f}(s)}\tilde{v}_{1;3}^{\text{surf}} + 1, \quad (5.41)$$

$$\mathcal{L} = \frac{\mu\gamma_s}{\hat{f}(s)}\tilde{v}_{1;1}^{\text{surf}} + \frac{\lambda(-js\alpha_1)}{s\hat{f}(s)}\tilde{v}_{1;3}^{\text{surf}} + 1, \quad (5.42)$$

$$\mathcal{M} = \frac{\mu(-js\alpha_1)}{s\hat{f}(s)}\tilde{v}_{1;1}^{\text{surf}} + \frac{(\lambda+2\mu)\gamma_p}{\hat{f}(s)}\tilde{v}_{1;3}^{\text{surf}}, \quad (5.43)$$

$$\mathcal{N} = \frac{\mu(-js\alpha_1)}{s\hat{f}(s)}\tilde{v}_{1;1}^{\text{surf}} + \frac{(\lambda+2\mu)\gamma_s}{\hat{f}(s)}\tilde{v}_{1;3}^{\text{surf}}, \quad (5.44)$$

$$\mathcal{O} = -\frac{(-js\alpha_1)}{s\gamma_p}, \quad (5.45)$$

$$\mathcal{P} = \frac{\mu\gamma_p}{\hat{f}(s)}\tilde{v}_{3;1}^{\text{surf}} + \frac{\lambda(-js\alpha_1)}{s\hat{f}(s)}\tilde{v}_{3;3}^{\text{surf}}, \quad (5.46)$$

$$\mathcal{Q} = \frac{\mu\gamma_s}{\hat{f}(s)}\tilde{v}_{3;1}^{\text{surf}} + \frac{\lambda(-js\alpha_1)}{s\hat{f}(s)}\tilde{v}_{3;3}^{\text{surf}}, \quad (5.47)$$

$$\mathcal{R} = \frac{\mu(-js\alpha_1)}{s\hat{f}(s)}\tilde{v}_{3;1}^{\text{surf}} + \frac{(\lambda+2\mu)\gamma_p}{\hat{f}(s)}\tilde{v}_{3;3}^{\text{surf}} + 1, \quad (5.48)$$

$$\mathcal{S} = \frac{\mu(-js\alpha_1)}{s\hat{f}(s)}\tilde{v}_{3;1}^{\text{surf}} + \frac{(\lambda+2\mu)\gamma_s}{\hat{f}(s)}\tilde{v}_{3;3}^{\text{surf}} + 1, \quad (5.49)$$

$$\mathcal{T} = \frac{(-js\alpha_1)}{s\gamma_s}, \quad (5.50)$$

$$\mathcal{U} = -\tilde{v}_{1;1}^{\text{inc}} - \left(\frac{\lambda(-js\alpha_1)}{s\hat{f}(s)} \tilde{v}_{1;1}^{\text{inc}} + \frac{(\lambda+2\mu)}{s\hat{f}(s)} \partial_3 \tilde{v}_{3;1}^{\text{inc}} \right) \tilde{v}_{1;3}^{\text{surf}}, \quad (5.51)$$

$$\mathcal{V} = - \left(\frac{\lambda(-js\alpha_1)}{s\hat{f}(s)} \tilde{v}_{1;1}^{\text{inc}} + \frac{(\lambda+2\mu)}{s\hat{f}(s)} \partial_3 \tilde{v}_{3;1}^{\text{inc}} \right) \tilde{v}_{3;3}^{\text{surf}}, \quad (5.52)$$

$$\mathcal{W} = - \left(\frac{\mu(-js\alpha_1)}{s\hat{f}(s)} \tilde{v}_{3;3}^{\text{inc}} + \frac{\mu}{s\hat{f}(s)} \partial_3 \tilde{v}_{1;3}^{\text{inc}} \right) \tilde{v}_{1;1}^{\text{surf}}, \quad (5.53)$$

$$\mathcal{X} = -\tilde{v}_{3;3}^{\text{inc}} - \left(\frac{\mu(-js\alpha_1)}{s\hat{f}(s)} \tilde{v}_{3;3}^{\text{inc}} + \frac{\mu}{s\hat{f}(s)} \partial_3 \tilde{v}_{1;3}^{\text{inc}} \right) \tilde{v}_{3;1}^{\text{surf}}. \quad (5.54)$$

This matrix equation is also decoupled with respect to the source direction, much the same as eq. (5.17). The actual implementation of eq. (5.30) is left open for future research.

Conclusions

This thesis presented a method to remove Love waves (and other surface effects) from land seismic data. This final chapter summarizes the method, discusses the main results obtained on synthetic datasets and field data, and proposes possible subjects for future research.

In shallow seismic SH-wave experiments, the data are often severely polluted with surface related wave phenomena, the most important of which are Love waves. Conventional methods to remove these Love waves are often unsuccessful, most importantly because their group velocity is almost equal to the shear wave velocity. A method to remove Love waves from seismic SH-wave data is an important pre-processing step. This method should not be dependent on a priori information about the subsurface, and should not disturb the desired reflection events.

In this thesis, we derived a method, based on the Betti-Rayleigh field reciprocity theorem, that removes surface effects like Love waves from seismic land data, and where the data *itself* carries all the information needed to distinguish Love waves (and other surface related wave phenomena) from the other events present in the data. Reciprocity is a mathematical tool to describe the interaction between two different states. By taking one state as the actual (Love wave containing) configuration, where the medium is

bounded by a stress-free surface, and the other state as an ideal (Love wave free) configuration, where this surface is absent, we derived an integral equation of the second kind from which the Love wave free velocity wavefield can be solved as a function of the Love wave contaminated data. Other input parameters are: the soil properties of the top layer, which are the shear wave velocity c_s and the shear modulus μ (or alternatively, the mass density ρ), and the source wavelet.

In discrete notation, the integral equation becomes a matrix equation, which can be solved with conventional matrix operations such as *inversion*. Another technique used to solve integral equations of the second kind, the *Neumann series expansion*, can not be used, due to the fact that Love wave “multiples” occur mainly in the evanescent regime, and are thus hardly separated in time. This means that when the norm of the kernel of the integral equation is greater than one (which it usually is), too many updates of the series are needed before the computer reaches machine precision.

When the medium is horizontally layered, the kernel of the integral equation becomes diagonal, and the equation reduces to a simple scalar expression. The usefulness of this expression is limited, since it has to be applied to CDP-gathers, while seismic SH-wave data are often severely spatially aliased due to the low velocity of shear waves (especially in soft soils), and this is even more so with CDP-gathers.

We tested the method on several synthetic datasets. The datasets were all modeled with the finite difference method. In all of the cases, the removal method had no problems with removing the Love waves completely from the data. It even removed noise in the form of scattered Love waves, in the examples where such noise was present. In all cases, the data matched the response of a medium without a stress-free surface after the application of the removal procedure. The computation takes about two and a half hours for a dataset consisting of 251 shots with 241 traces per shot, with 120 frequencies to be solved.

The method was not very sensitive to errors in the estimation of the input parameters. The shear wave velocity can be chosen within a factor of two of the real value, and the mass density even provides satisfactory results when it is chosen five times too high. The deviation in the phase of the source wavelet can be up to 60 degrees, although larger phase shifts introduce much more noise into the data.

The data itself can also carry severe distortions and still produce satis-

factory results. For example, when there is a stochastic noise level as high as the amplitude of the reflections in the data, or when anelastic attenuation with a quality factor as low as 10 is introduced, it poses no problem for the method. We also examined the effects of (slight) spatial aliasing, a missing trace in the data and 3-D effects on the performance of the method, but in all cases, the method still manages to remove the Love waves from the data. The method seemed to be very robust.

In Chapter 5, an initiative is taken to remove Rayleigh waves and other surface effects from coupled P- and SV-wave systems, using the same technique, derived from elastic reciprocity. Once again, we defined one state where the surface is bounded by a stress free surface, and one state where the surface is absent, and applied the Betti-Rayleigh reciprocity theorem. The difference is that, in this case, the sources and receivers do not point in the crossline (x_2) direction, but in the vertical (x_3) and inline (x_1) direction.

Since P- and SV-waves are coupled, application of the reciprocity theorem also leads to coupled equations. However, the final equation is decoupled with respect to the source direction. This means that, even though all source and receiver combinations are needed to make the removal operator, the data can be solved independently for the source in the x_1 - or the x_3 -direction.

We modeled a dataset with finite difference modeling. The dataset consisted of four shots (the source and the receiver can each point into the x_1 - or the x_3 -direction). The model was a simple unbounded halfspace, so the only waves that occur are a (non-dispersive) Rayleigh wave and the direct waves. The method managed to remove the Rayleigh wave and leave the direct waves intact.

In Appendix C, we test the Love wave removal method on a field dataset. We shot a dataset at the site of the Sofia tunnel (before it was drilled) near Hendrik Ido Ambacht in the Netherlands. At first sight, the data seemed to be of good quality. Over the whole of the line, the data contained Love waves which behaved almost exactly like the ones in the synthetic example.

However, application of the method did not remove the Love waves from the data. Quite the contrary, the method introduced more noise into the data.

Even though we could not pinpoint the exact reason why the removal method does not produce satisfactory results on field data, we did rule out some of the possibilities:

- It is not due to spatial aliasing, since we interpolated the data both in the common shot domain and in the common receiver domain.
- It is not due to differences in the source wavelet (which the method assumes are equal). The variations in the recorded vibrator source wavelets are minor, which we checked in the time domain as well as in the frequency domain (both the amplitude and the phase of the wavelet). Besides, deconvolving with these wavelets resulted in nice pulse-like wavelets, and this is a strong indication that they are correct.
- It is not due to differences in shot strengths. Even though there is some variation in the shot strength, when we applied the same weights on a synthetic dataset, the method did still produce good results.

Some of the possible reasons for the poor results, but which we were unable to check, are:

- Near-field effects. Near-field effects do not occur when the SH-waves are created with line sources. In a field experiment, the sources behave more like point sources, and near-field effects do occur. Checking what effect the near field has on Love waves and their subsequent removal would require 3-D finite difference modeling. This was deemed to be computationally too expensive.
- Anisotropy. We assumed that the top layer of the medium is homogeneous and isotropic. Previous studies showed however, that the highest degree of anisotropy occurs in these top layers. This means that the polarization of the traveling wave is rotated as it propagates through the medium. Therefore, although the wave will still be a decoupled SH-wave, it will have components in both the crossline (x_2) direction and the inline (x_1) direction. This will have an effect on the amplitude and the phase of the wave, when we measure only the crossline component.
- A combination of effects described above. Each time we ruled out a possible cause, this was done in a way where we examined the effect of the cause on the Sofia dataset, and then applied the same effect on a synthetic dataset. Therefore, each time, the synthetic dataset suffered from only one distortion, while the Sofia dataset suffers from all of them. If a combination of effects is the cause, then it is hard to discover which combination, and where exactly the threshold lies.

Even though we could not make the Love wave removal method work on a field dataset, we are still confident that it has a high potential. Perhaps with a few modifications to the theory, like taking the anelastic attenuation into account with complex values for the medium parameters, or incorporating the near-field effects when constructing a line source response, the method will provide good results.

Appendix D shows an attempt at a wavelet estimation. It is based on energy minimization. The idea was that only the correct wavelet will remove the most energy from the data. This attempt was also not successful, because when the wavelet goes to zero, the data also goes to zero, and this is obviously not the solution we are looking for.

A

Integral transforms and their properties

Throughout the theory, we use Laplace transforms and spatial Fourier transforms for the derivation of the equations. These transforms are defined here, and some of their most relevant properties are discussed.

A.1 The Laplace transform

■ A.1.1 Continuous Laplace transform

In view of causality, we assume that a wavefield generated by sources is only not equal to zero, after a time $t = 0$, which defines the time when the sources are fired. If we introduce the characteristic function $\chi_T(t)$ as:

$$\chi_T(t) = \begin{cases} 0, & t < 0, \\ \frac{1}{2}, & t = 0, \\ 1, & t > 0, \end{cases} \quad (\text{A.1})$$

then the Laplace transform of a causal function $u(\mathbf{x}, t)$ in space and time is defined as:

$$\mathcal{L}_t \{u(\mathbf{x}, t)\} = \hat{u}(\mathbf{x}, s) = \int_{t \in \mathbb{R}} \chi_T(t) u(\mathbf{x}, t) e^{-st} dt. \quad (\text{A.2})$$

To ensure convergence of eq. (A.2), the Laplace parameter s must satisfy the constraint $\text{Re}(s) > 0$. When we take the limiting case of a completely imaginary Laplace parameter, $s \rightarrow j\omega$, where ω is the angular frequency, we arrive at the temporal Fourier transform.

The function $\hat{u}(\mathbf{x}, s)$ can be transformed back to the time domain by evaluating the Bromwich integral (Bracewell [1987]), which is defined as:

$$\frac{1}{2\pi j} \int_{\varepsilon-j\infty}^{\varepsilon+j\infty} \hat{u}(\mathbf{x}, s) e^{st} ds = \chi_T(t) u(\mathbf{x}, t). \quad (\text{A.3})$$

The path of integration in this equation is the line parallel to the imaginary axis of the complex s -domain ($s = \varepsilon, \varepsilon \in \mathbb{R}^+$), on the right side of this domain, since this is where the Laplace transform itself is defined.

The Laplace transform of a function differentiated to time can be found when we take the time derivative of the complete integrand in eq. (A.2):

$$\begin{aligned} \int_{t \in \mathbb{R}} \partial_t [\chi_T(t) u(\mathbf{x}, t) e^{-st}] dt &= \int_{t \in \mathbb{R}} [\partial_t \chi_T(t)] u(\mathbf{x}, t) e^{-st} dt + \\ &\int_{t \in \mathbb{R}} \chi_T(t) [\partial_t u(\mathbf{x}, t)] e^{-st} dt + \int_{t \in \mathbb{R}} \chi_T(t) u(\mathbf{x}, t) [\partial_t e^{-st}] dt. \end{aligned} \quad (\text{A.4})$$

It is the second term on the right hand side that we are interested in. The term on the left hand side yields zero. For the first term on the right hand side, we find:

$$\int_{t \in \mathbb{R}} [\partial_t \chi_T(t)] u(\mathbf{x}, t) e^{-st} dt = \lim_{t \downarrow 0} u(\mathbf{x}, t), \quad (\text{A.5})$$

and for the third term on the right hand side:

$$\int_{t \in \mathbb{R}} \chi_T(t) u(\mathbf{x}, t) [\partial_t e^{-st}] dt = -s \hat{u}(\mathbf{x}, t). \quad (\text{A.6})$$

Therefore, for the Laplace transform of a function differentiated to time, we find:

$$\int_{t \in \mathbb{R}} \chi_T(t) [\partial_t u(\mathbf{x}, t)] e^{-st} dt = s \hat{u}(\mathbf{x}, t) - \lim_{t \downarrow 0} u(\mathbf{x}, t). \quad (\text{A.7})$$

This equation shows that a differentiation to time is equivalent to a multiplication with a factor s in the Laplace domain, together with a correction due to the jump of the function as it passes the instant $t = 0$. In most practical cases, it can be assumed that $u(\mathbf{x}, t) = 0$ for $t = 0$, and thus, only the multiplication with s remains.

■ A.1.2 Numerical implementation

For the numerical implementation of the Laplace transform, we take a complex Laplace parameter:

$$s = \varepsilon + j\omega, \quad (\text{A.8})$$

where, according to our earlier statement, $\varepsilon > 0$. If ε is taken constant, the forward Laplace transform, eq. (A.2), becomes:

$$\hat{u}(\mathbf{x}, \varepsilon + j\omega) = \int_{t \in \mathbb{R}} \chi_T(t) [u(\mathbf{x}, t) e^{-\varepsilon t}] e^{-j\omega t} dt. \quad (\text{A.9})$$

This equation is a normal forward Fourier transform, but after the application of an exponential taper on the function. The integral converges when the function $u(\mathbf{x}, t) e^{-\varepsilon t}$ is absolute integrable. Also, singularities along the path of integration are avoided with this definition.

The function $\chi_T(t)u(\mathbf{x}, t)$ can be obtained from its Laplace-domain counterpart. The Bromwich integral, eq. (A.3), becomes an inverse temporal Fourier transform:

$$\frac{e^{\varepsilon t}}{2\pi} \int_{\omega \in \mathbb{R}} \hat{u}(\mathbf{x}, \varepsilon + j\omega) e^{j\omega t} d\omega = \chi_T(t)u(\mathbf{x}, t). \quad (\text{A.10})$$

From eq. (A.9), and keeping in mind that $u(\mathbf{x}, t)$ is real, it follows that $\hat{u}(\mathbf{x}, \varepsilon - j\omega) = \hat{u}^*(\mathbf{x}, \varepsilon + j\omega)$, with the star (*) denoting the complex conjugate. Therefore, the inverse transform can also be written as:

$$\chi_T(t)u(\mathbf{x}, t) = 2\text{Re} \left\{ \frac{e^{\varepsilon t}}{2\pi} \int_0^\infty \hat{u}(\mathbf{x}, \varepsilon + j\omega) e^{j\omega t} d\omega \right\}. \quad (\text{A.11})$$

Since an elastic medium has an equilibrium state, when there are no waves propagating, there will be no DC-component in the data, i.e. $\hat{u}(\mathbf{x}, j\omega) = 0$ for $\omega = 0$. Furthermore, we can restrict our analysis to positive frequencies only.

■ A.1.3 Discretization in the time domain

When processing seismic data on a computer, eq. (A.9) and eq. (A.10) are performed by numerical techniques. With digital devices, the function values of $u(\mathbf{x}, t)$ are only known on a discrete and finite set of points in time.

Suppose that we have N measured points in time, regularly divided by a constant width Δt . As a consequence, we will also have N data points in

the frequency domain, also regularly divided, this time by a width of $\Delta\omega$. Eq. (A.9) is now replaced by its discrete counterpart:

$$\begin{aligned} \hat{u}(\mathbf{x}, j \, k \Delta\omega) &= \Delta t \sum_{n=0}^{N-1} [e^{-\varepsilon n \Delta t} u(\mathbf{x}, n \Delta t)] e^{-j \, k \Delta\omega \, n \Delta t}, \\ \text{for } k &= -\frac{1}{2}N + 1, \dots, \frac{1}{2}N. \end{aligned} \quad (\text{A.12})$$

The frequency sampling rate $\Delta\omega$ is chosen in such a way that it agrees to the relation:

$$\Delta t \, \Delta\omega = \frac{2\pi}{N}. \quad (\text{A.13})$$

Note that the domain of integration in eq. (A.12) is chosen symmetrically around $t = 0$, i.e. $t \in [(-\frac{1}{2}N+1)\Delta t, \dots, \frac{1}{2}N\Delta t]$. Since the function $u(\mathbf{x}, n\Delta t)$ is discrete in the time domain, this means that it is periodic in the frequency domain, with period $N\Delta\omega$.

We find a similar expression for the discrete counterpart of eq. (A.10):

$$\begin{aligned} u(\mathbf{x}, n\Delta t) &= \frac{e^{\varepsilon n \Delta t \Delta\omega}}{2\pi} \sum_{k=-\frac{1}{2}N+1}^{\frac{1}{2}N} \hat{u}(\mathbf{x}, \varepsilon + j \, k \Delta\omega) e^{j \, n \Delta t \, k \Delta\omega}, \\ \text{for } n &= 0, \dots, N-1. \end{aligned} \quad (\text{A.14})$$

Since the function $\hat{u}(\mathbf{x}, j \, k \Delta\omega)$ is discrete in the frequency domain, this means that it is periodic in the time domain, with period $N\Delta t$.

Eq. (A.12) and eq. (A.14) are standard discrete Fourier transforms, apart from the multiplication with the exponential factor, and can be performed with standard numerical Fast Fourier Transform (FFT) routines.

A.2 The spatial Fourier transform

During the course of this thesis, one frequently encounters notations such as: $\hat{u}(\mathbf{x}^R | \mathbf{x}^S, s)$. This notation means a scalar wavefield quantity \hat{u} (the hat (^) denotes its representation in the Laplace domain), measured at a position \mathbf{x}^R , caused by a source at position \mathbf{x}^S . Since the coordinates \mathbf{x}^R and \mathbf{x}^S are independent, we can define two different Fourier transforms, one for each coordinate.

■ A.2.1 Fourier transform with respect to the receiver coordinate

We define the horizontal Fourier transform with respect to the receiver coordinate as:

$$\mathcal{F}_R \{ \hat{u}(x_1^R | x_1^S, s) \} = \tilde{u}(js\alpha_1^R | x_1^S, s) = \int_{x_1^R \in \mathbb{R}} \hat{u}(x_1^R | x_1^S, s) e^{js\alpha_1^R x_1^R} dx_1^R. \quad (\text{A.15})$$

Here, α_1^R is defined as the complex angular horizontal slowness. The reason for this is explained later. While α_1^R may be complex, it is chosen in such a way that $s\alpha_1^R$ is real. The horizontal slowness is related to the more commonly used horizontal wavenumber k_1^R by: $k_1^R = s\alpha_1^R$. The integral in eq. (A.15) converges when the function $\hat{u}(x_1^R | x_1^S, s)$ is integrable for the domain $\{x_1^R \in \mathbb{R} | -\infty < x_1^R < \infty\}$.

The function $\tilde{u}(js\alpha_1^R | x_1^S, s)$ can be transformed back to the space domain by means of an inverse Fourier transform:

$$\begin{aligned} \hat{u}(x_1^R | x_1^S, s) &= \mathcal{F}_R^{-1} \{ \tilde{u}(js\alpha_1^R | x_1^S, s) \} = \\ &= \frac{1}{2\pi} \int_{s\alpha_1^R \in \mathbb{R}} \tilde{u}(js\alpha_1^R | x_1^S, s) e^{-js\alpha_1^R x_1^R} ds\alpha_1^R. \end{aligned} \quad (\text{A.16})$$

The horizontal Fourier transform of a function differentiated with respect to the horizontal receiver coordinate can be found when we take the derivative with respect to the horizontal receiver coordinate of the complete integrand in eq. (A.15), a similar procedure as eq. (A.4):

$$\begin{aligned} \int_{x_1^R \in \mathbb{R}} \partial_1^R \left[\hat{u}(x_1^R | x_1^S, s) e^{js\alpha_1^R x_1^R} \right] dx_1^R &= \\ \int_{x_1^R \in \mathbb{R}} [\partial_1^R \hat{u}(x_1^R | x_1^S, s)] e^{js\alpha_1^R x_1^R} dx_1^R + \int_{x_1^R \in \mathbb{R}} \hat{u}(x_1^R | x_1^S, s) \left[\partial_1^R e^{js\alpha_1^R x_1^R} \right] dx_1^R. \end{aligned} \quad (\text{A.17})$$

We are interested in the first term on the right hand side. The integral on the left hand side yields zero, on account of Gauss' integral theorem. Therefore, we find:

$$\int_{x_1^R \in \mathbb{R}} [\partial_1^R \hat{u}(x_1^R | x_1^S, s)] e^{js\alpha_1^R x_1^R} dx_1^R = -js\alpha_1^R \tilde{u}(js\alpha_1^R | x_1^S, s). \quad (\text{A.18})$$

This equation shows that a differentiation to the x_1^R component of a function in the space domain corresponds to a multiplication with a factor $-js\alpha_1^R$ of the function in the horizontal slowness domain.

When examining the complex angular horizontal slowness parameter, we find that its dimension is [s/m], i.e. the inverse dimension of velocity. Hence, the name *slowness*. Indeed, when taking the limit $s \rightarrow j\omega$, the complex angular horizontal slowness parameter α_1^R becomes completely imaginary. We can then write: $\alpha_1^R = -jp_1^R$, in which p_1^R is the slowness parameter more commonly found in literature, for example in $(\tau-p)$ -transforms.

■ A.2.2 Fourier transform with respect to the source coordinate

The horizontal Fourier transform with respect to the source coordinates is defined as:

$$\mathcal{F}_S \{ \hat{u}(x_1^R | x_1^S, s) \} = \bar{u}(x_1^R | js\alpha_1^S, s) = \int_{x_1^S \in \mathbb{R}} \hat{u}(x_1^R | x_1^S, s) e^{-js\alpha_1^S x_1^S} dx_1^S. \quad (\text{A.19})$$

It is a similar expression as eq. (A.15), but with an opposite sign in the exponent. In Section 3.4, we use the two different Fourier transforms on data from horizontally layered media. With them, the double Fourier transform of a shift-invariant quantity becomes diagonal (i.e. only has a contribution when $s\alpha_1^R = s\alpha_1^S$), instead of an anti-diagonal one.

With the two different definitions of the Fourier transform, Parseval's theorem (Arfken [1985]) becomes:

$$\begin{aligned} \int_{x_1 \in \mathbb{R}} \hat{f}(x_1^R | x_1, s) \hat{g}(x_1 | x_1^S, s) dx_1 = \\ \frac{1}{2\pi} \int_{s\alpha_1 \in \mathbb{R}} \bar{f}(x_1^R | js\alpha_1, s) \tilde{g}(js\alpha_1 | x_1^S, s) ds\alpha_1. \end{aligned} \quad (\text{A.20})$$

■ A.2.3 Discretization in the space domain

Discretization in space is almost inevitably caused by the use of geophones. Geophones are devices that measure the particle velocity at a certain point. Suppose that we have placed N geophones in the ground with a spacing of Δx_1^R . This will lead to N points with a spacing of $\Delta s\alpha_1^R$ (which is real-valued) in the horizontal slowness domain. The domains of integration are chosen symmetrically around zero for both the forward and the inverse transforms, i.e. $x_1^R \in [(-\frac{1}{2}N + 1)\Delta x_1^R, \dots, \frac{1}{2}N\Delta x_1^R]$ in the space domain, and $s\alpha_1^R \in [(-\frac{1}{2}N + 1)\Delta s\alpha_1^R, \dots, \frac{1}{2}N\Delta s\alpha_1^R]$ in the horizontal Fourier do-

main. The discrete counterparts of eq. (A.15) and eq. (A.16) are then:

$$\begin{aligned} \tilde{u}(jk\Delta s\alpha_1^R|x_1^S, s) &= \Delta x_1^R \sum_{n=-\frac{1}{2}N+1}^{\frac{1}{2}N} \hat{u}(n\Delta x_1^R|x_1^S, s) e^{j n\Delta x_1^R k\Delta s\alpha_1^R} \\ \text{for } k &= -\frac{1}{2}N+1, \dots, \frac{1}{2}N, \end{aligned} \quad (\text{A.21})$$

and

$$\begin{aligned} \hat{u}(n\Delta x_1^R|x_1^S, s) &= \frac{\Delta s\alpha_1^R}{2\pi} \sum_{k=-\frac{1}{2}N+1}^{\frac{1}{2}N} \tilde{u}(jk\Delta s\alpha_1^R|x_1^S, s) e^{-j n\Delta x_1^R k\Delta s\alpha_1^R} \\ \text{for } n &= -\frac{1}{2}N+1, \dots, \frac{1}{2}N, \end{aligned} \quad (\text{A.22})$$

where the sampling in the horizontal slowness is chosen as:

$$\Delta s\alpha_1^R \Delta x_1^R = \frac{2\pi}{N}. \quad (\text{A.23})$$

Also here it goes that, since the function $\hat{u}(n\Delta x_1^R|x_1^S, s)$ is discrete in the space domain, it is periodic in the horizontal slowness domain and vice versa. To avoid edge effects that are the result of spatial windowing, the data are usually tapered with a spatial cosine taper.

B

Elastodynamic radiation from line sources

In the theory, we sometimes needed expressions for the incident wavefields. Analytical expressions for these wavefields could be found in the literature, but usually they were formulated in the space domain, and intended for point sources. In this appendix, we will derive expressions for the incident wavefields generated by line sources.

B.1 The incident SH-wave field

We begin by restating eq. (2.20) and eq. (2.21), but without sources of deformation:

$$\partial_j \hat{\tau}_{i,j} - s \rho \hat{v}_i = -\hat{f}_i, \quad (\text{B.1})$$

$$\hat{\tau}_{i,j} = \frac{C_{i,j,p,q}}{s} \partial_p \hat{v}_q. \quad (\text{B.2})$$

For the volume density of force, we take a line source which exerts its force in the x_2 direction. Obviously, this source generates only SH-waves. Therefore, $i = 2$ and $\hat{f}_i(\mathbf{x}, s) = \hat{f}_2(s) \delta(x_1 - x_1^S) \delta(x_3 - x_3^S)$. We substitute eq. (B.2) into

eq. (B.1), assume a homogeneous and isotropic medium, and obtain:

$$\frac{C_{2,j,p,q}}{s} \partial_j \partial_p \hat{v}_q - s \rho \hat{v}_2 = -\hat{f}_2(s) \delta(x_1 - x_1^S) \delta(x_3 - x_3^S). \quad (\text{B.3})$$

Since there are only SH-waves in this configuration, we can take also $q = 2$. Furthermore, since the source is a line source, all derivatives with respect to the x_2 coordinates are zero, hence, both j and p do not take the value 2. In the remaining components of the stiffness tensor $C_{i,j,p,q}$, only two contributions remain: $C_{2,1,1,2} = \mu$ and $C_{2,3,3,2} = \mu$. Substituting this, eq. (B.3) becomes:

$$\partial_1 \partial_1 \hat{v}_2 + \partial_3 \partial_3 \hat{v}_2 - \frac{s^2}{c_s^2} \hat{v}_2 = -\frac{s}{\mu} \hat{f}_2(s) \delta(x_1 - x_1^S) \delta(x_3 - x_3^S), \quad (\text{B.4})$$

where we have to remember that $c_s^2 = \mu/\rho$.

To find a convenient solution to this differential equation, we perform a double Fourier transformation on it, not only with respect to the x_1 coordinate, but also with respect to the x_3 coordinate. This Fourier transform is defined, similar to eq. (A.15), as:

$$\check{u}(js\alpha_1, js\alpha_3, s) = \mathcal{F}_3\{\tilde{u}(js\alpha_1, x_3, s)\} = \int_{x_3 \in \mathbb{R}} \tilde{u}(js\alpha_1, x_3, s) e^{js\alpha_3 x_3} dx_3. \quad (\text{B.5})$$

Also for this Fourier transform goes, similar to the Fourier transform with respect to the x_1 coordinate, that a differentiation to the x_3 component of a function in the space domain corresponds to a multiplication with a factor $-js\alpha_3$ of the function in the horizontal slowness domain.

After applying this double Fourier transform, eq. (B.4) becomes:

$$(s^2 \alpha_1^2 + s^2 \alpha_3^2) \check{v}_2 + \frac{s^2}{c_s^2} \check{v}_2 = \frac{s}{\mu} \hat{f}_2(s) e^{js\alpha_1 x_1^S + js\alpha_3 x_3^S}. \quad (\text{B.6})$$

From this equation, we can solve \check{v}_2 :

$$\check{v}_2(js\alpha_1, js\alpha_3, s) = \frac{s \hat{f}_2(s) e^{js\alpha_1 x_1^S + js\alpha_3 x_3^S}}{\mu \left(s^2 (\alpha_1^2 + \alpha_3^2 + \frac{1}{c_s^2}) \right)}. \quad (\text{B.7})$$

To arrive at the expression we used in this thesis, we only have to perform an inverse Fourier transformation with respect to the x_3 coordinate:

$$\tilde{v}_2(js\alpha_1, x_3, s) = \frac{s}{\mu} \hat{f}_2(s) e^{js\alpha_1 x_1^S} \frac{1}{2\pi} \int_{s\alpha_3 \in \mathbb{R}} \frac{e^{js\alpha_3 x_3^S}}{s^2 (\alpha_3^2 + \gamma_s^2)} e^{-js\alpha_3 x_3} ds \alpha_3. \quad (\text{B.8})$$

Here, γ_s is defined as:

$$\gamma_s = \sqrt{\frac{1}{c_s^2} + \alpha_1^2}. \quad (\text{B.9})$$

This integral can be evaluated easily with the pole-residue theorem (see for example Fokkema and van den Berg [1993]). The integrand has a pole at either $+js\gamma_s$ or $-js\gamma_s$, depending on whether $x_3 \leq x_3^S$ or $x_3 \geq x_3^S$, respectively. Taking into account the respective residues, we find:

$$\tilde{v}_2(js\alpha_1, x_3, s) = \frac{\hat{f}_2(s)}{2\mu\gamma_s} e^{js\alpha_1 x_1^S - s\gamma_s |x_3 - x_3^S|} \quad (\text{B.10})$$

From this equation, it is obvious that a differentiation to the x_3 -coordinate becomes a multiplication with either $-s\gamma_s$ when the field is down-going ($x_3 > x_3^S$) or $+s\gamma_s$ when the field is up-going ($x_3 < x_3^S$). Also, we see that the vertical derivative of this wavefield is zero ($\partial_3 \tilde{v}_2 = 0$) when $x_3 = x_3^S$, due to the absolute-function in the exponent.

B.2 The incident P- and SV-wave field

The starting point for the calculation of the coupled P- and SV-wave system is again eq. (B.1) and eq. (B.2). This time however, the line source exerts its force in either the x_1 direction or the x_3 direction. This means that i does not take the value 2. Again, we substitute eq. (B.2) into eq. (B.1), assume a homogeneous and isotropic medium, and obtain:

$$\frac{C_{i,j,p,q}}{s} \partial_j \partial_p \hat{v}_q - s\rho \hat{v}_i = -\hat{f}_i. \quad (\text{B.11})$$

In this equation, j and p do not take the value 2, because we assumed line sources, and also $q \neq 2$, because the sources (pointing only in the x_1 or x_3 direction) generate only P- and SV-waves. Performing all summations, this gives for $i = 1$:

$$\frac{\lambda + 2\mu}{\rho} \partial_1 \partial_1 \hat{v}_1 + \frac{\lambda}{\rho} \partial_1 \partial_3 \hat{v}_3 + \frac{\mu}{\rho} \partial_3 \partial_1 \hat{v}_3 + \frac{\mu}{\rho} \partial_3 \partial_3 \hat{v}_1 - s^2 \hat{v}_1 = -\frac{s}{\rho} \hat{f}_1, \quad (\text{B.12})$$

and for $i = 3$:

$$\frac{\lambda + 2\mu}{\rho} \partial_3 \partial_3 \hat{v}_3 + \frac{\lambda}{\rho} \partial_3 \partial_1 \hat{v}_1 + \frac{\mu}{\rho} \partial_1 \partial_3 \hat{v}_1 + \frac{\mu}{\rho} \partial_1 \partial_1 \hat{v}_3 - s^2 \hat{v}_3 = -\frac{s}{\rho} \hat{f}_3. \quad (\text{B.13})$$

This can be summarized as:

$$(c_p^2 - c_s^2) \partial_j \partial_i \hat{v}_i + c_s^2 \partial_i \partial_i \hat{v}_j - s^2 \hat{v}_j = -\frac{s}{\rho} \hat{f}_j, \quad (\text{B.14})$$

where i & $j \neq 2$. In order to solve this equation, we need an expression for the coupling term $\partial_i \hat{v}_i$. In order to get there, we multiply the above equation with ∂_j , and obtain:

$$c_p^2 \partial_j \partial_j \partial_i \hat{v}_i - s^2 \partial_j \hat{v}_j = -\frac{s}{\rho} \partial_j \hat{f}_j. \quad (\text{B.15})$$

In order to get a useful expression, we perform a double Fourier transformation on this equation. One transformation is with respect to the x_1 coordinate, the other with respect to the x_3 coordinate, which is defined by eq. (B.5). We get:

$$(-js\alpha_i) \check{v}_i = \frac{(-js\alpha_i) \frac{s}{\rho} \check{f}_i}{(s^2(c_p^2\alpha_j\alpha_j + 1))}. \quad (\text{B.16})$$

Now, eq. (B.14) is also transformed to the horizontal slowness domain with a double Fourier transformation. After that, we can substitute eq. (B.16), and solve the expression for the velocity. We obtain:

$$\check{v}_i = \frac{\frac{s}{\rho} \check{f}_i}{s^2(c_s^2\alpha_j\alpha_j + 1)} + \frac{(c_p^2 - c_s^2) (-js\alpha_i) (-js\alpha_j) \frac{s}{\rho} \check{f}_j}{s^2(c_p^2\alpha_j\alpha_j + 1) s^2(c_s^2\alpha_j\alpha_j + 1)}. \quad (\text{B.17})$$

Remember that in these equations, $i \& j \neq 2$. We see that:

$$\frac{(c_p^2 - c_s^2)}{(c_p^2\alpha_j\alpha_j + 1)(c_s^2\alpha_j\alpha_j + 1)} = \frac{1}{\alpha_j\alpha_j + \frac{1}{c_p^2}} - \frac{1}{\alpha_j\alpha_j + \frac{1}{c_s^2}}. \quad (\text{B.18})$$

So finally, we can write the solution for the particle velocity:

$$\check{v}_i = \check{G}_{i,j} \frac{s}{\rho} \check{f}_j, \quad (\text{B.19})$$

in which:

$$\check{G}_{i,j} = \frac{1}{c_s^2} \check{G}_S \delta_{i,j} + \frac{(-js\alpha_i)(-js\alpha_j)}{s^2} \left(\check{G}_P - \check{G}_S \right), \quad (\text{B.20})$$

where \check{G}_P and \check{G}_S are Greens functions, similar to acoustic Greens functions (see for example Fokkema and van den Berg [1993], de Hoop [1995] or the previous section):

$$\check{G}_{P,S} = \frac{1}{s^2(\alpha_j\alpha_j + \frac{1}{c_{p,s}^2})}. \quad (\text{B.21})$$

■ B.2.1 The x_1 component of the particle velocity, due to a source in the x_1 direction

The most simple case to find incident wavefield is the one where the source is pointing in the x_1 direction, and where we consider the x_1 component of the particle velocity. We substitute $i \& j = 1$ in eq. (B.19), and obtain:

$$\tilde{v}_{1;1} = \frac{s\check{f}_1}{\mu}\check{G}_S - \frac{\alpha_1^2 s\check{f}_1}{\rho}\check{G}_P + \frac{\alpha_1^2 s\check{f}_1}{\rho}\check{G}_S. \quad (\text{B.22})$$

In order to obtain the expression in the $(js\alpha_1, x_3, s)$ -domain, we only have to perform an inverse Fourier transformation with respect to the x_3 coordinate on the Greens functions \check{G}_P and \check{G}_S , because all the other factors are independent from $js\alpha_3$. These inverse Fourier transforms are known (see Section B.1):

$$\tilde{G}_{P,S}(js\alpha_1, x_3, s) = \mathcal{F}_3^{-1}\{\check{G}_{P,S}(js\alpha_1, js\alpha_3, s)\} = \frac{e^{-s\gamma_{p,s}|x_3|}}{2s\gamma_{p,s}} \quad (\text{B.23})$$

In this equation, γ_p is defined, similarly to γ_s , as:

$$\gamma_p = \sqrt{\frac{1}{c_p^2} + \alpha_1^2}. \quad (\text{B.24})$$

A clarifying perspective is obtained when we take $x_3 = 0$, and a line source $\hat{f}_1 = \hat{f}_1(s)\delta(x_1)\delta(x_3)$. In that case, the incident field becomes:

$$\tilde{v}_{1;1} = \frac{\hat{f}_1(s)}{2\mu\gamma_s} - \frac{\alpha_1^2 \hat{f}_1(s)}{2\rho\gamma_p} + \frac{\alpha_1^2 \hat{f}_1(s)}{2\rho\gamma_s}, \quad \text{for } x_3 = 0. \quad (\text{B.25})$$

However, when we realize that:

$$\alpha_1^2 = \gamma_{p,s}^2 - \frac{1}{c_{p,s}^2}, \quad (\text{B.26})$$

then the equation becomes:

$$\tilde{v}_{1;1} = \frac{\hat{f}_1(s)}{2(\lambda + 2\mu)\gamma_p} - \frac{\gamma_p \hat{f}_1(s)}{2\rho} + \frac{\gamma_s \hat{f}_1(s)}{2\rho}, \quad \text{for } x_3 = 0. \quad (\text{B.27})$$

This equation tells us, that the x_1 -component of the particle velocity, due to a source in the x_1 -direction at the “depth level” $x_3 = 0$ consists not only of

a direct P-wave (described by the first term on the right hand side), but also of a near-field P-wave component (described by the second term on the right hand side), and, surprisingly, of a near-field S-wave component (described by the third term on the right hand side). This would not have been immediately obvious had we looked only at eq. (B.25).

■ B.2.2 The x_3 -component of the particle velocity, due to a source in the x_3 direction

Now, we try to find the incident wavefield when the source is pointing in the x_3 direction, and when we measure the x_3 component of the particle velocity. To this end, we substitute $i \& j = 3$ in eq. (B.19), and obtain:

$$\check{v}_{3;3} = \frac{s\check{f}_3}{\mu}\check{G}_S + \frac{(-js\alpha_3)(-js\alpha_3)}{s^2}\frac{s}{\rho}\check{f}_3\check{G}_P - \frac{(-js\alpha_3)(-js\alpha_3)}{s^2}\frac{s}{\rho}\check{f}_3\check{G}_S. \quad (\text{B.28})$$

The Greens functions G_P and G_S are known both in the $(js\alpha_1, js\alpha_3, s)$ -domain and in the $(js\alpha_1, x_3, s)$ -domain. But now, when performing the inverse Fourier-transformation with respect to the x_3 -coordinate, we have to take the multiplications with $-js\alpha_3$ in the second and the third term of the last equation into account. Similar to the Fourier transform with respect to the x_1 -coordinate, a multiplication with $-js\alpha_3$ in the $(js\alpha_1, js\alpha_3, s)$ -domain is equivalent to a differentiation with respect to the x_3 -coordinate in the $(js\alpha_1, x_3, s)$ -domain. We can show that:

$$\partial_3 \partial_3 \tilde{G}_{P,S} = s^2 \gamma_{p,s}^2 \tilde{G}_{P,S} - \delta(x_3), \quad (\text{B.29})$$

independent of whether it is an up-going or down-going field. After an inverse Fourier transform with respect to the x_3 -coordinate, we substitute this and eq. (B.23) into eq. (B.28), assume a line source in the form of $\hat{f}_3(s)\delta(x_1)\delta(x_3)$, observe that the delta functions cancel each other, and we obtain:

$$\check{v}_{3;3} = \frac{\hat{f}_3(s)}{2\mu\gamma_s} - \frac{\gamma_s\hat{f}_3(s)}{2\rho} + \frac{\gamma_p\hat{f}_3(s)}{2\rho}, \quad \text{for } x_3 = 0. \quad (\text{B.30})$$

Similar to eq. (B.25), this equation implies that the x_3 -component of a wavefield caused by a source in the x_3 direction consists on the “depth level” $x_3 = 0$ of a normal incident SV-wave (described by the first term on the right-hand side), a near-field SV-wave (described by the second term on the right-hand side) and a near-field P-wave (described by the third term on the right-hand side).

■ B.2.3 The x_1 -component of the particle velocity, due to a source in the x_3 direction, and vice versa

Finally, we determine the last components of the incident wavefield. They are the cross-components, i.e. the source and receiver are pointing in a different direction each. As an example, we take $i = 1$ and $j = 3$ in eq. (B.19). This yields:

$$\check{v}_{1;3} = \frac{(-js\alpha_1)(-js\alpha_3)}{s^2} (\check{G}_P - \check{G}_S) \frac{s}{\rho} \check{f}_3. \quad (\text{B.31})$$

This time, when we Fourier-transform the equation back to the $(js\alpha_1, x_3, s)$ -domain, there is only one multiplication with $(-js\alpha_3)$ which becomes a differentiation with respect to the x_3 -coordinate. So we perform a Fourier-transformation with respect to the x_3 -coordinate on eq. (B.31), substitute eq. (B.23), and perform the differentiation (and of course, the source function is defined as $\hat{f}_3(s)\delta(x_1)\delta(x_3)$). Thus we obtain:

$$\tilde{v}_{1;3} = \left(-\frac{(-js\alpha_1)\hat{f}_3(s)}{2s\rho} e^{-s\gamma_p|x_3|} + \frac{(-js\alpha_1)\hat{f}_3(s)}{2s\rho} e^{-s\gamma_s|x_3|} \right) \text{sign}(x_3). \quad (\text{B.32})$$

Remember, the sign-function is defined as:

$$\text{sign}(x) = \begin{cases} -1, & x < 0, \\ 0, & x = 0, \\ 1, & x > 0, \end{cases} \quad (\text{B.33})$$

and it is the result of the differentiation of the absolute function in the exponent.

We see that exactly on the surface $x_3 = 0$, the incident wavefield of the cross-terms is zero, due to the sign-function. However, when we perform a differentiation with respect to the x_3 -coordinate on eq. (B.32), we see that it does not equal to zero, in contrast to the other incident wavefields we derived. Instead it becomes:

$$\partial_3 \tilde{v}_{1;3} = \frac{(-js\alpha_1)\gamma_p \hat{f}_3(s)}{2\rho} - \frac{(-js\alpha_1)\gamma_s \hat{f}_3(s)}{2\rho}, \quad \text{for } x_3 = 0. \quad (\text{B.34})$$

We obtain the same expressions for the wavefields when the source and receiver directions are switched (i.e. $i = 3$ and $j = 1$).

Application on field data

In Chapter 3, we have seen that the procedure to remove Love waves from seismic SH-wave data works very well on synthetic datasets. Chapter 4 showed that even with substantial distortions in the input parameters or in the data, the method still provides good results. In this appendix, we discuss our findings of the application of the method on a field dataset.

The dataset we used was shot at the site of the Sofia tunnel before it was drilled, near Hendrik Ido Ambacht in the Netherlands (see Figure C.1 for the exact location of the site). We will use the name Sofia-dataset from now on. This site was chosen because of the excellent quality of the data in previous experiments (were it not for the dominating presence of Love waves), and because a geological subsurface model was already known, due to soil investigations needed for the construction of the tunnel. The realization of this dataset was made possible due to sponsoring of the former OYO-department in Nieuwegein in the Netherlands.

First, this appendix describes the acquisition of the dataset. Then it describes the preprocessing steps needed to arrive at a dataset suitable for the removal procedure. Finally it shows the results of the application of the removal procedure on the Sofia dataset. These results are not satisfactory. The method fails to remove Love waves from the data, and furthermore introduces more noise instead. The appendix concludes with a discussion of

the reasons behind these results, and recommendations for improvement.

C.1 Geometry of the dataset

The Sofia-dataset consists of a 2-D geometry. According to eq. (3.27) and Figure 3.6, the most ideal geometry would be split-spread roll-along, with a wide aperture. However, we only had 96 geophones at our disposal, divided over 4 cables, and therefore, a roll-along configuration is not optimal. We chose to organize the data in fixed spreads. In each spread, the geophones stay in place, and only the source is moved. It is only when a certain number of shots have been reached, that a geophone cable is moved from the beginning to the end of the line. We made 5 such spreads, with 24 shots per spread, totaling 120 shots. The data from a receiver exactly at the source position would be clipped, due to the strength of the source. Therefore, we chose to remove this zero-offset geophone and replace it after the source had been moved to the next position. A simplified version of this geometry is given in Figure C.2. We also constructed a synthetic dataset following this geometry,

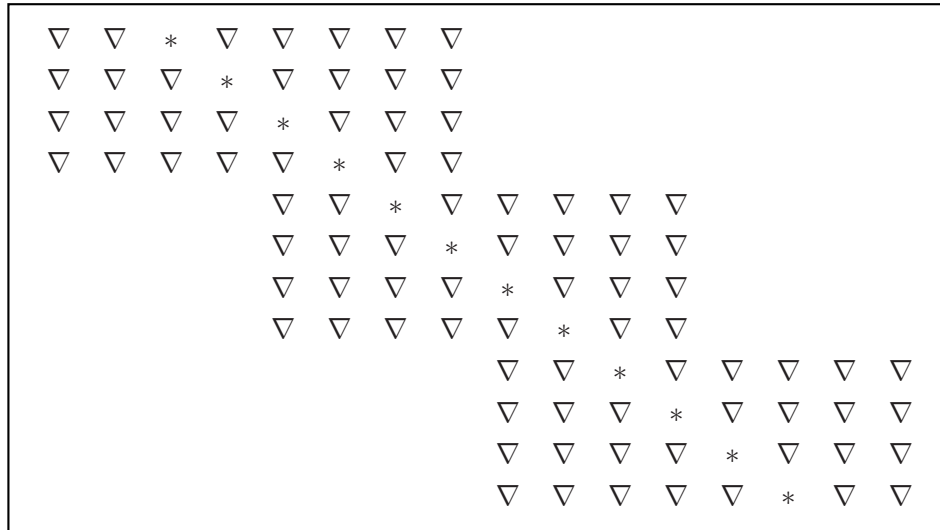


Figure C.2: Simplified geometry for 3 spreads, 4 shots per spread and 7 receivers per shot. A “▽” represents a receiver, a “*” represents a source. The Sofia dataset consists of 5 spreads, 24 shots per spread and 95 receivers per shot.

Table C.1: *Acquisition parameters of the Sofia dataset.*

number of spreads	5
number of shots per spread	24
total number of shots	120
number of traces per shot	95
source- and receiver-spacing	0.75 m
max. neg. offset at begin of swath	27.0 m
max. pos. offset at begin of swath	44.25 m
max. neg. offset at end of swath	44.25 m
max. pos. offset at end of swath	27.0 m
sample time	0.001 s
total trace length	9.0 s
starting freq. of sweep	5 Hz
end freq. of sweep	80 Hz
sweep length	7.0 s
number of sweeps per stack	4

and performed the Love wave removal method on it. No problems were encountered when using this geometry.

For the source, we used a horizontal shear-wave vibrator, developed at the former OYO-CAG department (Ghose et al. [1996]). This device has the advantage of being a controlled source, as opposed to less controllable methods, such as a sledgehammer. Other important acquisition parameters are summarized in Table C.1.

C.2 Source and receiver considerations

In order to apply the Love-wave removal method on this field data, we have to make the following assumptions regarding the source and receiver configurations and the subsurface characteristics:

- The method described in Chapter 3 assumes that all sources are line-sources. This implies that the wavefield shows a cylindric symmetry, with a corresponding amplitude decay proportional to $1/\sqrt{|x|}$ for body

waves in the far field in a homogeneous medium. The wavefields of the Sofia-dataset however, are generated by (approximately) point sources, which means that the corresponding amplitude decay is proportional to $1/|\mathbf{x}|$ for body waves in a homogeneous medium (so called spherical divergence).

Several methods exist to correct for this discrepancy in amplitude decay (Yilmaz [1987]; Wapenaar et al. [1992].) The most common method used is to multiply the data with offset-independent factors of $\sqrt{j\omega}$ in the frequency domain and \sqrt{t} in the time domain.

- The method assumes that the source signature of each shot is the same. In reality, this is hard to realize. However, each shot of the Sofia-dataset is deconvolved with its respective source-signature, measured on the source itself. Therefore, after deconvolution, each shot should have the same source-signature (which, in the frequency domain, should be 1, for the frequency range of the sweep).
- All the sources and receivers are placed upon the surface, and it is assumed that this surface is flat. Fortunately, that is not a big problem in the Netherlands . .

Also, it is assumed that the surface acts as a perfect reflector for SH-waves, because it is stress-free, and that the placement of the sources and receivers on this surface does not influence this condition.

- It is assumed that the medium is independent of the crossline (x_2) direction. In that case, the crossline component of the particle velocity will contain only SH-waves. If not, there will be pollution from other wave types in the data, and the timing of Love-waves will not be predicted correctly.
- It is assumed that there is a homogeneous and isotropic surface layer present throughout the whole area where the dataset was obtained. Chapter 4 however, showed that slight deviations in the estimated mass density and shear-wave velocity do not influence the result significantly.
- The geophones have a sensitivity of $1.67 \cdot 10^4$ mV/(m/s). The accelerometer on the vibrator has a sensitivity of 0.162 mV/N. Therefore, to obtain the displacement velocity of the geophones, the raw data has to be divided by $1.67 \cdot 10^4$. Then, because of the deconvolution, the

data has to be multiplied by 0.162. Bear in mind that the unit of the deconvolved data is then m/N.

C.3 Preprocessing steps

In order to prepare the data optimally for the application of the removal procedure, we performed the following preprocessing steps:

- Deconvolution with source wavelet. Each shot is deconvolved with its own source wavelet, which is recorded with the help of two accelerometers located on the vibrator itself. Since the mass of the vibrator is known, the actual (ground) force is easily determined.

When the response of the earth is denoted by $\hat{G}(j\omega)$ and when there is additive stochastic noise \hat{N} , then the data of a trace is obtained by: $\hat{G}(j\omega)\hat{f}_2(j\omega) + \hat{N}$. Simply dividing this expression by the source wavelet $\hat{f}_2(j\omega)$ is not feasible at the places where the source wavelet reaches zero. The division is stabilized in the following manner: $\hat{G}(j\omega) \frac{\hat{f}_2(j\omega)\hat{f}_2^*(j\omega)}{|\hat{f}_2(j\omega)|^2 + \varepsilon^2} + \hat{N} \frac{\hat{f}_2^*(j\omega)}{|\hat{f}_2(j\omega)|^2 + \varepsilon^2}$. With the proper selection of the stabilization factor ε , this expression approximates $\hat{G}(j\omega)$. In other words, the source wavelet is (approximately) 1, for the frequency range of the vibrator sweep. Figure C.3 shows one shot of the data after this deconvolution step.

- Top mute. To eliminate some anti-causal noise.
- Frequency filter: Bandpass 3-6-55-65 Hz. Even though the vibrator sweep ranges up to 80 Hz, there appeared to be much noise of 70 Hz at near offsets.
- Interpolation of dead traces with spline interpolation.
- Reconstruction of zero-offset traces. This was done with a linear interpolation of the two nearest offset traces, but where the samples were chosen such that at smaller times, an event will have a linear move-out, while at larger times, an event will have a hyperbolic move-out. The reconstructed trace was multiplied with a factor of 2.7, which was taken from the synthetic data.
- Anti-aliasing steps. The data are severely spatially aliased. Figure C.4 shows the (f, k) -spectrum of the shot displayed in Figure C.3, after

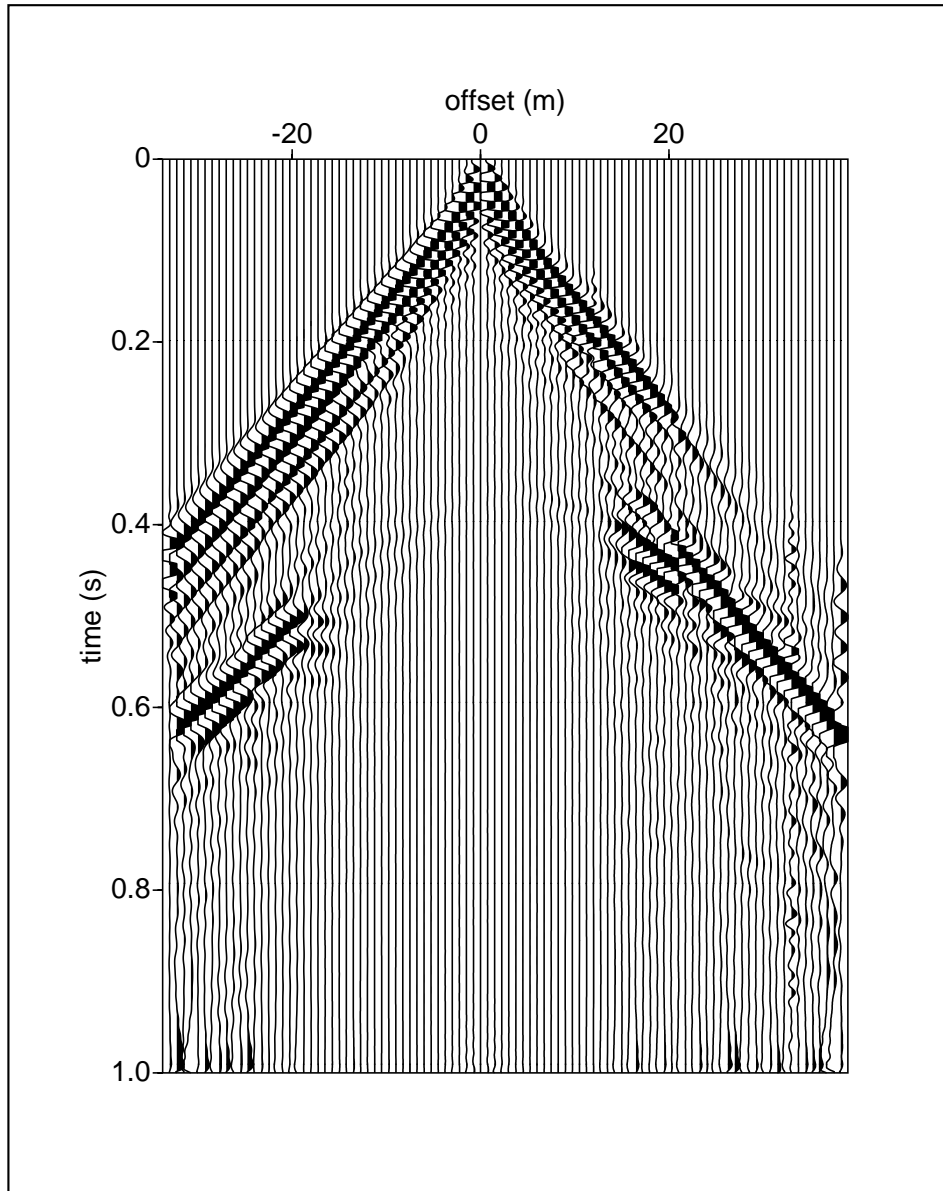


Figure C.3: Shot number 33 from the Sofia dataset. Raw data, deconvolution only. Individual trace scaling.

the pre-processing steps above. Not only are the data aliased, the aliasing starts where there is the maximum energy. Therefore, we took the following anti-aliasing steps: First we applied a Linear Move Out. This causes the data to be moved towards $k = 0$ in the (f, k) -domain. Bear in mind that this diminishes only the aliasing of the main events. Events in the form of backscattered noise become more aliased by this procedure, but we assume that this noise is not present in the data, or at least form only a minor contribution. When the data were no longer aliased, we added zeroes to the edges of the (f, k) -spectrum. Thus, we made the dataset twice as large. After transforming the data back to the space-time domain, the Linear Move Out is removed. Since the method requires that the source and receiver spacing is equal, we did the same in the common-receiver domain. So in total, the dataset became four times as large as the original dataset. Figure C.5 shows the (f, k) -spectrum of the shot, after interpolation, and Figure C.6 shows the shot in the space-time domain after interpolation and the other pre-processing steps described above.

After these pre-processing steps, the data are considered suitable for the application of the removal procedure, eq. (3.27). Figure C.6 shows one shot of the new dataset. Love waves are indeed prominent in this figure. Especially on the left side of the figure they resemble qualitatively the Love waves in the synthetic examples. There is also a very strong reflection starting at $t = 0.4$ s at the zero offset. What this figure does not show (due to the individual trace scaling), is that there is much anelastic attenuation. But as shown in Chapter 4, this should not be a problem.

C.4 Results of the removal procedure on the Sofia data

In the previous section, we explained how we prepared the Sofia-dataset for the application of the removal procedure. The most important step was the anti-aliasing procedure. When we applied the removal procedure, eq. (3.27), on these data, we could not get a good result. Instead of removing the Love waves, the method even introduced more noise into the data. Therefore, in the remainder of this appendix, we explore the possible reasons for the poor results. Since Chapter 4 explores the sensitivity of the method using only the 1-D removal scheme, eq. (3.25), we first examine some of the possible causes which are specific for the application of the removal method on the complete dataset. After that, we revert back to the 1-D removal scheme, and

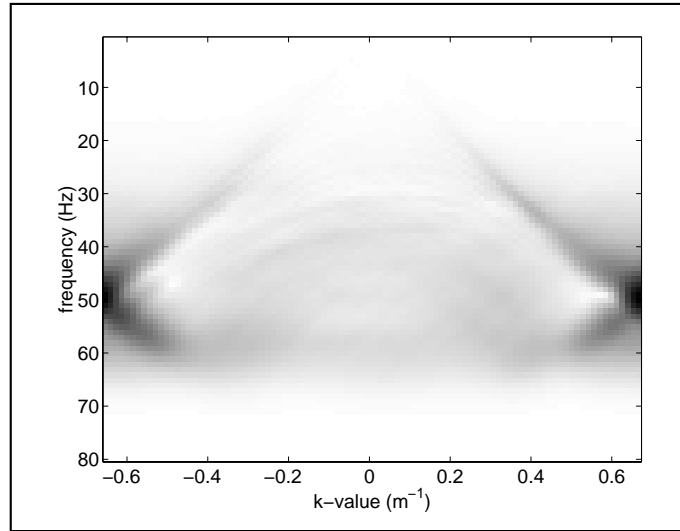


Figure C.4: (f, k) -spectrum of shot number 33 of the Sofia dataset.

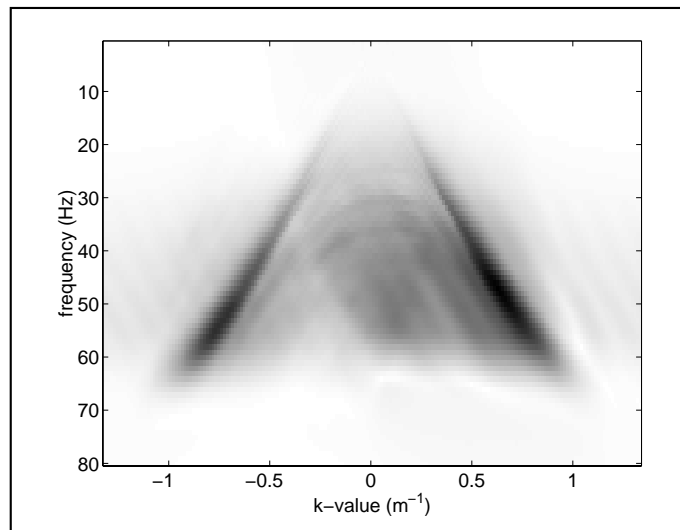


Figure C.5: (f, k) -spectrum of the same shot, after interpolation.

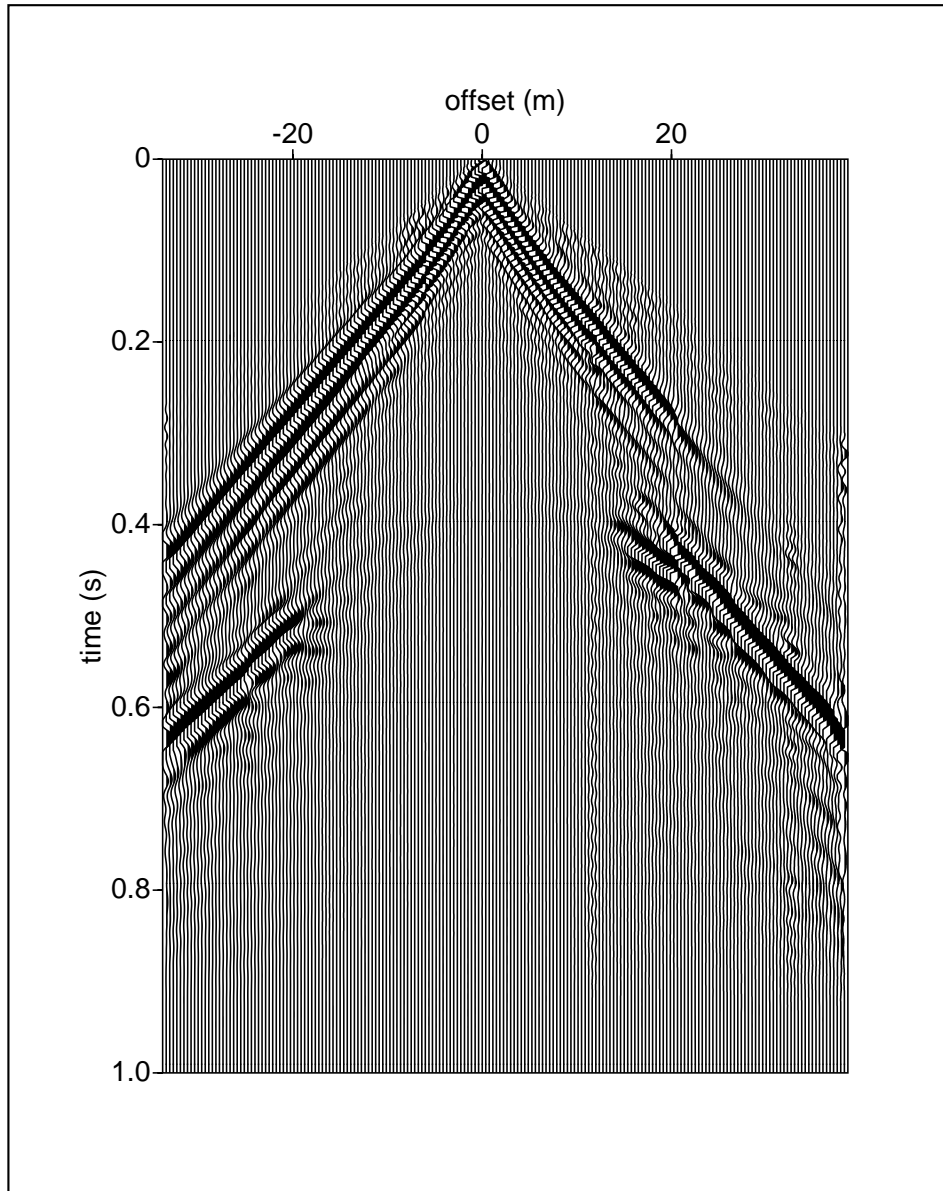


Figure C.6: Same shot as Figure C.3, after preprocessing. Shot is displayed with individual trace scaling.

take only one (modified) shot of the Sofia dataset, to take a closer look at the characteristics of the data, and the effects the removal scheme has on them.

■ C.4.1 Deviations in the source wavelets

The Love wave removal method assumes that all sources are equal. This is hard to realize. But since each shot is deconvolved with its own source wavelet, an artificial source wavelet is created that should be equal for all shots. However, if there are large deviations in the vibrator source, then this could cause large deviations in the data. Therefore, we inspected the vibrator source-wavelets first to see if there were any abnormal deviations. Figure C.7 shows frequency spectra of the vibrator sweep. In these spectra, no serious deviations are visible. We also checked source wavelets with the help of auto-correlation. The auto-correlations of the vibrator sweeps are shown in Figure C.8. Also here, all deviations certainly are within acceptable limits. We conclude that deviations in the source wavelets are not the reason that the removal method fails on the Sofia-dataset.

This was one of the first assumptions we made; that the recorded source wavelets somehow were incorrect, and that that was the reason for the poor results. In Chapter 4, we saw that a deviation in the phase of the source wavelet was the only thing that introduced noise into the data. But after the tests described above, we dismissed this idea. Indeed, if the recorded vibrator sweeps manage to collapse the wavelet into a pulse after deconvolution, then this is a strong indication that the wavelets are correct. However, we did try to develop a wavelet estimation procedure. The results of this are shown in Appendix D.

■ C.4.2 Deviations in shot-sensitivity

The relative strength of each shot could also be an important factor. When we look at eq. (3.27), we see that the method performs a Fourier transform over the source-coordinates. When one shot of the dataset is much stronger than the others, this means that one column in the matrix (see Figure 3.6), will have a large amplitude. The effect of this will be that, due to the Fourier transform, noise will be smeared over the other columns.

First, we calculated the weight of each shot. We did this by calculating the energy of each shot record (see Appendix D) in the space-time domain. These weights are shown in Figure C.9. There is indeed variation in the strength of the shots. The difference between the strongest and the weakest

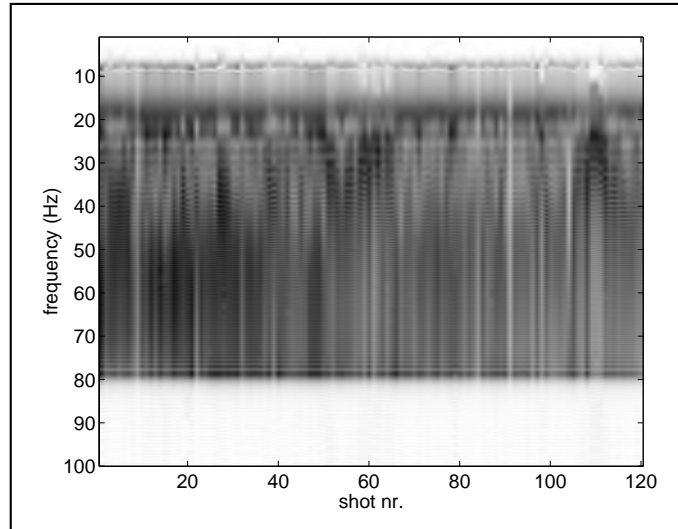


Figure C.7: *Frequency spectra of the vibrator sweeps.*

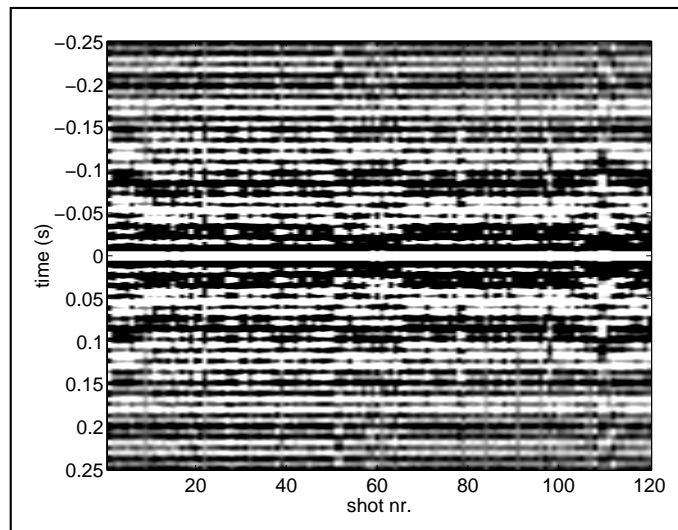


Figure C.8: *Autocorrelation of the vibrator sweeps.*

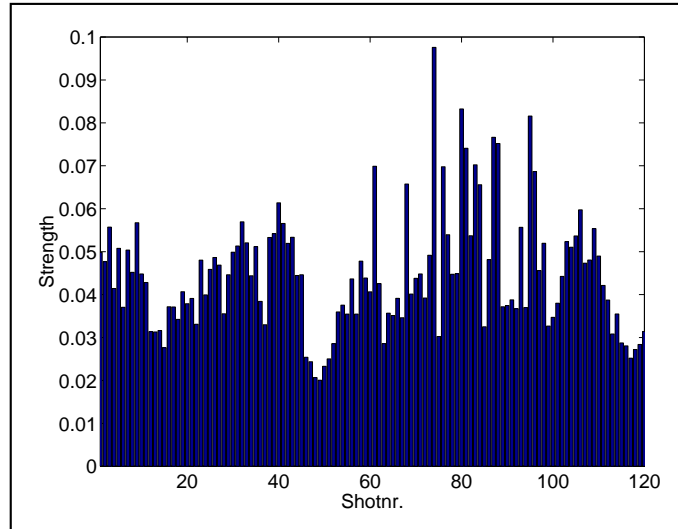


Figure C.9: Strength of each shot (calculated by the energy in each shot) of the Sofia dataset.

shot is as much as a factor of five. In the next step, we applied these weights to a synthetic dataset, where we took the weight of the first shot as the norm, and applied the removal procedure, eq. (3.27). But the results, although of course not as good as in the perfect situation, were still satisfactory. We conclude that differences in the shot strengths is not the cause of the poor results, and that normalizing the energy of each shot to the same level will also not lead to improvement.

■ C.4.3 Use of 1-D scheme to 1-D shot

Since we could not find an explanation for the poor results when examining the whole dataset, we chose to use one shot instead. With one shot, we can use the 1-D removal scheme, eq. (3.25), and display the data in the (f, k) -domain. We chose one shot where the Love waves were most similar to the ones we saw in the synthetic examples. This was the shot displayed in Figure C.6. In order to make the data more consistent with data from a horizontally layered medium, we mirrored the negative offsets of this shot (bear in mind that we could not use CDP-gathers, since they would be aliased

just as much as the uninterpolated data). Figure C.10 shows the resulting shot that we are going to use.

In Chapter 4, we stated that the mass density, ρ , can be used as a “fudge factor”. When we take $\rho = 0$, the method should do nothing, and the original input data should be returned. This is shown in Figure C.11.

In Figures C.12 and C.13, we show the results of the removal procedure where we chose the mass density as 3000 kg/m^3 and 5000 kg/m^3 , respectively.

Figures C.12 and C.13 show how the Love wave removal method operates on the data. The method does not remove the Love waves, but instead makes them stronger and more dispersive. In addition to that, noise is introduced, which seems to come from an unstable point near $k_x = 0$ in the (f, k) -domain. The denominator of eq. (3.25) apparently reaches zero at that point, although we never had such problems with the synthetic examples. Even though the division is stabilized with a technique similar to the one used for the deconvolution, this leads only to a suppression of the unstable point, while the surrounding area still gives large values. Therefore, in Figure C.14, we show the result of the removal procedure where we filtered the unstable point out of the data. This removes much of the noise, but it just makes it more clear that the Love waves have increased in strength instead of being suppressed. Even the desired reflection events have been obscured.

The fact that the Love waves are increasing in strength instead of decreasing, could be an indication that the sign of the data is erroneous. This would mean that instead of using $1 + \frac{\tilde{v}_2^{\text{surf}}}{2\tilde{v}_2^{\text{inc}}}$ in eq. (3.25), we should use $1 - \frac{\tilde{v}_2^{\text{surf}}}{2\tilde{v}_2^{\text{inc}}}$. We checked this, and it proved not to be the case. With this change, the unstable points appear in different points of the (f, k) -spectrum, but the Love waves still increase in strength, while also the desired reflection information is disturbed.

When the mass density goes to infinity, the total solution of the removal method goes to zero. But when a large, but finite, value is chosen for the mass density, the method will estimate a direct (incident) wave in the data, while the original data are suppressed. This is shown in Figure C.15. The wave in this figure looks qualitatively like a (derivative of a) Klauder wavelet. Notice how it is anti-causal, and no longer dispersive. The rest of the data, including the reflection, has vanished.

We have shown that for extreme choices of the mass density ($\rho = 0 \text{ kg/m}^3$ and $\rho = 50,000 \text{ kg/m}^3$), the method behaves as predicted. But for choices of the mass density which are realistic, the method behaves not as expected. Somehow, the phase behavior of the data is fundamentally different from the

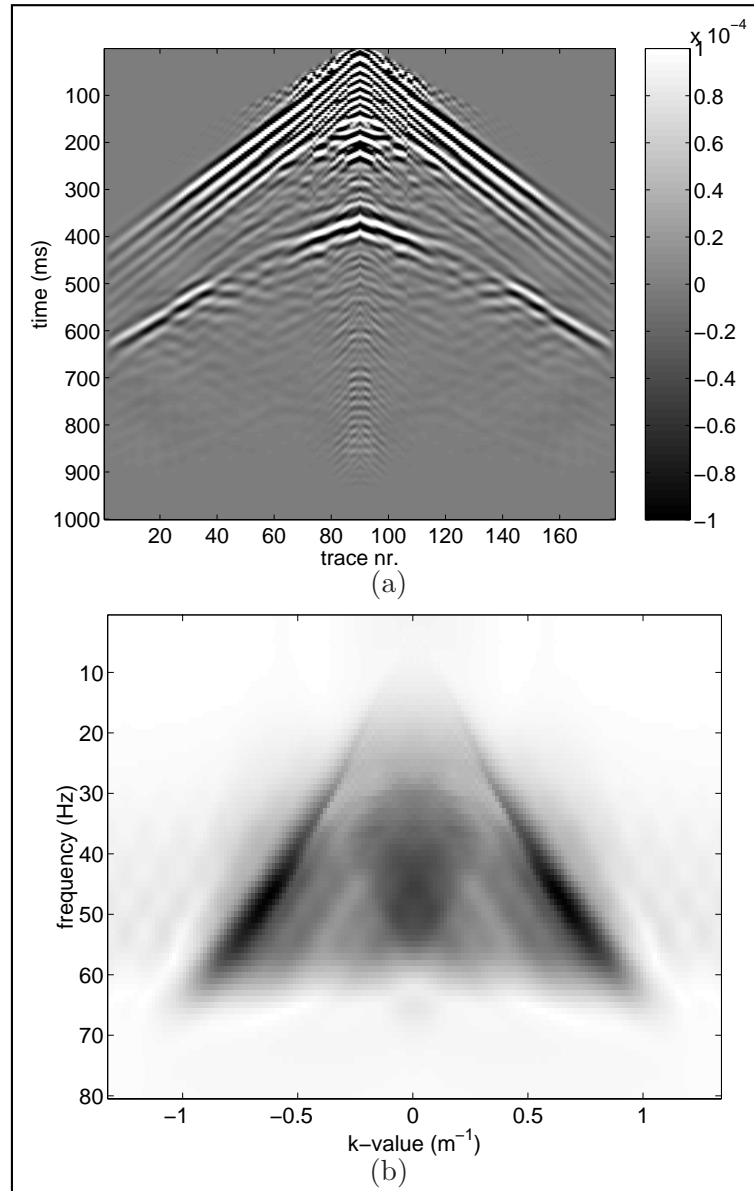


Figure C.10: (a) Data of the Sofia dataset, to be used for analysis with 1-D scheme, eq. (3.25), amplitudes are clipped to provide a better view, (b) (f, k) -spectrum of (a).

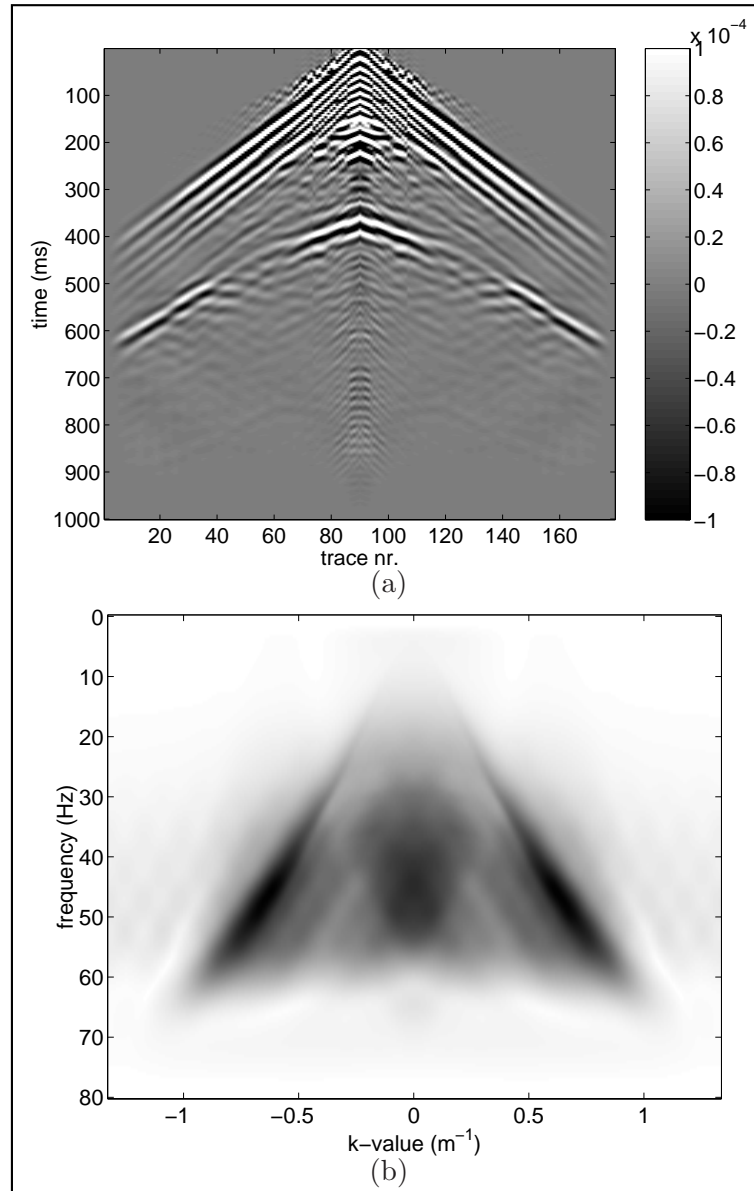


Figure C.11: (a) Result of removal procedure, eq. (3.25), where we used $\rho = 0 \text{ kg/m}^3$, (b) (f, k) -spectrum of (a).

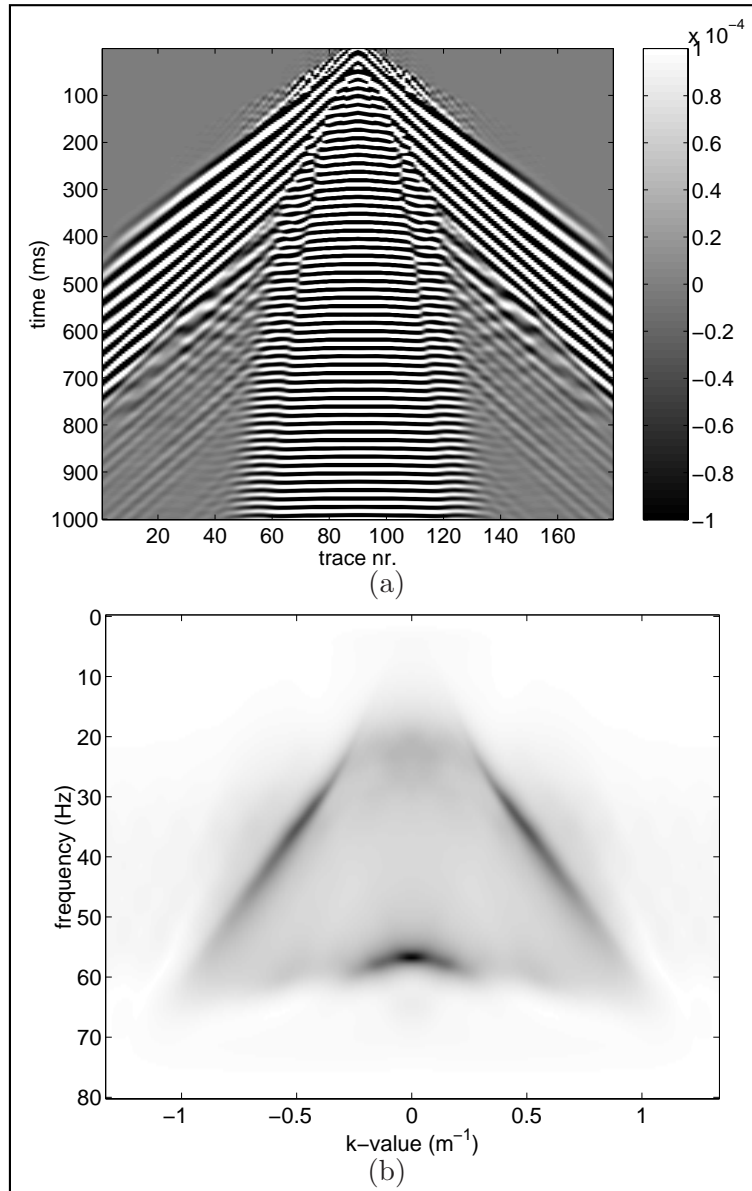


Figure C.12: (a) result of removal procedure, eq. (3.25), where we used $\rho = 3000 \text{ kg/m}^3$, (b) (f, k) -spectrum of (a).

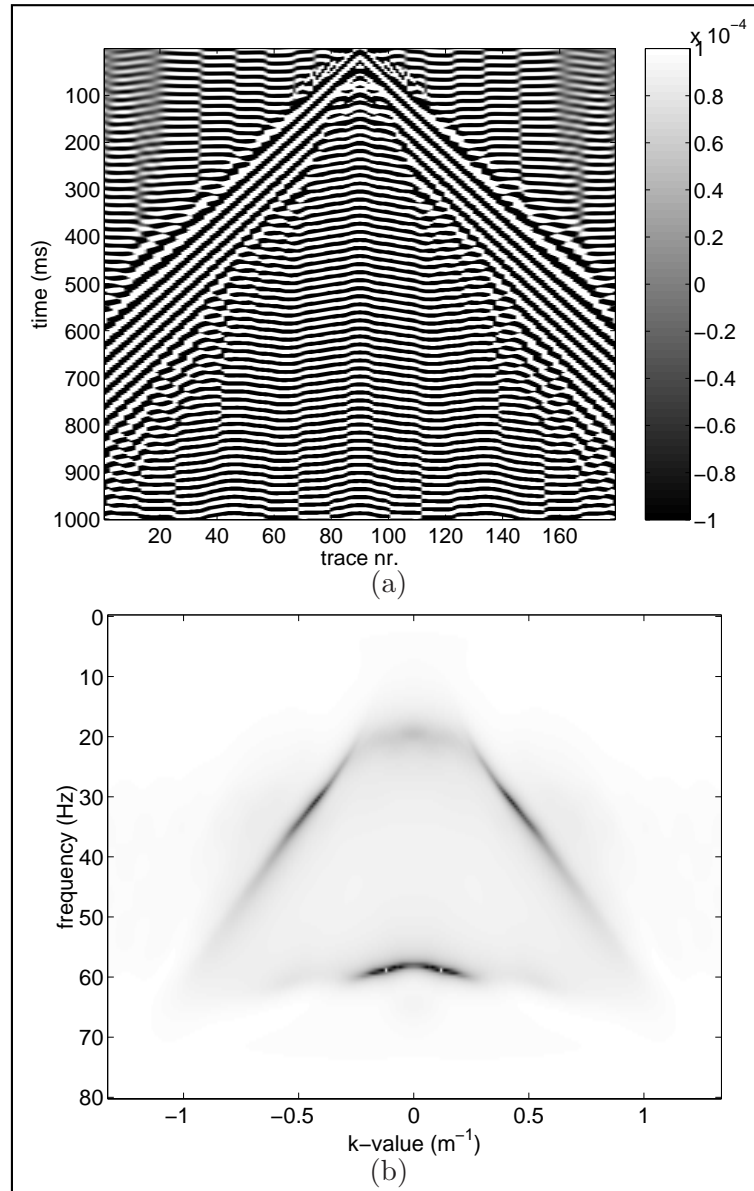


Figure C.13: (a) Result of removal procedure, eq. (3.25), where we used $\rho = 5000 \text{ kg/m}^3$, (b) (f, k) -spectrum of (a).

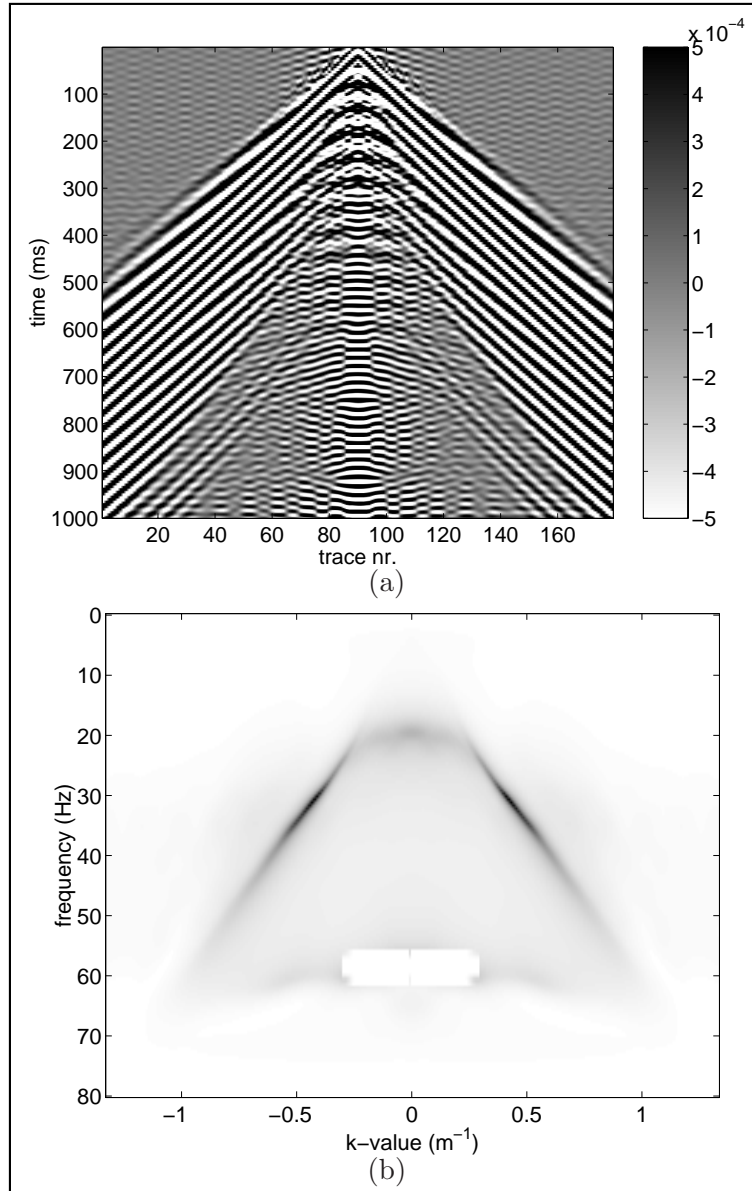


Figure C.14: (a) Result of removal procedure, eq. (3.25), where we used $\rho = 5000 \text{ kg/m}^3$, and where we removed an anomalous point near $k_x = 0$, (b) (f, k) -spectrum of (a).

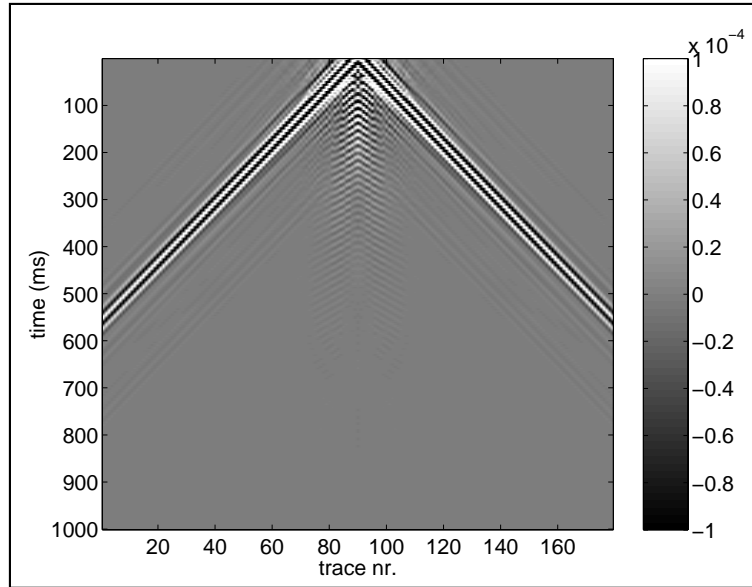


Figure C.15: Result of removal procedure, eq. (3.25), where we used $\rho = 50,000 \text{ kg/m}^3$

synthetic examples.

C.5 Conclusions and recommendations

The Love wave removal method did not provide satisfactory results on the Sofia field data. It seems that the assumptions we made in Section C.2 do not conform to the reality in that case. In Sections C.4.1 and C.4.2, we proved that at least two of these assumptions were correct. The remainder of this appendix discusses other assumptions, which we were not able to check, and gives some possible recommendations for improvement.

■ C.5.1 Concerning near-field and 3-D effects

In the course of this thesis, we assumed that SH-waves behaved “pseudo-acoustic”, which means that we assumed that only one wave type, the SH-waves, occur. And when we have a medium with line sources, then it does. However, in the case of point sources in an elastic medium, data are polluted

with near-field effects. These do not occur in acoustic media, or when the SH-waves are generated with line sources! See for example eq. (B.19) or de Hoop [1995], compared to eq. (B.10). Although eq. (B.19) is derived for media with line sources, the expression is the same for media with point sources, and therefore i and/or $j = 2$ can also be substituted in this equation. This means that even decoupled SH-waves have near-field wavefields, while for the application of the removal procedure on the Sofia dataset, we simply assumed that they were nonexistent. As we can see in Figure 5.4, the presence of this near-field wavefield can distort the wavelet of the dataset. For the Sofia dataset, this would mean that there are two wavelets in each shot: one wavelet where the wavefield is distorted by near-field effects, and the “correct” wavelet in the far field.

Although we did check if the method was sensitive to whether or not the data was generated with line sources or point sources (which it was not), we did not take the near-field effects into account there. To test whether or not near-field effects do have such a great effect on the Love wave removal method, we need a dataset modeled with full 3-D finite difference modeling. This is computationally very expensive, and therefore it has not been tested.

Perhaps, in the future, an amplitude pre-processing procedure as described by Wapenaar et al. [1992] should be performed prior to the application of the Love wave removal procedure. This would mean that the $v_{1,1}$ -component is needed in addition to the $v_{2,2}$ -component to construct a $v_{2,2}$ line-source response.

■ C.5.2 Concerning heterogeneities and anisotropy

In the theory, one of the main assumptions was that the top layer was homogeneous and isotropic. In Chapter 4, we stated that deviations in the mass density and velocity will not have a great influence on the performance of the removal method. However, Ghose [1995] shows that our assumption of isotropy may be presumptuous. According to this, it is the top layers of the medium that show the highest degree of anisotropy. Also, Ernst [1999] shows that the shallow subsurface is often heavily contaminated with small scale heterogeneities. Such small scale heterogeneities manifest themselves in the same manner as anisotropy. Anisotropy causes a wave traveling through the subsurface to change polarity. Therefore, when the wave reaches a receiver, even though it is still a decoupled SH-wave, it will have components both in the crossline (x_2) direction and in the inline (x_1) direction. The amount of change not only depends on the degree of anisotropy, but also on the dis-

tance the wave traveled through the subsurface. The change will have an effect on both the amplitude and phase of traces containing data from the x_2 -component.

Ghose and Osada [1993] propose a method to counter the effects of anisotropy by using both components of the particle velocity and counter-rotate the data in such a way, that the energy of one component reaches a minimum, while the other component reaches a maximum. Since we did not record the x_1 -component of the particle velocity, we cannot check if anisotropy is part of the problem. We can also not correct for it by using this method if it is.

This section, and the previous one, show that multi-component recordings, with regard to both the source and receiver directions, are in all probability a necessity for the successful application of the Love wave removal procedure.

An attempt at wavelet estimation based on energy minimization

In Chapter 4, it became clear that an accurate knowledge of the source wavelet was needed in order for the removal procedure to work. This source wavelet is usually unknown, and therefore, we need an estimation procedure.

Classical estimation procedures, such as developed by Weglein and Secrest [1990] (later perfected by Tan [1999]), do not work in our case, because they make use of specifics of marine seismics. More precise, these procedures require that sources and receivers are located below the water surface, whereas in our configuration, they are located *on* the surface.

Another approach, taken by van Borselen et al. [1994], is to base the wavelet estimation procedure on the concept of energy minimization. In Chapter 4, we have seen that a wrongly estimated wavelet only added noise to the data. Therefore, if we find a wavelet that manages to reduce the total energy in the data, then this is an indication that it leads to the right wavelet. However, Van Borselens method is tied to a Neumann expansion series. And as we showed in Chapter 3, on page 29, a Neumann series expansion is impossible in our case of Love wave removal. Ikelle et al. [1997] propose to do the same procedure, but with only taking the first order multiple. This could work for in our case, since although a Neumann series expansion is

impossible, we can always take only the first term. However, one condition for Ikelle's method to converge, is that removing the first order multiple reduces the energy in the data. This proved to be not the case for our situation of Love waves, which are, in one point of view, interfering multiples.

This appendix shows our attempt at developing a wavelet estimation procedure. It is also based on energy minimization. However, we take our full inversion equation as the basis. Unfortunately, our attempt was not very successful. The initial estimation of the wavelet proved to be very good, but further updates of this wavelet did not converge to the correct solution. We will discuss the reason for this at the end of this appendix.

D.1 Basis definitions

Since the theory in this appendix is designed for discrete data organized in matrices, it is convenient to define an inner product for these matrices:

$$\langle \mathbf{A}; \mathbf{B} \rangle = \sum_{\text{all } x^S} \sum_{\text{all } x^R} A(x^R, x^S) \cdot B^*(x^R, x^S), \quad (\text{D.1})$$

where the star (*) denotes a complex conjugation, and the matrices have the same properties as described in Section 3.5.

A matrix has a real norm, which is defined as:

$$\|\mathbf{A}\| = \sqrt{\langle \mathbf{A}; \mathbf{A} \rangle}, \quad (\text{D.2})$$

which is by definition greater than zero, or only zero when the matrix consists of zeros.

D.2 Problem statement

As the starting point, we take the matrix equation, eq. (3.27), and write it a bit different to show the wavelet dependence:

$$\hat{\mathbf{V}}_2^{\text{nosurf}} = \left[\frac{1}{\hat{f}_2(s)} \hat{\mathbf{K}} + \mathbf{I} \right]^{-1} \cdot \hat{\mathbf{V}}_2^{\text{surf}}, \quad (\text{D.3})$$

in which $\hat{\mathbf{K}}$ is defined, without wavelet this time, as:

$$\hat{\mathbf{K}} = \mu \Delta x_1 \mathcal{F}_S^{-1} \left\{ \mathcal{F}_S \left\{ \hat{\mathbf{V}}_2^{\text{surf}} \right\} \cdot \mathbf{\Gamma}_s \right\}. \quad (\text{D.4})$$

In numerical implementations, we always take the Laplace parameter as: $s = \varepsilon + j\omega$. This makes eq. (D.3) also an equation in the space-frequency domain (as opposed to the space-Laplace domain).

The problem consists of finding a source wavelet, which causes a minimum in the energy norm. This energy norm is defined as:

$$E = \sum_{\text{pos. } \omega} ||\hat{\mathbf{V}}_2^{\text{nosurf}}||^2. \quad (\text{D.5})$$

The only a priori information we have about the wavelet, is that it is causal and real valued in the time domain. The causality condition is enforced by the Hilbert transforms between the real part and the imaginary part of the wavelet (in the frequency domain). This means that the real part of the source wavelet is related to the “complete wavelet” ($\hat{r}_2(j\omega) = \text{Re}(\hat{f}_2(j\omega))$), through a linear operator (Fokkema and van den Berg [1993]):

$$\hat{f}_2(j\omega) = \mathcal{C}\{\hat{r}_2(j\omega)\} = 4\mathcal{F}_t \left\{ \chi(t) \text{Re} \left(\mathcal{F}_t^{-1} \{ \chi(\omega) \hat{r}_2(j\omega) \} \right) \right\}, \quad (\text{D.6})$$

where $\chi(a)$ is the characteristic function, which was already defined in eq. A.1. \mathcal{F}_t denotes a Fourier transform with respect to time.

D.3 Iterative solution

Suppose that at some point, we know an approximation of the source wavelet: $\hat{f}_2^{(n-1)}(j\omega)$. Then we try to improve that wavelet by updating it:

$$\hat{f}_2^{(n)}(j\omega) = \hat{f}_2^{(n-1)}(j\omega) + \alpha^{(n)} \hat{d}^{(n)}(j\omega). \quad (\text{D.7})$$

Because we are interested in the relative decrease in energy, we make the energy normalized to the original (surface data) energy:

$$\bar{E}^{(n)} = \frac{\sum_{\text{pos. } \omega} ||\hat{\mathbf{V}}_2^{\text{nosurf},(n)}||^2}{\sum_{\text{pos. } \omega} ||\hat{\mathbf{V}}_2^{\text{surf}}||^2}. \quad (\text{D.8})$$

Posed this way, the problem is divided into three different pieces: Finding a constant $\alpha^{(n)}$, in such a way that the energy is minimized, finding a suitable update direction $\hat{d}^{(n)}(j\omega)$ and finding the first approximation of the source wavelet $\hat{f}_2^{(0)}(j\omega)$.

■ D.3.1 Minimizing the energy

We try to find a minimum in the energy function, with respect to $\alpha^{(n)}$. However, the expression for $\hat{\mathbf{V}}_2^{\text{nosurf},(n)}$ is not linear in $\alpha^{(n)}$. If, however, we could approximate the expression in such a way that it is linear, then the energy function becomes a quadratic function, and it will have a unique minimum. To this end, we examine the matrix operator

$$\left[\frac{1}{\hat{f}_2^{(n)}(j\omega)} \hat{\mathbf{K}} + \mathbf{I} \right]^{-1} = \left[\frac{1}{\hat{f}_2^{(n-1)}(j\omega) + \alpha^{(n)} \hat{d}^{(n)}(j\omega)} \hat{\mathbf{K}} + \mathbf{I} \right]^{-1}. \quad (\text{D.9})$$

We extract $\hat{f}_2^{(n-1)}(j\omega)$ from this equation, and then make a Taylor expansion, where we only take the first two terms:

$$\begin{aligned} \left[\frac{1}{\hat{f}_2^{(n-1)}(j\omega) \left(1 + \frac{\alpha^{(n)} \hat{d}^{(n)}(j\omega)}{\hat{f}_2^{(n-1)}(j\omega)} \right)} \hat{\mathbf{K}} + \mathbf{I} \right]^{-1} &\approx \\ \left[\frac{1}{\hat{f}_2^{(n-1)}(j\omega)} \left(1 - \frac{\alpha^{(n)} \hat{d}^{(n)}(j\omega)}{\hat{f}_2^{(n-1)}(j\omega)} \right) \hat{\mathbf{K}} + \mathbf{I} \right]^{-1}. \end{aligned} \quad (\text{D.10})$$

Next, we extract the matrix $\left(\frac{1}{\hat{f}_2^{(n-1)}(j\omega)} \hat{\mathbf{K}} + \mathbf{I} \right)$, and again make Taylor expansion, with only two terms:

$$\begin{aligned} &\left[\left(\frac{1}{\hat{f}_2^{(n-1)}(j\omega)} \hat{\mathbf{K}} + \mathbf{I} \right) \cdot \left(\mathbf{I} - \left(\frac{1}{\hat{f}_2^{(n-1)}(j\omega)} \hat{\mathbf{K}} + \mathbf{I} \right)^{-1} \cdot \frac{\alpha^{(n)} \hat{d}^{(n)}(j\omega)}{(\hat{f}_2^{(n-1)}(j\omega))^2} \hat{\mathbf{K}} \right) \right]^{-1} \\ &\approx \left[\mathbf{I} + \left(\frac{1}{\hat{f}_2^{(n-1)}(j\omega)} \hat{\mathbf{K}} + \mathbf{I} \right)^{-1} \cdot \frac{\alpha^{(n)} \hat{d}^{(n)}(j\omega)}{(\hat{f}_2^{(n-1)}(j\omega))^2} \hat{\mathbf{K}} \right] \cdot \left[\frac{1}{\hat{f}_2^{(n-1)}(j\omega)} \hat{\mathbf{K}} + \mathbf{I} \right]^{-1}. \end{aligned} \quad (\text{D.11})$$

With this, we have shown that we can write eq. (D.3) as:

$$\begin{aligned} \hat{\mathbf{V}}_2^{\text{nosurf},(n)} \approx & \left[\mathbf{I} + \left(\frac{1}{\hat{f}_2^{(n-1)}(j\omega)} \hat{\mathbf{K}} + \mathbf{I} \right)^{-1} \cdot \frac{\alpha^{(n)} \hat{d}^{(n)}(j\omega)}{(\hat{f}_2^{(n-1)}(j\omega))^2} \hat{\mathbf{K}} \right] \cdot \\ & \left[\frac{1}{\hat{f}_2^{(n-1)}(j\omega)} \hat{\mathbf{K}} + \mathbf{I} \right]^{-1} \cdot \hat{\mathbf{V}}_2^{\text{surf}}. \end{aligned} \quad (\text{D.12})$$

This equation is a linear function of $\alpha^{(n)}$. Let's remind that we are looking for a minimum in the energy. Therefore we differentiate the energy function with respect to $\alpha^{(n)}$. Or, since it is a quadratic function, we can also differentiate with respect to its complex conjugate:

$$\frac{\partial E^{(n)}}{\partial \alpha^{(n)}} = \frac{\partial E^{(n)}}{\partial \alpha^{(n)*}} = \sum_{\text{pos. } \omega} \langle \hat{\mathbf{V}}_2^{\text{nosurf},(n)}, \frac{\partial}{\partial \alpha^{(n)}} \hat{\mathbf{V}}_2^{\text{nosurf},(n)} \rangle = 0. \quad (\text{D.13})$$

For the derivative within the inner product, we find:

$$\begin{aligned} \frac{\partial}{\partial \alpha^{(n)}} \hat{\mathbf{V}}_2^{\text{nosurf},(n)} = & \left(\frac{1}{\hat{f}_2^{(n-1)}(j\omega)} \hat{\mathbf{K}} + \mathbf{I} \right)^{-1} \cdot \frac{\hat{d}^{(n)}(j\omega)}{(\hat{f}_2^{(n-1)}(j\omega))^2} \cdot \hat{\mathbf{K}} \cdot \left(\frac{1}{\hat{f}_2^{(n-1)}(j\omega)} \hat{\mathbf{K}} + \mathbf{I} \right)^{-1} \cdot \hat{\mathbf{V}}_2^{\text{surf}}. \end{aligned} \quad (\text{D.14})$$

At this point, we would like to make some abbreviations:

$$\hat{\mathbf{H}}^{\text{inv}} = \left(\frac{1}{\hat{f}_2^{(n-1)}(j\omega)} \hat{\mathbf{K}} + \mathbf{I} \right)^{-1}, \quad (\text{D.15})$$

$$\hat{\mathbf{D}}^{\text{iff}} = \frac{1}{(\hat{f}_2^{(n-1)}(j\omega))^2} \hat{\mathbf{H}}^{\text{inv}} \cdot \hat{\mathbf{K}} \cdot \hat{\mathbf{H}}^{\text{inv}}. \quad (\text{D.16})$$

And with these definitions we find that:

$$\alpha^{(n)} = - \frac{\sum_{\text{pos. } \omega} \hat{d}^{(n)}(j\omega)^* \langle \hat{\mathbf{H}}^{\text{inv}} \cdot \hat{\mathbf{V}}_2^{\text{surf}}; \hat{\mathbf{D}}^{\text{iff}} \cdot \hat{\mathbf{V}}_2^{\text{surf}} \rangle}{\sum_{\text{pos. } \omega} |\hat{d}^{(n)}(j\omega)|^2 \cdot \|\hat{\mathbf{D}}^{\text{iff}} \cdot \hat{\mathbf{V}}_2^{\text{surf}}\|^2}, \quad (\text{D.17})$$

When we make the constraint that $\alpha^{(n)}$ has to be real, a similar expression can be derived. We only have to take the real part of eq. (D.17).

■ D.3.2 The (conjugate) gradient direction

The update direction $\hat{d}^{(n)}(j\omega)$ is chosen as the Polak-Ribière conjugate gradient direction (Brodley [1977]):

$$\hat{d}^{(n)}(s) = \begin{cases} \mathcal{C}\{\hat{g}^{(1)}(j\omega)\}, & n = 1, \\ \mathcal{C}\{\hat{g}^{(n)}(j\omega)\} + \gamma^{(n)}\hat{d}^{(n-1)}(j\omega), & n > 1, \end{cases} \quad (\text{D.18})$$

with

$$\gamma^{(n)} = \frac{\sum_{\text{pos. } \omega} [\hat{g}^{(n)}(j\omega) (\hat{g}^{(n)}(j\omega) - \hat{g}^{(n-1)}(j\omega))]}{\sum_{\text{pos. } \omega} [\hat{g}^{(n-1)}(j\omega)]^2}, \quad (\text{D.19})$$

where $\hat{g}^{(n)}(j\omega)$ is a real gradient direction, which we will determine now. For this, we look at eq. (D.17). The denominator is real, and always greater than zero. Therefore, for improvement ($\alpha^{(n)} \neq 0$), the real part of the numerator must not be zero. We substitute $\hat{d}^{(n)}(j\omega) = \mathcal{C}\{\hat{g}^{(n)}(j\omega)\}$ in this numerator, and with this, the improvement condition becomes:

$$\text{Re} \left(\sum_{\text{pos. } \omega} \mathcal{C} \left\{ \hat{g}^{(n)}(j\omega) \right\}^* \cdot \left\langle \hat{\mathbf{H}}^{\text{inv}} \cdot \hat{\mathbf{V}}_2^{\text{surf}}; \hat{\mathbf{D}}^{\text{iff}} \cdot \hat{\mathbf{V}}_2^{\text{surf}} \right\rangle \right) \neq 0. \quad (\text{D.20})$$

We can show that this equation equals to (van den Berg [1994]):

$$\sum_{\text{pos. } \omega} \hat{g}^{(n)}(j\omega) \cdot \text{Re} \left(\mathcal{C} \left\{ \left\langle \hat{\mathbf{H}}^{\text{inv}} \cdot \hat{\mathbf{V}}_2^{\text{surf}}; \hat{\mathbf{D}}^{\text{iff}} \cdot \hat{\mathbf{V}}_2^{\text{surf}} \right\rangle \right\} \right) \neq 0. \quad (\text{D.21})$$

This expression does not vanish, and thus the improvement condition is satisfied, when we take:

$$\hat{g}^{(n)}(j\omega) = \text{Re} \left(\mathcal{C} \left\{ \left\langle \hat{\mathbf{H}}^{\text{inv}} \cdot \hat{\mathbf{V}}_2^{\text{surf}}; \hat{\mathbf{D}}^{\text{iff}} \cdot \hat{\mathbf{V}}_2^{\text{surf}} \right\rangle \right\} \right). \quad (\text{D.22})$$

This gradient direction is used in eq. (D.18). It enforces the causality of the source wavelet.

■ D.3.3 Initial Guess

There are not many constraints on the initial guess of the source wavelet for the wavelet estimation scheme to converge. The only condition is that it must also be a causal and real-valued function in time. One approach is to start with a constant. Since we divide by the source function (see eq. (D.3)), we

cannot take this constant as zero. Therefore, we try to find a constant, which also causes a minimum in the energy. For this, we make a Taylor expansion of eq. (D.3), and take only the first two terms:

$$\hat{\mathbf{V}}_2^{\text{nosurf}} \approx [\mathbf{I} - a\hat{\mathbf{K}}] \cdot \hat{\mathbf{V}}_2^{\text{surf}}, \quad (\text{D.23})$$

where a is a complex constant. Finding a minimum in the energy with respect to a , we find:

$$a = \sum_{\text{pos. } \omega} \frac{\langle \hat{\mathbf{V}}_2^{\text{surf}}; \hat{\mathbf{K}} \cdot \hat{\mathbf{V}}_2^{\text{surf}} \rangle}{\|\hat{\mathbf{K}} \cdot \hat{\mathbf{V}}_2^{\text{surf}}\|^2}. \quad (\text{D.24})$$

This constant is made causal in time by applying the causality operator:

$$\hat{f}_2^{(0)}(j\omega) = \frac{1}{2}\mathcal{C} \left\{ \frac{1}{a} \right\}. \quad (\text{D.25})$$

With these definitions, the method is completely defined.

Alternatively, we can perform eq. (D.24) frequency by frequency (i.e. we do not sum over the frequencies). This way, we build an initial wavelet, frequency by frequency. This can already be a very good estimation of the real wavelet.

D.4 Results and discussion

We applied the method described above on the simple case of a horizontally layered medium. This configuration is described in Section 3.6.1. At first, it seemed that the method would give good results. The initial-guess wavelet (the one built frequency by frequency) decreased the (normalized) energy to 0.3518. Further updates of the wavelet kept decreasing the energy, and the method did not converge to a solution. We show this in Figure D.1. Bear in mind that the energy that remains after applying the removal method with the true wavelet on this data is 0.2733.

But why does the method not converge to the right solution? To answer this question, we look at the wavelet that the method estimates. This is shown in Figure D.2. The initial-guess wavelet is already a good approximation of the true wavelet. However, further updates make the wavelet smaller and smaller. To find the reason for this, we look at eq. (D.3), or to eq. (D.12). When, in these equations, the wavelet $\hat{f}_2(s)$ goes to zero, the result $\hat{\mathbf{V}}_2^{\text{nosurf}}$ also goes to zero. And a matrix full of zeros certainly has the lowest possible

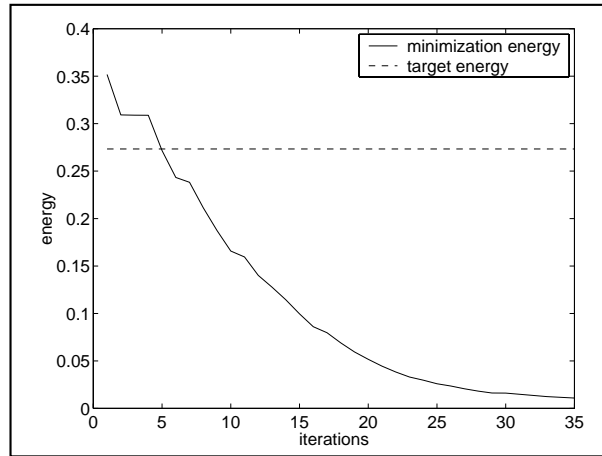


Figure D.1: Remaining energy in the shot record after wavelet estimation procedure. The dashed line is the energy that remains after applying the removal with the right wavelet.

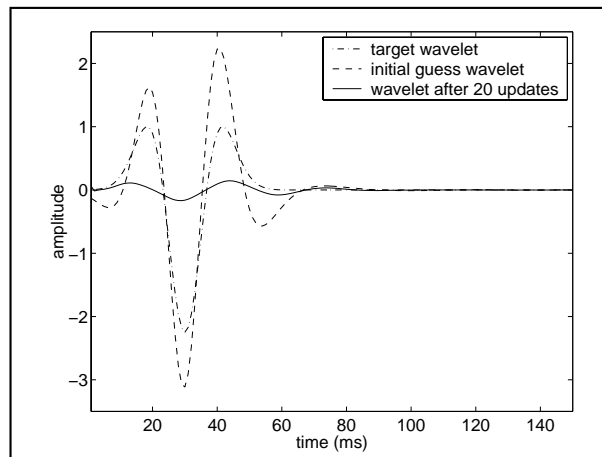


Figure D.2: Wavelets estimated by the energy minimization method. The dotted line is the true wavelet, used in forward modeling, the dashed line is the wavelet of the initial guess, and the solid line is the wavelet after 20 updates.

energy, but it is not the solution that we are looking for. We must conclude that the method described in this appendix does not work in its current form.

Maybe the method can be adjusted, for example by redesigning it to find the largest wavelet that causes a minimum in the energy. This problem is left open for examination as a possible future project.

Bibliography

- K. Aki and P.G. Richards. *Quantitative Seismology: Theory and Methods*. W.H. Freeman and Co., 1980. ISBN 0-7167-1058-7.
- G. Arfken. *Mathematical methods for physics*. Academic Press, 1985.
- A.J. Berkhout. *Seismic migration: Imaging of acoustic energy by wave field extrapolation. A. Theoretical aspects*. Elsevier, 1982.
- A.J. Berkhout. *Applied seismic wave theory*. Elsevier, 1987.
- B. Blonk. *Removal of scattered surface waves from seismic data*. PhD thesis, Delft, University of Technology, 1995.
- R.N. Bracewell. *The Fourier transform and its applications*. McGraw-Hill electrical and electronic engineering series. McGraw-Hill, New York, 1987.
- K.W. Brodley. *Unconstrained minimization, Chapter III*, in D.A.H. Jacobs, Ed., *The state of the art in numerical analysis*, pages 255–257. Academic Press, 1977.
- F.A. Dahlen and J. Tromp. *Theoretical global seismology*. Princeton university press, 1998.
- A.T. de Hoop. *Handbook of Radiation and Scattering of Waves*. Academic Press, 1995. ISBN 0-12-208655-4.

- A.T. de Hoop and H.J. Stam. Time-domain reciprocity theorems for elastodynamic wave fields in solids with relaxation and their application to inverse problems. *Wave Motion*, 10:479–489, 1988.
- G.P. Deidda and R. Balía. An ultrashallow SH-wave seismic reflection experiment on a subsurface ground model, in review. *Geophysics*, 66(04):1097–1104, 2001.
- F. Ernst. *Modeling, imaging and removal of guided waves*. PhD thesis, Delft, University of Technology, 1999.
- F. Ernst and G.C. Herman. Reduction of near-surface scattering effects in seismic data. *The Leading Edge*, 17(06):759–764, 1998.
- J. Falk. *Efficient seismic modeling of small-scale inhomogeneities by the finite-difference method*. PhD thesis, University of Hamburg, 1998.
- J.T. Fokkema and P.M. van den Berg. *Seismic Applications of Acoustic Reciprocity*. Elsevier, 1993. ISBN 0-444-89044-0.
- R. Ghose. Changes in shear-wave polarization with depth detected in Buckhorn oil field, Illinois. *Geotherm. Sci. & Techn.*, 5:79–89, 1995.
- R. Ghose, J. Brouwer, and V. Nijhof. A portable S-wave vibrator for high-resolution imaging of the shallow subsurface. In *58th. Annual Mtg., Eur. Ass. of Geosc. & Eng., proceedings*, page M037, 1996.
- R. Ghose and M. Osada. Anisotropy in near-surface formations and shear-wave birefringence - Its geotechnical implications: A VSP appraisal. *OYO Tech. Rep.*, ISSN 0912-6325:55–145, 1993.
- M. Holtzman. Chebyshev optimized geophone arrays. *Geophysics*, 28:145–155, 1963.
- L.T. Ikelle, G. Roberts, and A.B. Weglein. Source signature estimation based on the removal of first-order multiples. *Geophysics*, 62(6):1904–1920, 1997.
- H. Lamb. On the propagation of tremors over the surface of an elastic solid. *Philosophical Transactions of the Royal Society of London*, A 203:1–42, 1904.
- B. Lenders. The removal of surface-related wave phenomena in elastic media. Master’s thesis, Delft, University of Technology, 2002.

- A.E.H. Love. *A treatise on the mathematical theory of elasticity, fourth edition*. Dover Publications, 1926.
- R.D. Miller, J. Xia, and C.B. Park. Love waves: A menace to shallow shear wave reflection surveying. In *71st. Annual Mtg., Soc. Expl. Geoph., Expanded Abstracts*, pages 1377–1380, 2001.
- P.F. Morse and G.F. Hildebrandt. Ground roll suppression by the stackarray. *Geophysics*, 54(3):290–301, 1989.
- M.Q. Nguyen, F. Glangaud, and J.I. Mars. Mixed surface waves elimination. In *61th Annual Mtg., Eur. Ass. of Geosc. & Eng., in proceedings*, pages 6–21, 1999.
- R. Saatçılar and N. Canitez. The lattice filter in ground-roll suppression. *Geophysics*, 59(4):623–631, 1994.
- D.W. Steeples and R.D. Miller. Seismic reflection methods applied to engineering, environmental and groundwater problems. *Geotechnical and environmental geophysics*, 1:1–30, 1990.
- G. Swinnen, G.G. Drijkoningen, and D.J.M Ngan-Tillard. Tunnel boring machine of 2nd. heinenoord tunnel: source of seismic signals. In *4th. Annual Mtg., Envir. & Eng. Geophys. Soc. - Europ. Sec., proceedings*, 1998.
- T.H. Tan. Wavelet spectrum estimation. *Geophysics*, 64(6):1836–1846, 1999.
- R.G. van Borselen. *Removal of surface related multiples from marine seismic data*. PhD thesis, Delft, University of Technology, 1995.
- R.G. van Borselen, J.T. Fokkema, and P.M. van den Berg. Removal of surface-related wave phenomena - the marine case. *Geophysics*, 61(01):202–210, 1996.
- R.G. van Borselen, J.T. Fokkema, P.M. van den Berg, R.M. van der Weiden, and T.H. Tan. Fast energy minimization method for surface-related multiple removal. In *64th. Annual Mtg., Soc. Expl. Geoph., Expanded Abstracts*, pages 1485–1488, 1994.
- P.M. van den Berg. Minimization of the energy criterion: determination of the source wavelet in the multiple-elimination procedure. *Report nr. Et/EM 1994-04*, (Private communications), 1994.

- D.J. Verschuur. *Surface-related multiple elimination, an inversion approach*. PhD thesis, Delft, University of Technology, 1991.
- D.J. Verschuur, A.J. Berkhout, and C.P.A. Wapenaar. Adaptive surface-related multiple elimination. *Geophysics*, 57(9):1166–1177, 1992.
- C.P.A. Wapenaar, D.J. Verschuur, and P. Herrmann. Amplitude preprocessing of single and multicomponent seismic data. *Geophysics*, 57(9):1178–1188, 1992.
- A.B. Weglein and B.G. Secrest. Wavelet estimation for a multidimensional acoustic or elastic earth. *Geophysics*, 55(7):902–913, 1990.
- O. Yilmaz. *Seismic Data Processing*. Society of Exploration Geophysicists, Tulsa, 1987.

Abstract

Removing Love waves from shallow seismic SH-wave data

Geophysical exploration measurements are used to obtain an image of the geological structures of the subsurface, as detailed as possible. To this end, a wavefield is generated by a seismic source. This wavefield propagates through the subsurface, and will partly reflect on boundaries between layers with contrasting properties, and it will partly propagate further into the subsurface. De wavefields that have propagated back to the surface are measured with receivers. When this experiment is repeated several times on different locations, the measured data can be used to obtain the desired image.

There are two kinds of seismic waves that can propagate through the subsurface. The ones that are generally used are the pressure waves, or P-waves, where the movement of the particles is parallel to the propagation direction of the wave. The other ones are the shear waves, or S-waves, where the movement of the particles is perpendicular to the propagation direction of the wave. When the particle movement is horizontally polarized (perpendicular to the plane of propagation), this wave type is often decoupled, or in other words, it propagates independently of other wave types. These waves are also called SH-waves.

The surface of the Earth behaves as a perfect reflector for SH-waves. This means that all SH-waves that reach the surface will be completely reflected back into the subsurface. When the top layer of the subsurface is thin (smaller than the wavelength of the SH-wave), and when this top layer has a lower wave velocity than deeper layers, then the presence of the surface leads to

a kind of surface waves, which were first described by A.E.H. Love, and are therefore called *Love waves*. Love wave characteristics are: their group velocity is almost equal to the shear wave velocity; since they propagate solely along the surface, they attenuate slowly and are thus often stronger than reflected waves; and they are dispersive.

The presence of Love waves deteriorates the quality of the final picture (or seismogram), because they obscure the desired reflections. Existing techniques to remove Love waves from seismic data often perform insufficient, or require certain knowledge about the subsurface. This knowledge is generally not available. Therefore, the ideal method should be one where the measured data alone is sufficient to separate the Love waves from the desired reflection information.

The method we describe in this thesis uses the Betti-Rayleigh reciprocity theorem for elastic media. Reciprocity is a mathematical tool to relate two different states to each other. Here, one state is the actual situation, where the medium is bounded by a stress-free surface. The other state is an ideal situation, where there is no surface, and the top layer is extended to infinity. When there is no surface, there are also no surface waves.

By applying the reciprocity theorem, we derive an integral equation, from which the Love wave free wavefield can be solved as a function of the data that do contain these surface waves. Other input parameters are the (shear-) wave velocity and the mass density of the top layer, and the source wavelet. When the data are discrete, the integral equation becomes a matrix equation. This can be solved using conventional numerical methods, such as matrix inversion. When the medium is horizontally layered (a so called 1-D medium), the kernel of the matrix equation becomes diagonal in the wave-number domain. Then the matrix equation reduces to a scalar expression.

We tested the method on several synthetic datasets. In all cases, the Love waves were completely removed. Even other noise in the form of scattered Love waves was removed, in the cases where it was present. The method also had no problems when the input parameters were chosen wrongly. And when distortions were introduced into the data (distortions like random noise, or the effects of anelastic attenuation), the method still performed well.

To test the method on field data, we performed a seismic experiment on the site of the Sofia tunnel (before it was drilled) near Hendrik Ido Ambacht in the Netherlands. The dataset that was the result seemed all right at

first. Strong Love waves were indeed present in the data. However, we could not succeed in removing these Love waves with the method. Even worse, the method added noise to the data, to such an extent, that it completely obscured the original data. Although we searched extensively for possible reasons, we were not able to find the exact cause of the bad results.

In the final chapter, we made a start to remove the surface waves from coupled P- and SV-wave systems, using the same method as we did for SH-waves. Because P- and SV-waves are coupled, the resulting equations are also coupled. This means that we need all possible source and receiver combinations to remove the surface waves. But it appeared that the equations could be solved independently with regard to the source direction. We validated the theory with an example where we removed the Rayleigh wave from the response of a homogeneous half-space.

Samenvatting

Het verwijderen van Love golven uit ondiepe seismische SH-golf data

Geofysische exploratie-metingen zijn erop gericht om een zo gedetailleerd mogelijk beeld te krijgen van de geologische structuren in de ondergrond. Hiervoor wordt met behulp van een seismische bron een golfveld opgewekt. Dit golfveld propageert dan door de ondergrond, en zal op grensvlakken tussen contrasterende lagen gedeeltelijk worden teruggekaatst (gereflecteerd) en gedeeltelijk zal het verder door de ondergrond propageren. De golfvelden die vanuit de ondergrond weer terug naar het oppervlak komen, worden aldaar gemeten met ontvangers. Door dit experiment herhaaldelijk en op verschillende plaatsen te doen, kan de verkregen data gebruikt worden om het gewenste beeld te verkrijgen.

Nu zijn er twee soorten seismische golven die door de ondergrond kunnen propageren. De meest gebruikte is de longitudinale golf, ook wel P-golf genoemd, waarbij de bewegingsrichting van de deeltjes parallel is aan de voortplantingsrichting van de golf. De andere soort is de transversale golf, of de S-golf, waarbij de bewegingsrichting van de deeltjes loodrecht op de voortplantingsrichting van de golf staat. Wanneer de bewegingsrichting van de deeltjes ook nog eens horizontaal gepolariseerd is (loodrecht op het vlak van de propagatie-richting), is in veel gevallen deze golf ontkoppeld, oftewel hij propageert onafhankelijk. Deze golf wordt SH-golf genoemd.

Het oppervlak van de aarde gedraagt zich als een perfecte reflector voor SH-golven. Alle SH-golven die het oppervlak bereiken zullen dus volledig

gereflecteerd worden en weer terug de ondergrond in propageren. Wanneer nu de bovenste laag van de ondergrond dun is, dat wil zeggen kleiner dan de golflengte van de SH-golf, en als deze laag een lagere golfvoortplantingssnelheid heeft dan de diepere lagen, dan leidt de aanwezigheid van het oppervlak tot een type oppervlakte-golven, die het eerste beschreven zijn door A.E.H. Love, en die daarom Love golven worden genoemd. De kenmerken van Love golven zijn: hun voortplantingssnelheid is bijna gelijk aan die van SH-golven; doordat ze enkel langs het oppervlak propageren, doven ze langzaam uit, en zijn dus vaak sterker dan reflecties; en ze zijn dispersief.

De aanwezigheid van Love golven heeft een nadelige invloed op de kwaliteit van de uiteindelijke afbeelding (seismogram), doordat ze de gewenste reflecties van de diepere lagen overschaduwen. Bestaande technieken om Love golven uit seismische data te krijgen schieten vaak tekort, of veronderstellen een bepaalde kennis van de ondergrond. Deze kennis is over het algemeen niet aanwezig. Daarom zou een ideale methode er een zijn, waarbij de gemeten data alleen voldoende is om de Love golven te scheiden van de gewenste reflectie informatie.

De methode, die in dit proefschrift wordt beschreven, maakt gebruik van het reciprociteits-theorema voor elastische media van Betti en Rayleigh. Reciprociteit is een wiskundig concept waarmee twee verschillende toestanden aan elkaar gerelateerd kunnen worden. De ene toestand is de situatie zoals die in werkelijkheid is. Dat wil zeggen, met het reflecterende oppervlak. De andere toestand is een idealisering van de werkelijkheid. Hier is het oppervlak afwezig, en wordt de bovenste laag in feite tot in het oneindige voortgezet. En als er geen oppervlak is, dan zijn er ook geen oppervlakte-golven mogelijk.

Door gebruik te maken van het reciprociteits-theorema, wordt een integraal-vergelijking verkregen, waaruit het Love-golf-vrije golfveld kan worden opgelost, als functie van de data waar deze oppervlaktegolven nog wel in zitten. Andere invoer-parameters zijn de (schuif-) golfsnelheid en de massa-dichtheid van de bovenste laag, en het bron-signaal. In discrete vorm kan deze integraal-vergelijking geschreven worden als een matrix-vergelijking. Deze kan opgelost worden met standaard numerieke methodes, zoals matrix-inversie. Als de ondergrond horizontaal gelaagd is (een zogenaamd 1-D medium), wordt de matrix-operator diagonaal in het golf-getal domein. De matrix-vergelijking reduceert dan tot een scalaire uitdrukking.

De methode is getest op verschillende synthetische datasets. In alle

gevallen werden de Love golven er volledig uitgehaald. In de gevallen waar ze aanwezig waren, werden zelfs de verstrooide Love golven eruit gehaald. Ook wanneer de invoer-parameters verkeerd gekozen werden, kon de methode toch de Love golven verwijderen. Zelfs wanneer er verstoringen geïntroduceerd werden in de data, zoals bijvoorbeeld stochastische ruis of de effecten van anelastische demping, bleef de methode goed werken.

Om de methode uit te proberen op data uit het veld, is er een seismisch experiment uitgevoerd op de plaats van de toekomstige Sofia tunnel bij Hendrik Ido Ambacht. De dataset die hieruit volgde leek op het oog erg goed. Er waren sterke Love golven in aanwezig. Echter, het lukte de methode niet om ze te verwijderen. Sterker nog, er werd alleen maar ruis toegevoegd, en wel van een dusdanige sterkte, dat de originele data geheel overschaduwde werd. Alhoewel uitgebreid naar mogelijke redenen is gezocht, is de precieze oorzaak voor het slechte resultaat niet gevonden.

In het laatste hoofdstuk is een begin gemaakt om, met dezelfde methode als voor SH-golven, de oppervlakte-golven uit gekoppelde P- en SV-golf systemen te verwijderen. Doordat deze golven gekoppeld zijn (dat wil zeggen, ze propageren niet onafhankelijk van elkaar), vormen de uiteindelijke vergelijkingen ook een gekoppeld systeem. Alle mogelijke bron- en ontvanger-combinaties zijn dus nodig om de oppervlakte-golven te verwijderen. Echter, het blijkt dat de vergelijkingen onafhankelijk van de bron-richting opgelost kunnen worden. De geldigheid van de theorie wordt gevalideerd met een voorbeeld waarbij de zogenaamde Rayleigh-golf uit de respons van een homogene halfruimte wordt gehaald.

Curriculum Vitae

Lourens Frank van Zanen was born on January 27th., 1974, in Wormerveer (near Zaandam), the Netherlands. In 1992, he graduated from secondary school (Gymnasium) at the “Zaanlands Lyceum” in Zaandam. Later that year, he became a student at the Free University of Amsterdam, where he studied Physics. In August of the year 1997, he received his M.Sc. degree. His master’s thesis explored the possibilities of the development of a new control system for the Pelletron particle accelerator present at the university. He worked under the supervision of (the late) dr. H.J.W. Spoelder, section Computational Physics, and dr. R. Vis, section Nuclear Chemistry.

In the year 1998, he started his Ph.D. project in the Delft University of Technology, section of Applied Geophysics, under the supervision of Prof. dr. ir. J.T. Fokkema, Prof. dr. ir. C.P.A. Wapenaar and ir. G.G. Drijkoningen, Ph.D., all from this same section. The research was performed in the framework of the DIOC (Delft Interfaculty Research Centre) program “Observation of the Earth and Earth’s crust”. His work focused on the removal of Love waves from seismic SH-wave data. This research has led to the present Ph.D. thesis, and furthermore to a publication in a scientific journal, four presentations at international conferences and an M.Sc. thesis of a foreign student.

From October 2002 through March 2003, he performed a study of the possibilities of Amplitude Versus Offset (AVO-) analysis on seismic river data. This was done under supervision of Prof. dr. S.A.P.L. Cloetingh and ir. S. Tigrek of the Earth Sciences department of the Free University of Amsterdam, in the framework of the ISES research school. The results of this study were presented at the international ISES meeting in April 2003.

Acknowledgments

Of course, first of all, the author wishes to thank his promotor Prof. dr. ir. J.T. Fokkema. Thank you for introducing me into the world of geophysics, and making me enthusiastic about it.

Then a very warm thank you for my dear wife Carola, who stood by me all these years, and was even crazy enough to marry me during one of them.

They say that a fool can ask more questions than a thousand wise men can answer. For me, dr. ir. G.G. Drijkoningen and Prof. dr. ir. C.P.A. Wapenaar were always there to answer my questions, and I can only hope that I wasn't too big of a fool. However, you were certainly wise enough. Thank you for all your patience these years.

There is a long list of colleagues that I have had the pleasure of working with. I will try to address you all here. And if I do forget you, it is not because you were unimportant to me, but because I am incredibly clumsy when it comes to names. So here it goes: Thank you Michel, Rob, Jeroen, Menno, Gerdje, Jan, Jeroen, Jan-Willem, Kees, Rutger, Hedi, Antonio, Sevgi, Martijn, Nicoletta, Evert, Ranajit, Joachim, Jesper, Jan, Gerrit, Dennis, Deyan and Benedikt.

Of course I will not forget the people of the former OYO-department, especially dr. J. Brouwer. I don't think a fieldwork will ever be the same without you.

My friends, with whom I share a few of my vague hobbies: Thank you for not forgetting me and keeping me a sane person these years, Margot, Verik, Merik (Viking), Mariska, Blerik, Jasper, Roelof, Jacco, Monique, Christiaan, Ingrid, Michiel, Dorien, Daan, Vera, Shirin, Nazi and Amir.

Finally, I would like to thank my family; my grandparents, my parents and my brothers.